

May 2016

# Numerical Simulation of Slow Drying in Porous Media Using Pore Network Model

Zhenyu Xu

*University of Wisconsin-Milwaukee*

Follow this and additional works at: <https://dc.uwm.edu/etd>



Part of the [Engineering Commons](#)

---

## Recommended Citation

Xu, Zhenyu, "Numerical Simulation of Slow Drying in Porous Media Using Pore Network Model" (2016). *Theses and Dissertations*. 1229.

<https://dc.uwm.edu/etd/1229>

This Dissertation is brought to you for free and open access by UWM Digital Commons. It has been accepted for inclusion in Theses and Dissertations by an authorized administrator of UWM Digital Commons. For more information, please contact [open-access@uwm.edu](mailto:open-access@uwm.edu).

# **NUMERICAL SIMULATION OF SLOW DRYING IN POROUS MEDIA USING PORE NETWORK MODEL**

by

Zhenyu Xu

A Thesis Submitted in  
Partial Fulfillment of The  
Requirements for the Degree of

Doctor of Philosophy  
in Engineering

at

The University of Wisconsin-Milwaukee

May 2016

# ABSTRACT

## NUMERICAL SIMULATION OF SLOW DRYING IN POROUS MEDIA USING PORE NETWORK MODEL

by

Zhenyu Xu

The University of Wisconsin – Milwaukee, 2016  
Under the Supervision of Professor Krishna M Pillai

In our first model, an internal and external coupled solver is presented to simulate the slow drying of a porous medium placed adjacent to a laminar flow of air in a slit. The porous medium is represented by a  $20 \times 20$  pore-network model: the invasion-percolation algorithm is employed to simulate moisture redistribution; water-vapor migration in empty network is estimated using the purely diffusive approach. The external flow-field, unchanged during the drying simulation, is computed in the beginning using the Navier-Stokes equations. Subsequent water-vapor transport is modeled using a convection-diffusion type transport equation. A unique pore-to-cell meshing method and a novel unified (implicit) computational framework coupling the outer and the inner processes are proposed. Multi-scale problems in both space and time appear when solving the internal and external field simultaneously. To accurately simulate this kind of problem by aiming to minimize computation effort, the following aspects of the simulation are studied: space discretization schemes, numerical algorithms, mesh microstructure, and time-step refinement. The space discretization schemes tested in this paper include the Hybrid and the Hayase QUICK

schemes. The numerical algorithms tested to solve the drying process include the operator-splitting and a non-operator-splitting algorithm. Different mesh densities are tested along the directions parallel to and normal to the outer flow- porous-medium interface. Different time-steps are tested to find a suitable time-step for both the internal and the external computations. The external air velocity has some impact on the drying in the initial stages. Significantly, the microstructure of the pore-network is found to have a strong influence on drying.

In our second pore network model (which is based on our first model), the film effect is included and a novel logistic equation is used to relate the pore network variables with the external field variables. For migration of water vapors, the model accounts for both advective and diffusive transport in the external flow field while including diffusion in the dry part of the pore network.

By conducting a parametric study on the drying of a  $40 \times 40$  square network placed next to a slit flow, it is discovered that (a) higher hydraulic diameter of the throats leads to higher drying rates and longer constant drying-rate periods; (b) the drying time increases and the drying rate decreases as the throat cross section changes from a triangle to a square to a hexagon to a circle, which can be correlated to the weakening of the film effect; (c) increasing the external flow velocity (that leads to changing the Peclet number from 1 to 1000) has little effect on the drying rates and times; (d) increasing the external air humidity from 30% to 70 % leads to a large decrease in the drying rates and the consequent increase in the overall drying times.

The developed model is then used to simulate the drying of several thin porous media ( $40 \times$



40 ,  $80 \times 20$  , and  $160 \times 10$  ) with different aspect ratios placed either aligned-with or perpendicular-to a uniform 2-D flow. Plots of drying rates and drying times against the network saturation are studied. The presence of film during most of the drying period ensures that the surface pores are at saturated vapor pressure. As a result, the sharpest concentration gradients, which also control the drying rates, lie adjacent to the exposed surfaces. Consequently, the concentration gradients in the outer flow fields are very mild and play insignificant role in the drying of porous media. Hence, we reach a surprising conclusion—the orientation of thin porous media in the outer flow field is found to be irrelevant for drying. But expectedly, the higher exposed-area versus total volume ratio leads to faster drying. However, these conclusions should be examined further by future 3D simulations since a 2D simulation may underestimate the influence of external flow field on the drying of porous media.

Finally, the model is applied to the dual-porosity porous media. The drying simulation of a square-shaped and dual-porosity pore network is compared with a previously published experimental study. Two cases of small-pores side open and large-pore side open are considered. It is observed that though the simulation results of the  $12 \times 12$  network fail to match the experimental drying curves completely, important features of the drying process (such as complete emptying of large pores before the onset of drying in the small pore region of the large-pores side open case) are achieved. Next the drying of the same square-shaped, dual-porosity domain using a much refined  $100 \times 100$  network is carried out in a uniform air flow after keeping either the

large-pores or the small-pores side open. The former leads to faster drying and complete emptying of the large pores before the small pores. The latter witnesses the phenomenon of capillary pumping. Using the same refined network, the case of all side open is also studied. Changing the throat cross-section from circle to square leads to much faster drying. Introduction of microstructural irregularity in the network by randomly changing throat diameter and changing the coordination number of pores does not affect the drying rate and drying time significantly.

© Copyright by Zhenyu Xu, 2016  
All Rights Reserved

# TABLE OF CONTENTS

1	Introduction.....	1
1.1	Idealization of Pore Structures .....	2
1.2	General Description of the Drying Process of Pore Network .....	3
1.3	Definitions in Pore Network Model .....	7
1.4	Literature Review .....	8
1.5	Scope and Objective .....	12
1.6	Outline of the Thesis.....	14
2	Formulation I: P-N Model for Drying without the Film Effect .....	17
2.1	Modeling of the External Flow Field .....	17
2.2	Evaporation Modeling .....	19
2.3	Physics of Evaporation in the External Flow Field .....	19
2.3.1	Physics of Modeling Evaporation in Pore Network .....	20
2.4	Coupled Solution for Vapor Concentrations in the External Field and Pore-Network	
	22	
2.4.1	Operator-Splitting Algorithm .....	24
2.5	Non-Dimensionalization of Equations .....	25

2.6	Summary of Algorithm.....	26
3	Verification of Numerical Simulation.....	27
3.1	Slit Flow .....	29
3.2	Backward-Step Flow .....	30
3.3	Advection of a Gaussian Concentration Distribution.....	33
3.4	Verification of the I-P Algorithm Based Network Drying Module .....	35
4	Results from Formulation I and Discussions .....	37
4.1	Problem Description & Calculation Domain.....	37
4.2	Mesh Refinement Study .....	40
4.3	Time Step Selection.....	44
4.4	Influence of Schemes for Space Discretization.....	45
4.5	Operator-Splitting Method vs Non-Operator-Splitting Method.....	46
4.6	Influence of Peclet Number .....	47
4.7	Influence of Pore-Network Structure .....	50
4.8	Conclusions .....	51
5	Formulation II: P-N Model for Drying with Film Effect.....	53

5.1	Physics of Evaporation in Pore-Network .....	53
5.2	Dimensionless Analysis .....	58
5.3	Fully-Coupled Implicit Solution for Vapor Concentration in External Flow-Field and Pore Network .....	59
6	Examination of the Proposed Numerical Method.....	62
6.1	Testing the Approximation for the Relationship between Concentration, C, and $\phi$ .	62
6.2	Modified Drying Algorithms .....	64
6.3	Time Step Selection .....	66
6.4	Comparisons between Spatial Discretization Schemes .....	67
7	Identifying Factors Influencing the Film Effect .....	70
7.1	Influence of Throat (Hydraulic) Diameter.....	70
7.2	Influence of Throat Cross Section Shape .....	72
7.3	Influence of External Conditions.....	73
7.4	Summary & Conclusions.....	76
8	Studies in Drying of Thin Porous Media .....	77
8.1	Square Pore Network Drying in a Flow Field .....	77
8.1.1	Group 1 Simulations: One Side Open .....	78

8.1.2	Group 2 Simulations: Multiple Sides Open.....	79
8.2	Drying of Thin Porous Media.....	84
8.2.1	Group 3 Simulations: Aspect Ratio=4:1 .....	85
8.2.2	Group 4 Simulations: Aspect Ratio=16:1 .....	90
8.3	Comparison Between Different Aspect Ratios .....	94
8.4	Summary & Conclusions.....	95
9	Drying of Dual-Porosity Pore Network .....	97
9.1	A Comparison with Experiment .....	97
9.2	Square Pore Network in the Center .....	102
9.2.1	Group 1 Simulations: One Side Open .....	103
9.2.2	Group 2 Simulations: Influence of Irregularity in Pore Geometry.....	108
9.3	Summary & Conclusions.....	111
10	Summary and Concerns .....	113
	Appendix: Mathematical Models.....	114
	References.....	116
	CURRICULUM VITAE .....	121

# LIST OF FIGURES

Figure 1. Pore network model.....	3
Figure 2. General description - drying of porous media.....	4
Figure 3. Pore network definitions.....	7
Figure 4. Schematic of Beyhaghi’s method.....	12
Figure 5. Schematic grid layout for the coupled solution for vapor concentrations in the external flow-field and pore network – without film effect.....	23
Figure 6. Schematic of drying algorithm presented in this work.....	27
Figure 7. A schematic describing the geometry and boundary conditions of the considered 2-D slit flow .....	29
Figure 8. Velocity profile comparison between theoretical and numerical results.....	30
Figure 9. A schematic of the backward-step flow geometry.....	31
Figure 10. Velocity contour for the backward-step flow .....	32
Figure 11. Numerically obtained backward-step flow velocity profiles at different cross-sections .....	32
Figure 12. Schematic description of the code verification carried out by using the advection of Gaussian concentration distribution.....	33



Figure 13. Advection of Gaussian concentration distribution (Left $Pe = 1$ , right $Pe = 100$ ): a comparison of the numerical solution with the analytical solution .....	34
Figure 14. Verification of drying physics implementation (left: calculation domain; right: drying time-vs-network saturation plot).....	35
Figure 15. Simulation domain and problem description.....	38
Figure 16. Results of mesh refinement in the $Y$ direction, $Pe = 1000$ (Note: X04Y40 means use parameter 04 for $X$ direction meshing, and use 40 for $Y$ direction meshing. Higher number implies denser mesh).....	41
Figure 17. Results of mesh refinement in the $X$ direction, $Pe = 1000$ .....	42
Figure 18. Results of Mesh Refinement in $Y$ direction, $Pe = 1$ .....	42
Figure 19. Results of Mesh Refinement in $X$ direction, $Pe = 1$ .....	43
Figure 20. The final chosen mesh for the coupled inner-outer flow drying simulation .....	44
Figure 21. Time step selection .....	45
Figure 22. Comparison between the hybrid and QUICK schemes, $Pe = 1000$ .....	46
Figure 23. Effect of using the operator-splitting scheme for $Pe=1000$ .....	47
Figure 24. Influence of Peclet number on the drying kinetics.....	48
Figure 25. Phase distribution of different time step (Notes: 1: top row: $Pe = 1$ ; bottom row: $Pe =$	

<b>1000</b> ; 2: from left to right, time step 100, 300, 500, 700, 820; 3: the white line in the outside flow field shows the position of the concentration boundary layer (CBL).....	49
Figure 26. Influence of pore-network structure on drying kinetics .....	51
Figure 27. A typical set of “fingers” created by the liquid film climbing at the corners of a square cross-section throat .....	54
Figure 28. Cross section of various throats showing thin films existing between the thicker films attached to the corners .....	55
Figure 29. Geometrical details of a typical corner film .....	56
Figure 30. Relationship between dimensionless $\phi$ and $C$ : the real relationship, and the 3 approximated relationship by setting different coefficient $c = 2, 3, 4$ in Eq. (26) .....	60
Figure 31. Coupling of the outside-flow node cells and the P-N pores – with film effect.....	61
Figure 32. A $40 \times 40$ pore network put by side of, and open to, a slit flow during drying.....	62
Figure 33. A comparison of the evolution of drying rate and drying time for different approximations for the parameter C .....	63
Figure 34. Modified drying algorithm .....	64
Figure 35. A comparison of the predicted drying rates obtained using the original drying algorithm and the modified algorithm.....	65

Figure 36. Effect of different sub time-steps on the drying characteristics of pore network (For example, “SubStep=5” means that the drying time step is divided into 5 sub steps).....	67
Figure 37. Velocity field comparison (left: hybrid scheme; right: QUICK scheme).....	68
Figure 38. A comparison of the drying characteristics as predicted by three different spatial discretization schemes .....	68
Figure 39. Influence of throat diameter on film effect.....	71
Figure 40. Phase distribution and film radius distribution of case $D = 5\mu m$ (upper row: the phase distribution and outside concentration; lower row: the corresponding film radius).....	72
Figure 41. Influence of throat cross section shape.....	73
Figure 42. Influence of external conditions on the film effect for pore diameter = $5\mu m \pm 5\%$ . 74	
Figure 43. Influence of external conditions on the film effect for pore diameter = $10\mu m \pm 5\%$ .....	75
Figure 44. Velocity field around a square-shaped pore network at $Pe = 10$ (left: velocity contour; right: velocity contour and stream lines) .....	78
Figure 45. Study of drying of the square-shaped pore network when its one side is kept open, $Pe = 10, air\ humidity = 50\%$ .....	79
Figure 46. Changes in the liquid phase distribution (within the network) and CBL with time: open N+S sides (the outermost of the iso-concentration lines, the white lines, marks the location of the	

CBL boundaries).....	80
Figure 47. Changes in the liquid distribution (within the network) and CBL with time: open E+W sides (the outermost of the iso-concentration lines, the white lines, marks the location of the CBL boundaries).....	82
Figure 48. Changes in the liquid distribution (within the network) and CBL with time: open all sides (the outermost of the iso-concentration lines, the white lines, marks the location of the CBL boundaries).....	83
Figure 49. Drying characteristics of the square pore network when the multiple sides are opened together.....	84
Figure 50. Flow around a thin porous medium – horizontal, 4:1 (left: velocity distribution; right: streamline plot).....	85
Figure 51. Changes in the liquid phase distribution (within the network) and CBL with time– horizontal, 4:1.....	86
Figure 52. Flow around a thin porous medium – vertical, 4:1 (left: velocity distribution; right: streamline plot).....	87
Figure 53. Changes in the liquid phase distribution (within the network) and CBL with time– vertical, 4:1.....	88
Figure 54. Drying characteristics of the thin pore network with 4:1 aspect ratio when the multiple	

sides are opened .....	89
Figure 55. Flow around a thin porous medium – horizontal, 16:1 (left: velocity distribution; right: streamline plot) .....	90
Figure 56. Changes in the liquid phase distribution (within the network) and CBL with time– horizontal, 16:1 .....	91
Figure 57. Flow around a thin porous medium – Vertical, 16:1 (Left: velocity distribution, Right: streamline plot) .....	92
Figure 58. Changes in the liquid phase distribution (within the network) and CBL with time– vertical, 16:1 .....	93
Figure 59. Drying characteristics of the thin pore network with 16:1 aspect ratio when multiple sides are opened .....	94
Figure 60. A Comparison of drying characteristics of pore networks with different aspect ratios (W and H represent the P-N width and height, respectively) .....	95
Figure 61. Dual-porosity experiment setup (A: picture; B: a schematic describing elements of the setup; picture comes from (Pillai, et al., 2009) ).....	98
Figure 62. Prediction of drying rate and drying time as a function of network saturation for the <b>12 × 12</b> dual-porosity pore network .....	99
Figure 63. Phase distribution of simulations - <b>12 × 12</b> dual porosity pore network (A1:	

simulation results when the large-pores side is open with  $Pe = 400$ ; A2: experimental results when the large-pores side is open; B1: simulation results when the small-pores side is open with  $Pe = 100$ ; B2: experimental results when small side open; A2 and B2 are coming from (Pillai, et al., 2009) )..... 100

Figure 64. Dimensionless drying mass vs drying time – comparing with the experiment..... 101

Figure 65. Velocity field around square pore-network,  $Pe = 10$  (left side: velocity contour; right side: stream lines) ..... 103

Figure 66. Drying of dual porosity networks with one side open..... 104

Figure 67. Studying the drying characteristics of a dual-porosity network – with/without film effect ..... 104

Figure 68. Evolution of liquid-phase distribution and CBL with time in the dual-porosity network using square throats with film effect—the large-pores side is open (The outermost constant concentration curve is the CBL.) ..... 106

Figure 69. Evolution of liquid-phase distribution and CBL with time in the dual-porosity network using square throats with film effect—the small-pores side open (The outermost constant concentration curve is the CBL.) ..... 107

Figure 70. Dual-porosity pore network (left: regular; right: irregular)..... 108

Figure 71. Distributions of liquid-phase clusters and concentration contours – regular network,

random throat diameters ..... 109

Figure 72. Distributions of liquid-phase clusters and concentration contours – irregular network,  
random throat diameters .....110

Figure 73. Study of changes in drying rate and drying time of a dual-porosity network due to the  
introduction of geometrical irregularity.....111

# LIST OF TABLES

Table 1. Summary of verification cases .....	28
Table 2. Material properties and parameter values used in the present work .....	39
Table 3. Influence of random-number-generator parameters on the pore-network structure (Nomenclature: the case P1DR5 implies RSN=1 and MVP=5) .....	50



# LIST OF NOMENCLATURE

Note:

1. Symbols with bar on top are in their non-dimensionalized form
2. Symbols with \* as the superscript represent their reference value

$A, A_{i,j}, A_{avg}, A_F$  Area of throat cross-section or cell faces/Average Area/Film Area

CBL Concentration Boundary Layer

$c$  Coefficient

$C$  Liquid vapor concentration

$D$  Liquid mass diffusivity

I-P Invasion-Percolation

$l$  Throat length

$\dot{m}_{i,j}, \dot{m}_F, \dot{m}_G$  Mass flux between two pores/Mass flux through film/Mass Flux through gas

$M, M_d, M_v$  Molar Mass/Molar Mass of Dry Air/Molar Mass of Vapor

$N$  Number of film fingers

$p, p_a, p_v, p_l$  Pressure/Atmosphere Pressure/Vapor Pressure/Liquid Pressure

$Pe$  Peclet number

P-N Pore-Network

$Q_F$  Volume flux through film

$r$  Radius of curvature

$R, R_0, R_C, R_M$	Radius of throat/Radius of largest inscribed sphere/Radius of round corner/Radius of largest film curvature
$Re$	Reynolds number
$t$	time
$\mathbf{u}, U$	velocity
$x, y, X, Y$	coordinate

Greek Symbols:

$\alpha$	Half of the corner angle
$\beta$	Geometry factor of film effect
$\gamma$	Surface tension
$\delta_{i,j}$	Distance between two cells or pores
$\theta, \theta_C$	Contact angle/Critical contact angle
$\kappa$	Geometry factor of film effect
$\mu_g, \mu_l$	Air viscosity/Liquid viscosity
$\rho_g, \rho_l$	Air density/Liquid density
$\varphi_1, \varphi_2$	Constant related with film effect
$\phi_i, \phi_j$	Variable to calculate when film effect is considered
$\chi$	Ratio of film effect
$\psi_1, \psi_2, \psi_3, \psi_4, \psi_5$	Geometry factor of throat cross section

Subscript:

$i, j$  Index number of a cell/pore/throat

***Superscript:***

$n$  Time step

# ACKNOWLEDGMENTS

I would like to express my sincere gratitude to my adviser, Prof. Pillai, who provided me with relentless support, helpful guidance and suggestions, and endless patience, without which the completion of this dissertation would not have been possible.

I would like to thank Dr. Marc Prat of I.M.F.T., Toulouse, France, for providing some insightful guidance during the implementation of our simulation, and for providing the published experimental data.

I want to give my appreciation to all my dissertation committee members for their time and support.

Finally, I want to acknowledge to my master degree advisor, Prof. Chun-hian Lee, my family and my lovely girlfriend Ying Li.

# 1 INTRODUCTION

A porous medium is either a material containing pores or a collection of particles/fibers which when put together have pores between them. The skeletal, solid portion of such media is called the “matrix” or “frame”. The tiny voids, created between particles/fibers or carved out in the frame, are called pores, which are typically filled with gas or liquid (Dullien, 1991). Very often, the fluid transport is of interest in most applications, hence we are interested only in those porous media that have interconnected pores. Many materials fall in the category of porous media, for example, sponge, soil, sand, rock, cement, bone, wood, fabric, paper, food and ceramics. Research in porous media is of significant scientific and commercial interest in a number of industrial applications including composites processing, coating, food processing, production of building materials, pulp and paper industry, and pharmaceuticals. Drying of porous media is one such research topic.

The simulation methods for porous media problems can be classified into two major categories: the continuum methods, and the discrete methods. The continuum methods (or models) treat the porous media as a continuous material with volume-averaged macroscopic properties (Bear, 1988), while ignore the porous media’s pore-scale structure and attributes. This method is useful in large space-scale problems but its accuracy heavily depends on the selection of macroscopic properties, which must come from experiments or pore-level simulations. The

volume averaging continuum method is one of the proven and effective techniques for predicting such flow and transport coefficients using the closure formulation to upscale from the pore scale to the macro scale (Quintard & Whitaker, 1993).

On the other hand, the discrete method ‘goes into’ the porous media such that the pore-scale structures and processes inside the porous media are taken into account. The discrete method is usually employed to simulate small space-scale problems or to determine the macroscopic properties for the continuum models.

There are two major problems while modeling with the discrete methods: firstly, the representation of the geometry of a porous medium, and secondly, the modeling of transportation physics inside them.

## **1.1 Idealization of Pore Structures**

There are several idealized models of pore structures, which can be broadly categorized into three categories: pore network, array of solid particles, and hierarchical pore structure (Wikipedia, 2016).

Pore network model, as its name implied, is a network of pores interconnected by capillary throats. Array of solid particles model, literally, is a pack of particles close to each other. In hierarchical pore structure (Suzuki, et al., 2003), for example, the porous media is firstly idealized as a pack of larger-level particles, and each particle is further modeled as a pack of

smaller-level particles, etc. (Mao, et al., 2008).

Each of these three categories has its unique characteristics and has advantages over the others when modeling certain types of porous media. For example, array of solid particles is naturally suitable for modeling sand. Choosing the right idealization models is the first step towards an accurate simulation.

Pore-network (*P-N*) model, as shown in Figure 1, is created after extracting the skeleton of pore space from the porous media. The pore space forms a network-shaped structure, composed of joints and capillaries. The joints are called pores, and capillaries are called throats.

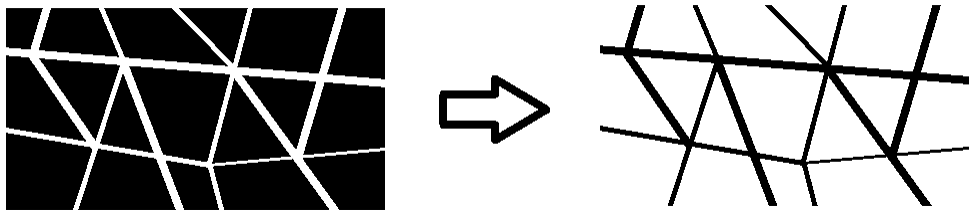


*Figure 1. Pore network model*

By changing the shape and size of the pores and throats, pore-network model can be used to model a broad range of porous media, such as fabrics, soil, open-cell ceramics, etc. This thesis focuses on studies involving pore-network models. Hence, all the following mathematical or physical descriptions are based on the pore-network model.

## **1.2 General Description of the Drying Process of Pore Network**

If a pore network filled with liquid has some openings to the surroundings, the liquid inside

will usually start drying up, and gradually all of the pores space will be occupied by the invading gas. The drying process and the involved physical phenomena are described in general terms as below (Yiotis & Boudouvis, 2003). *(Because the liquid we talked about is usually water, and the invading gas is usually air, so the terms liquid and water, gas and air will be used interchangeably in this thesis.)*

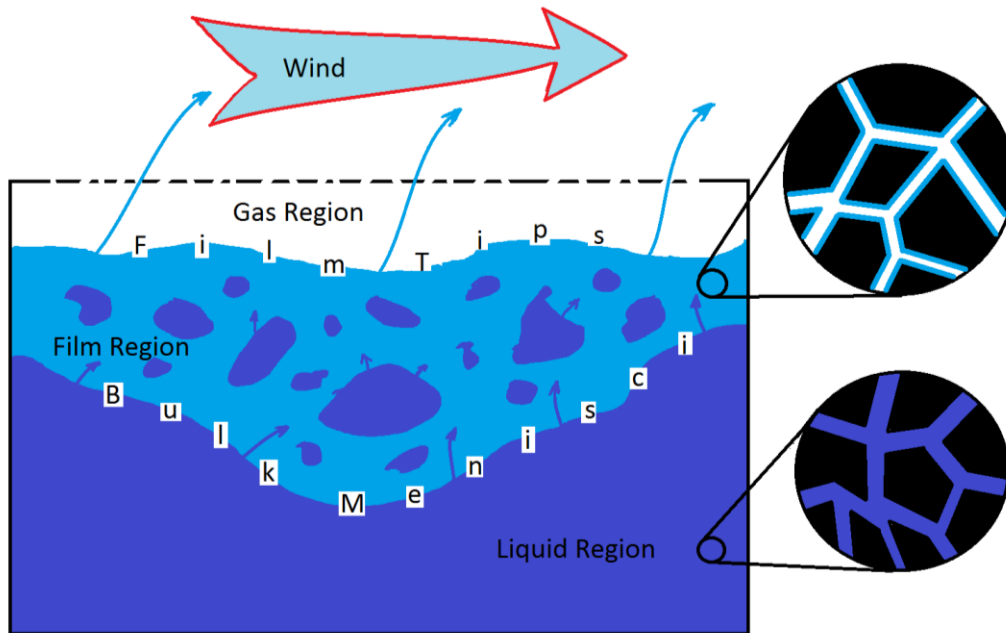


**Figure 2. General description - drying of porous media**

As we all known, the water-air interface is a boundary in dynamic equilibrium, where the number of water vapor molecules leaving the liquid phase equals the number of returning molecules. At this interface, the water vapor concentration (equal to the saturated vapor concentration, which is a function of temperature) reaches its peak value. If the surrounding concentration is lower than the saturated concentration, the vapor molecules on the interface will



diffuse into the environment. Because the vapor molecules diffuse into the far space, more vapor molecules have to come from the liquid phase to keep the interface concentration saturated. As more and more water molecules cross the interface and go into vapor phase, the water will start drying up.

It is the same scenario for porous media (Figure 5) during the drying process. Imagine a pore network initially filled with liquid. At the openings of the network, which is also the initial water-air (or drying) front. The water molecules escape from the liquid phase into the air phase, and then diffuse into the farther surroundings. As this process continues, the water-air drying front starts to recede deep into the porous medium, but diffusion of water vapor away from the front does not stop even in the tiny pore spaces. The water contained in pores of the porous medium keeps diminishing until it finally dries up. If a wind is blowing over the pore openings into the ambient, the bulk movement of the air will speed up the carrying-away of water vapor to the farther spaces through advection and accelerate the drying process.

During the drying process inside a porous medium, the liquid phase is also flowing and redistributing itself. Liquid pressure difference in different throats will drive the liquid phase from larger throats to smaller throats, such that the drying front inside a porous medium rarely recedes uniformly. The fronts at larger throats are usually observed to be receding quickly, while the fronts at smaller throats keep relatively stationary. This is because the capillary pressure behind a liquid-gas interface scales as  $\gamma/r$  where  $\gamma$  is the surface tension while  $r$  is the throat

radius, because of which the narrower throats have larger capillary pressures compared to the larger throats. This difference in the suction pressures leads to redistribution of the liquid phase from the larger throats to smaller ones during drying. Hence, liquid columns in smaller throats are kept stationary by the higher capillary pressures, while the columns in larger throats decrease. In fact, this is the basis behind the invasion-percolation (I-P) algorithm used for modeling the motion and breakup of drying front inside a porous medium during drying (Prat, 1993).

Besides the throat sizes, the hydrophobicity of the network material, and the cross-section shape of the throats also have influence on liquid redistribution during drying. In addition, the gravity and liquid viscosity also play important roles in the liquid flow.

Furthermore, the recession pattern of the water-air drying interface inside the throats is usually not like that of a flat area perpendicular to the throat axis. Instead, the liquid in the middle area of the throat recedes easily, while the liquid along the lateral corners of the throat tends to remain sticking longer. These liquid wedges along the throat corners are called *liquid films* or *film fingers*. During the drying process, the bulk liquid recedes first, leaving the film fingers to thin out slowly. In fact, the film fingers are often channels for the liquid to travel from the drying front into the dried up portions of the network and aid in the passage of water vapors into the outside air. As shown in Figure 2, the liquid flows from the bulk liquid region behind the drying front into the film region, and from the tips of the films, the liquid evaporate into the gas phase. Then the vapor is transported away from the porous media by advection and diffusion into

the surrounding airflow.

### 1.3 Definitions in Pore Network Model

From being wet to dry, the pores and throats of the pore-network experience a series of changes in their status. Initially they are filled with the liquid; and then bulk liquid retreats, and they are occupied by the films; after the films thin out, they are fully occupied by air. At each stage, different fluids and transportation mechanisms apply. For this reason, we differentiate the pores and throats at different stages by defining them as follows (Figure 3).

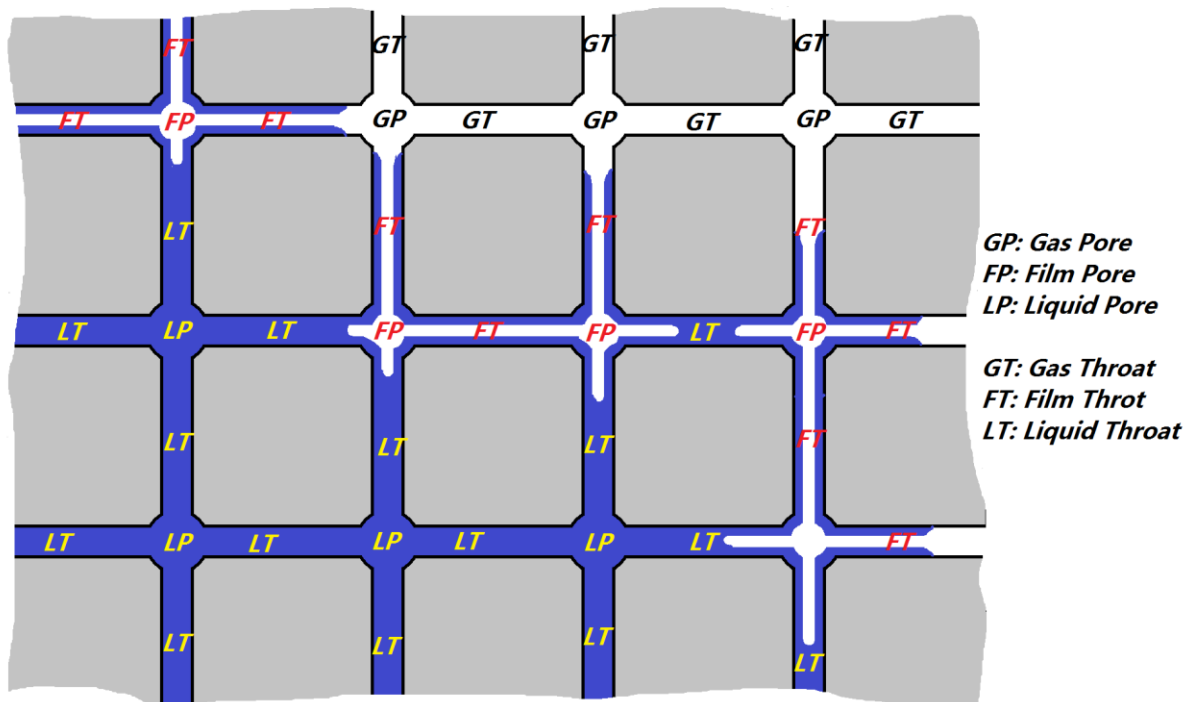


Figure 3. Pore network definitions

The definitions related to the pore network model:

- **Liquid Throat (LT):** the throat having the bulk liquid.
- **Film Throat (FT):** the throat with no bulk liquid, but having the film liquid.
- **Gas Throat (GT):** the throat that is completely dry and taken over by the gas.
- **Liquid Pore (LP):** the pore is filled with the liquid (usually, all the throats connected to such pores are LTs or Liquid Throats.)
- **Film Pore (FP):** the pores have no bulk liquid but the liquid inside the film; usually, among all its connected throats, there is at least one throat which is a film throat, and there are no gas throats.
- **Gas Pore (GP):** the pores fully taken by the gas; usually, there is at least one gas throat connecting with a gas pore.
- **Cluster:** a group of pores and throats, which share the same ‘Liquid’ status and are thus filled with the liquid, and are geometrically connected to each other.
- **Cluster Labeling:** the process of dividing all the ‘liquid’ pores and throats of the network into different clusters.

## 1.4 Literature Review

One of the earliest discrete methods is the pore network model developed by Nowicki, and it was used to determine the macroscopic properties a certain porous medium (Nowicki & Davis,

1992). Prat developed a pore network model based on the invasion-percolation (*I-P*) algorithm to simulate slow drying under isothermal conditions (Prat, 1993), in which the capillary and gravity forces were taken into account. This model was then used by Laurindo and Prat to study phase distributions and drying rate of porous media during the drying process. Comparison between the numerical and experimental results showed good match for the phase distributions (Laurindo & Prat, 1996), while for the drying rate and drying time, trends agreed with each other only qualitatively. The total drying time obtained through numerical simulations was several times larger than the experimental drying time (Laurindo & Prat, 1998).

Since then, many efforts have been made to improve the P-N model. The film effect has been added onto the P-N model (Yiotis, et al., 2004) (Prat, 2007). more and more physical phenomena are added on to the P-N model to improve it, including the film effect (Yiotis, et al., 2004) (Prat, 2007) and the viscous effect (Metzger, et al., 2007) (Metzger & Tsostas, 2008). And ignoring of the film effect was found to be the major reason responsible for the earlier-mentioned huge errors in the drying rates and drying times (Yiotis & Tsimpanogiannis, 2007). Besides, studies on the viscous effect show that when this effect is significant, the liquid-saturated portion of the pore network breaks into much more numerous, smaller clusters than the situations when the viscous effect is negligible. On the other side, these research efforts also verified that the I-P algorithm is valid when the viscous effect is small (Metzger & Tsostas, 2008). Beyond that, the thermal effect had also been studied (Huinink, et al., 2002).

These P-N models for drying yield some interesting insights when applied to the dual-scale porous media (Pillai, et al., 2009). Thin porous media, because of its special geometrical characteristics, yield some distinct transportation features of its own when they are simulated by the P-N models (Vafai, 2015).

With the introduction of a discrete approach in drying using the P-N model, some other problems also surface, for example, how to handle the coupling between the pore-scale P-N model and the lab-scale outside field, and how to simulate the coupling between a slow diffusion-dominated evaporation inside the network and a fast convection-dominated outside flow (Balhoff, et al., 2007) (Zenyuk, et al., 2015). (There are multi-scale problems existing in both space and time when solving the internal and external field simultaneously. The dimensions of pores are usually in microns, while the dimension of the whole porous medium is in tens of centimeters or even larger. The time to dry out a throat in the pore-network model could take dozens of minutes, while the time for the flow to sweep around the whole porous medium and take away the moisture is usually measured in seconds.)

Most early P-N model simulations on drying use a stand-alone porous medium without properly considering the surrounding environments. The mass transport between porous media and the outside environment is through an assumed constant-thickness concentration boundary layer (*CBL*) on the open side of the porous media. Through this boundary layer, the vapor molar concentration changes from a higher  $C$  value near the openings to the lower environmental

value  $C_\infty$  at the other side of the boundary layer. The mass transfer flux density,  $e$ , is calculated by

$$e = \rho_g D \frac{C - C_\infty}{\delta_\infty} \quad (1)$$

where  $\rho_g$ ,  $D$  are the gas phase density and diffusion coefficient of water vapor, respectively.

However, the actual *CBL* thickness is always changing with time and position, so the drying rate calculated in this way has unpredictable errors. Hence in recent years, more and more researchers are taking the outside flow-field simulation around the porous media into consideration during drying (Yiotis & Tsimpanogiannis, 2007) (Shaeri, et al., 2013). The turbulent flow effect around the porous medium is also taken into account. In these studies, the pore network and external fields are calculated using a split method. The detailed algorithm of the Beyhaghi's method can be summarized in Figure 4 (Beyhaghi, et al., Under Review).

For each drying step, the external water-vapor concentration field is calculated from a steady advection-diffusion equation given a

$$\mathbf{u} \cdot \nabla C = D \nabla^2 C \quad (2)$$

where  $\mathbf{u}$ ,  $C$ ,  $D$  are the velocity vector, vapor molar concentration, and diffusion coefficient of liquid vapor. The algorithm of this split method is complex because one needs to calculate the concentration twice in each sub-step.

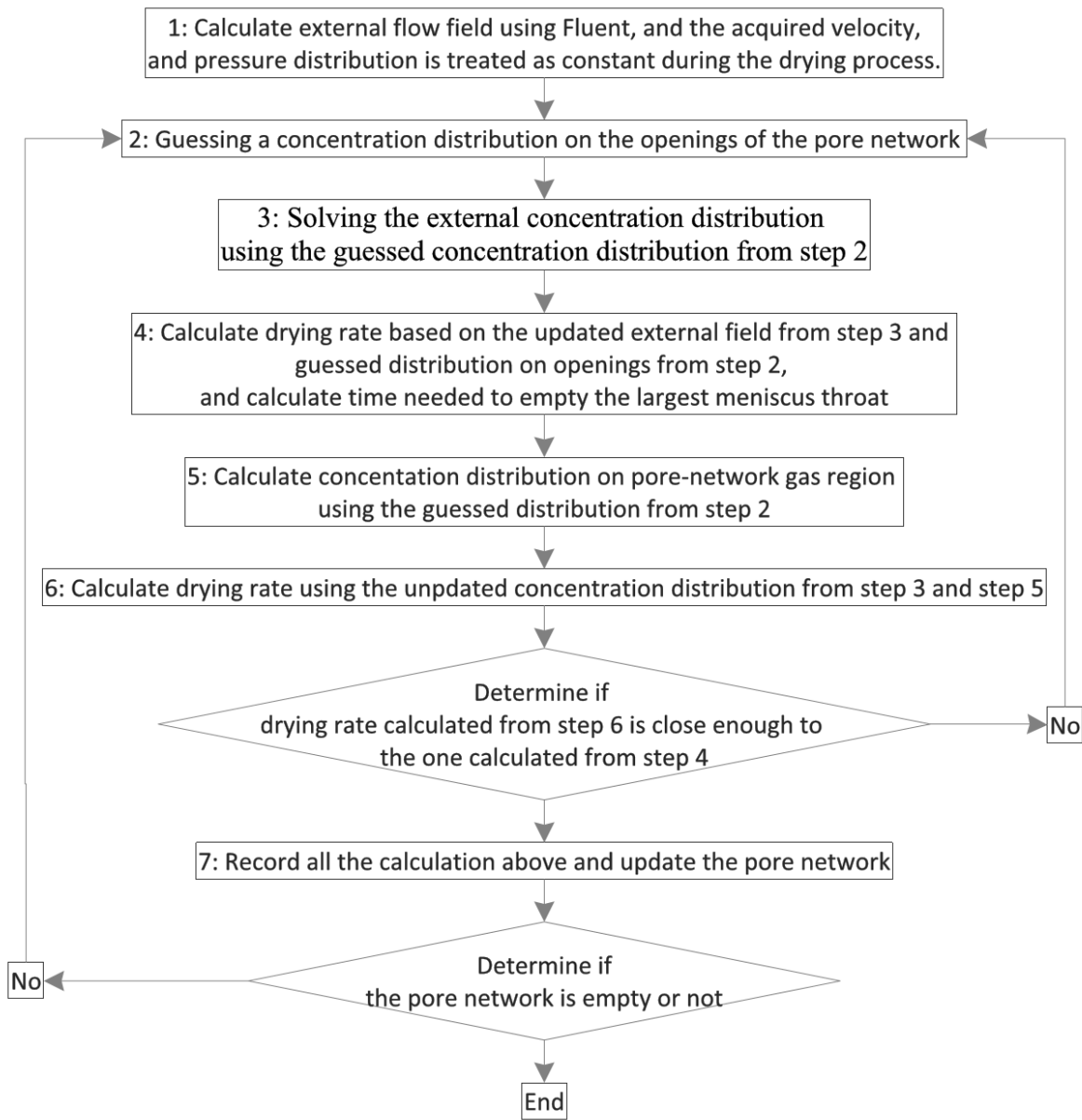


*Figure 4. Schematic of Beyhaghi's method*

## 1.5 Scope and Objective

Based on all these previous research efforts, the research work in this thesis is arranged as given below.



The first effort presents a new fully-coupled method and a new code implementation to simulate the slow drying problem of a porous medium (represented by a pore-network model) placed in a laminar air flow. The algorithm is more concise than the ones given in previous publications and can calculate the concentration changes in the pore network and external field simultaneously in real-time. In this work, factors having the potential to influence the simulations are studied further, such as: numerical algorithms, space discrete schemes, time step selection, mesh density at the interface of the external field and the network, the boundary layer above the open side of porous media, and the flow speed.

The adding of the film effect shortens the evaporation time by a factor of six (Laurindo & Prat, 1998), which makes the multi-scale problem addressed in this paper less serious. As a result, this first effort deliberately ignores the film effect so as to exaggerate the multi-time-scale problems. The idea is that if the treatments for multi-scale problems works for this exaggerated case, it should work well for other cases as well when other mitigating effects are added.

For the second effort, we inherited the fully-coupled, implicit method based drying code from our first model and added the crucial film effect onto its P-N model in order to make it more realistic.

The new model is used to study the drying of porous media when placed in a laminar flow field. This thesis will study the influence of microstructure, including the throat cross-section shape and throat size, on drying. By changing the aspect ratio of the pore network, drying of thin

porous media is studied. The effect of external wind direction and speed, the environmental vapor concentration, and the porous media openings are studied. At the end, the new model is applied to both regular and irregular dual-scale porous media. The results are compared with the published experimental results. *We believe this is the first and only the effort of this kind done till date.*

The scope and objectives of this thesis are summarized as follows:

1. *Develop a fully-coupled implicit model without the film effect to study the influential factors in the multiscale pore-network drying problems.*
2. *Include the film effect onto the method developed above.*
3. *Implement both methods using C++ with object-oriented programming (**OOP**) technology. (The developed software is named as **PORODRY<sup>TM</sup>**)*
4. *To apply the new model to study the effect of pore-network microstructure, the drying in thin porous media, the drying in dual-scale porous media, and the effect of irregular pore network.*

## **1.6 Outline of the Thesis**

Based on the thesis synopsis presented above and the studies carried out during the PhD program, the contents of this thesis are arranged in the following way:

Chapter 1: The background and previous research work on modeling drying using the P-N models were discussed. The coupling between the pore-level drying dynamics with

the external lab-scale flow field is chosen as the research direction for the thesis.

Chapter 2: The coupled method is formulated for predicting liquid redistribution and vapor transport inside the porous media and vapor transport in the external flow field. Here, the pore-network model without film effect is used to solve the drying problem.

Chapter 3: The implementation of the formulations in Chapter 2 is validated through a wide range of comparisons with the previous theoretical and experimental results.

Chapter 4: The methods described in Chapter 2 is used to study some topics, including mesh refinement, time step selection, influence of wind speed, and influence of microstructure.

Chapter 5: The film effect is added to the formulation of Chapter 2, and the fully-coupled method is reformulated.

Chapter 6: The methods described in Chapter 5 is tested under different numerical settings.

Chapter 7: The methods described in Chapter 5 is applied to study the influence of pore-network microstructure on drying.

Chapter 8: The methods described in Chapter 5 is applied to study drying in thin porous media.

Chapter 9: The methods described in Chapter 5 is applied to study drying in dual-scale porous media.

Chapter 10: The summary and conclusions of the current research is discussed; concerns and

future research directions is presented.

## 2 FORMULATION I: P-N MODEL FOR DRYING WITHOUT THE FILM EFFECT

The simulation of any isothermal drying of porous media in laminar flow can be de-coupled into two stages: the flow simulation of the external field, and the evaporation simulation in both the external flow-field and within the pore-network. The reason for such a decomposition is stated in the following section.

### 2.1 Modeling of the External Flow Field

The external region of a drying porous medium is a normal lab-scale flow field where the Navier-Stokes (N-S) equations for incompressible laminar flow apply. Under isothermal conditions, the energy equation can be ignored, so only the mass and momentum conservation equations are considered.

Mass Conservation:

$$\nabla \cdot \mathbf{u} = 0 \quad (3)$$

Momentum Conservation:

$$\rho_g \left( \frac{\partial \mathbf{u}}{\partial t} + \mathbf{u} \cdot \nabla \mathbf{u} \right) = -\nabla p + \mu_g \nabla^2 \mathbf{u} \quad (4)$$

Here  $\mathbf{u}$  is the velocity vector,  $p$  is the pressure,  $\rho_g$  and  $\mu_g$  are the density and dynamic viscosity

of the gas.

The gas considered is a mixture of dry air and water vapor. Theoretically, the gas density and viscosity will change with vapor concentration. But in our cases, this change can be ignored. For example, the humid air density can be expressed as

$$\rho_g = \frac{(p_a - p_v)M_d + p_v M_v}{\mathcal{R}T} \quad (5)$$

where  $p_a$ ,  $p_v$  are the atmosphere pressure and vapor partial pressure, respectively;  $M_d = 0.028964 \text{ kg/mol}$  and  $M_v = 0.018016 \text{ kg/mol}$  are the molar mass of dry air and water vapor, respectively;  $\mathcal{R} = 8.314 \text{ J/(K} \cdot \text{mol)}$  is the universal gas constant. Evaluating this equation using the standard atmosphere table, we can confirm that at any place on the earth with altitude below 4500 meters and with temperature below 40°C, the variation of humid-air density is well below 5% no matter how large the vapor concentration. The viscosity shares the same fate (Tsilingiris, 2008). Hence there is no need to simulate the external flow at each time-step during the entire drying process. Instead, the flow field is calculated only once at the beginning of the evaporation simulation.

The SIMPLE algorithms are used to solve equations (3) and (4) numerically. Two space discretization schemes, the Hybrid scheme and the Hayase QUICK scheme (Patankar, 1980) (Versteeg & Malalasekera, 2007), are tested for the convection term. As for the diffusion item, the central scheme is used.

## 2.2 Evaporation Modeling

There are two evaporation regions: the external flow field, and the internal pore-network. Continuum hypothesis is applicable to both these regions.

The continuum hypothesis applied to the lab-scale external field is obvious, but not so for the pore network. Inside the micro-meter size pore-network throats, the Knudsen number ( $Kn = \lambda/\delta^*$ , where  $\lambda$  is the molecule mean free path, and  $\delta^*$  is the representative physical length scale) is calculated to be well below  $10^{-3}$  by dividing the air molecule mean free path by the throat mean diameter (Shaeri, 2012). And if the throats are still filled with water, the Knudsen number will be even smaller because the molecular mean free path of water molecule is smaller. So, during the drying process, the Knudsen number is always far smaller than 1, which ensures the applicability of the continuum hypothesis inside the pore network model.

## 2.3 Physics of Evaporation in the External Flow Field

Using the continuum hypothesis, the evaporation outside is modeled using the unsteady convection-diffusion type conservation equations for molar concentration of vapor:

$$\frac{\partial C}{\partial t} + u \frac{\partial C}{\partial x} + v \frac{\partial C}{\partial y} = D \left( \frac{\partial^2 C}{\partial x^2} + \frac{\partial^2 C}{\partial y^2} \right) \quad (6)$$

Here  $C$  is the vapor molar concentration and  $D$  is the wet-phase mass diffusivity for water. (Some papers (Shaeri, et al., 2012) have also used the vapor pressure as the variable, the

relationship between vapor molar concentration and vapor pressure following the ideal gas law

$$C = p_v / \mathcal{R}T \text{ .)}$$

### **2.3.1 Physics of Modeling Evaporation in Pore Network**

As the drying progresses, the pore network model begins to witness the intrusion of the outside gas phase into the hitherto fully-saturated liquid region. With time, patches of both the gas and liquid regions appear in the pore-network model. In the gas region, the mass is transported mainly by gas diffusion; in the liquid region, the mass is redistributed mainly by capillary-pressure driven liquid flow (Prat, 1993).

Previous research has shown that the gravity, viscous and film effects have important influences on the drying pattern and drying rate of the pore-network model (Prat, 1993) (Yiotis & Stubos, 2001). Without the inclusion of the film effect, the total drying time predicted by the simulations is usually six times larger than seen in the experiments. The adding of the film effect corrected this error significantly, so among all these P-N developments, the most significant is the adding of the film effect. However, this doesn't bring any intrinsic changes to the multi-scale problem, but only makes it less serious in the time scale. So, to serve this chapter's purpose of studying the factors influencing the multi-scale problem better, the film effect is ignored deliberately. If this proposed method is applicable to the large time-scale difference between the pore-network and external field simulations without the film effect, it should work for the smaller time-scale difference between the two after the adding of the film effect. In the present work, we



assume the network is laid horizontally, so the gravity is also neglected (Laurindo & Prat, 1996) (Laurindo & Prat, 1998). By making these simplifications, we put our work's emphasis on the mass-transfer process between the P-N model and the outside field, and the numerical methods employed to solve them.

In the pore-network gas region, the convection effect is ignored due to the tiny geometry inside the pore-network and the resulting negligible velocities (Shaeri, et al., 2013). And because the pores have no volume, mass flux in gas pores with unknown vapor pressures follows the concentration balance equation

$$\sum_j \dot{m}_{ij} = \sum_j MD \frac{A_{ij}}{\delta_{ij}} (C_j - C_i) = 0 \quad (7)$$

where  $M$  is the molar mass of the vapor, and  $A_{ij}$ ,  $\delta_{ij}$  and  $\dot{m}_{ij}$  are the throat area, throat length and the mass flux, respectively, between the pores  $i$  and  $j$ .

In the pore-network liquid region, because of all the simplifications we made, the liquid redistribution simply follows the I-P rule presented in (Prat, 1993).

The liquid (gage) pressure for the wetting liquid considered (water) is related to the surface tension through the Laplace's Law as

$$p_l \propto -\frac{\gamma}{R} \quad (8)$$

where  $p_l$  is the liquid pressure,  $\gamma$  is the surface tension, and  $R$  is the radius of the throat. This

implies that a larger throat has a smaller negative (suction) pressure and vice versa, and this larger pressure difference between the larger and smaller throats will always pump liquid from the larger throats to the smaller ones.

When the network is drying, it will be invaded by air, and the liquid phase will be divided into many liquid clusters by the gas phase, a mixture of air and liquid vapor. Each cluster dries through all of its liquid-gas interfaces, the so called menisci throats, but no matter where the evaporation happens, the liquid in the largest throat of each cluster's menisci will be pumped by liquid pressure differential to supply the liquid to the smaller throats. Hence the largest throat on the interface of each cluster will always be emptied first. This rule is called the I-P rule and the process of finding clusters and their menisci during each time-step is called cluster labeling.

## **2.4 Coupled Solution for Vapor Concentrations in the External Field and Pore-Network**

Previous researchers solved the evaporation equations for the outside flow field and pore network separately (Shaeri 2012) (Shaeri, et al., 2013) (Beyhaghi, et al., Under Review). In this work, we align the outside field cells with the pore network model's pores and throats, as shown in Figure 5. Schematic grid layout for the coupled solution for vapor concentrations in the external flow-field and pore network, and propose a novel approach of solving concentrations in the two regions simultaneously. We can combine equations (6) and (7), and solve them using a fully

coupled method. The combined equation actually has a form similar to that of equation (6):

$$\frac{\partial C}{\partial t} + u \frac{\partial C}{\partial x} + v \frac{\partial C}{\partial y} = \sum_j MD \frac{A_{ij}}{\delta_{ij}} (C_j - C_i) \quad (9)$$

in which, the pores too are treated as finite volume cells, as in the external field cells; the main difference is that the volume of pores is zero, and the velocity inside the pore-network is also neglected. Another difference is that when calculating the right side diffusion term, the diffusion not only happens between two neighbor cells or between two neighbor pores, but also happens between cells and pores as shown in Figure 5.

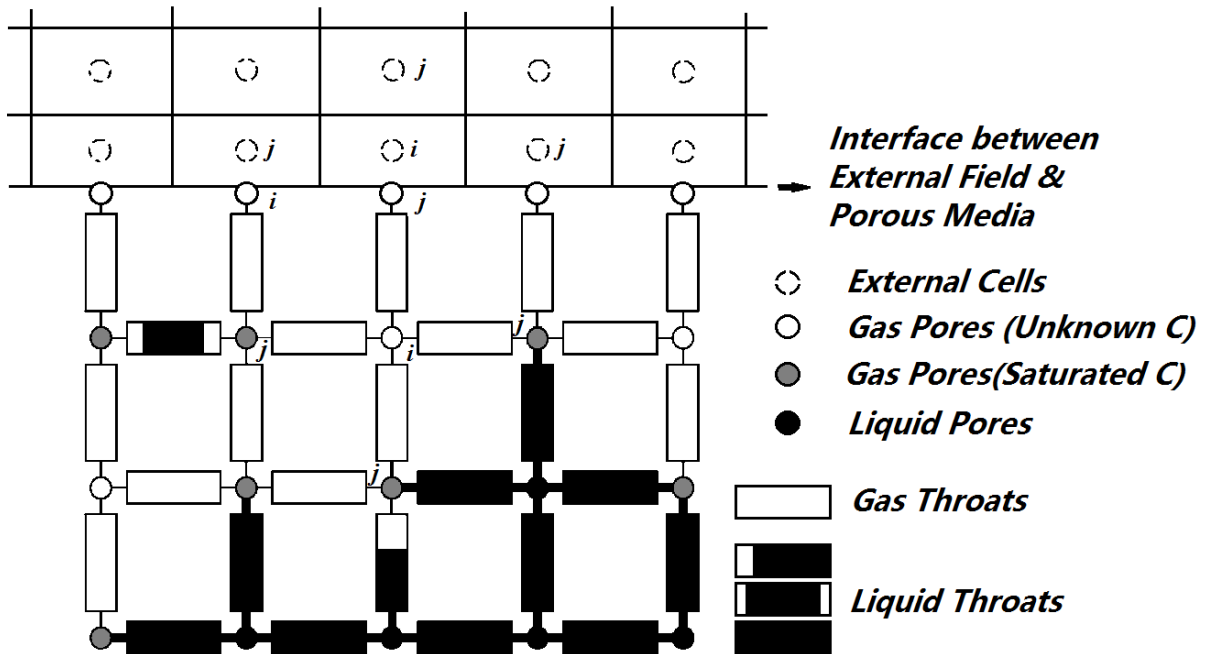


Figure 5. Schematic grid layout for the coupled solution for vapor concentrations in the external flow-field and pore network - without film effect

When  $i$  indexes an external cell,  $j$  could index either a neighboring external cell or a neighboring pore, or, when  $i$  indexes a pore,  $j$  could index either a neighboring pore or an external neighboring cell. The P-N opening pores can be offset slightly inward to avoid putting them right on the face of the external cells, which is not helpful when calculating the flux between the pore and cells.

In this coupled approach, the convection terms are discretized by the Hybrid scheme or Hayase QUICK scheme, and the diffusion terms are discretized by the central scheme.

### 2.4.1 Operator-Splitting Algorithm

Because of the concern about generating false diffusion at high Peclet-Number conditions (Muralidhar, et al., 1993), the operator-splitting algorithm is also tested to solve equation (9), which is transformed from a one-step algorithm into a two-step algorithm as follows:

The first step is to calculate the changes in vapor concentration due to the convection terms only:

$$\frac{\partial C}{\partial t} + u \frac{\partial C}{\partial x} + v \frac{\partial C}{\partial y} = 0 \quad (10)$$

And the second step is to calculate the same changes due to the diffusion term only:

$$\frac{\partial C}{\partial t} = \sum_j MD \frac{A_{ij}}{\delta_{ij}} (C_j - C_i) \quad (11)$$

Note that the evaporation from the pore-network only happens in the diffusion step.

In the operator-splitting algorithm, the first and the second steps can be switched; which one goes first, the convection equation or the diffusion equation, will influence the calculation stability and the results itself. In this paper, we tested all the three methods: the non-operator-splitting algorithm, the convection-diffusion-splitting algorithm, and the diffusion-convection-splitting algorithm, and the results are analyzed in the following sections.

## 2.5 Non-Dimensionalization of Equations

In this thesis, we used the dimensionless forms of all the above-given equations to do the calculation in order to reduce truncation errors as the non-dimensionalization process keeps the variable values close to unity and prevent very small values to appear during computations. However, the characteristic or reference values are chosen so that they are suitable for both the external lab-scale and internal pore-scale regions. But the derived dimensionless numbers have no physical meaning apart from rendering our calculations unit-less, because no combination of characteristic values can be found to simultaneously reflect the features of the external air flow, the external evaporation, the internal liquid flow and the internal evaporation.

In this thesis, two common dimensionless numbers will be used:

$$\text{Reynolds Number: } Re = \frac{\rho^* U^* l^*}{\mu^*} \quad (12)$$

$$\text{Peclet Number: } Pe = \frac{U^* l^*}{D^*} \quad (13)$$

The symbols with \* superscript represent the characteristic values. These values are different from the ones used in the field computations and are chosen to reflect the physics features and will be specified for each case.

## 2.6 Summary of Algorithm

The algorithm for the whole simulation can be described as follows:

1. Solve equations (3) and (4) to get the external flow field. Assume that the flow field variables, the outside velocity and pressure, are fixed during the following steps. Initialize the liquid-saturation distribution in the pore-network, and the vapor concentration distribution in the gas region.
2. Do cluster labeling for the pore-network.
3. For each cluster, calculate the drying flux and then the time needed to empty the largest meniscus throat—find out the minimum value among them for all the clusters, and set it as the time step.
4. Implicitly solve equation (9) to get the vapor concentration distribution. Repeat the calculation for Step 3 above and compare the result with the previous time-step obtained in Step 3. If the difference between them is smaller than the convergence criterion, then proceed to step 5; otherwise set a new time-step and do this step again.
5. Empty the throat using the time step calculated in step 4.
6. Check the saturation of the pore-network. If it is still wet, then go back to step 2; otherwise finish the computation.

For a better comparison with the Beyhaghi's method, the new algorithm is depicted in Figure

6. A careful comparison will show that it is more concise than the previous method.

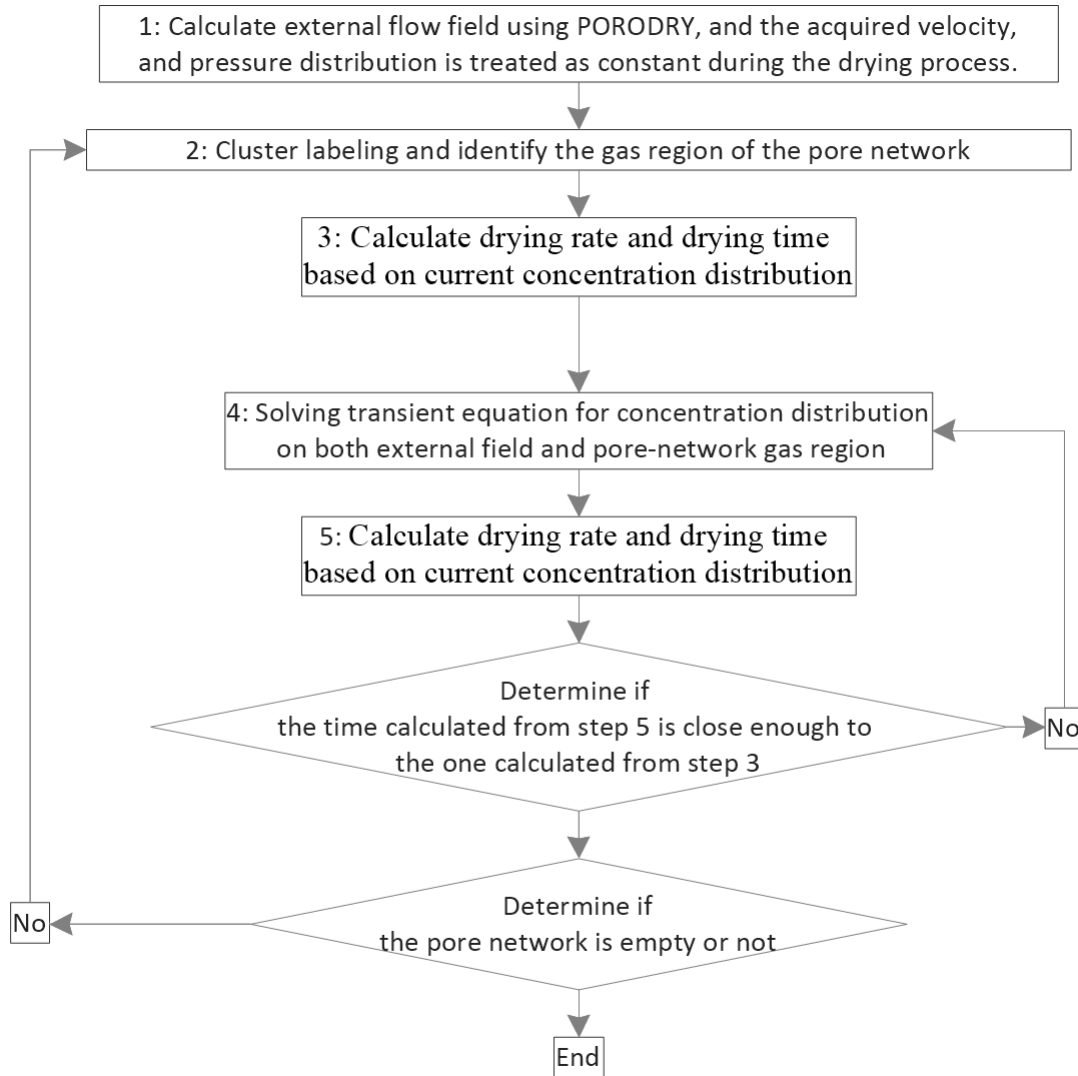


*Figure 6. Schematic of drying algorithm presented in this work*

### 3 VERIFICATION OF NUMERICAL SIMULATION

We designed four different verification cases to validate different aspects of our numerical solution and its code implementation, and these are summarized in Table 1.

*Table 1. Summary of verification cases*

Verification Case #	General Description
1	Slit flow; $Re = 1000$
2	Backward-step flow; $Re = 805$
3	Advection of Gaussian (bell-shaped) solute concentration profile in flow; $Pe = 1$ , $Pe = 100$
4	Drying of a $20 \times 20$ pore-network with one side open to the constant environment vapor concentration $C_\infty = 0$ .

Verification 1 is a 2-D incompressible laminar slit-flow, where there is a theoretical result available for comparison. Verification 2 is a 2-D backward-step flow, and the results are compared with a previous experiment and simulation (Lee, 1998). These two cases are chosen to verify our N-S equations solver for the outside flow-field, which is the first step of our proposed algorithm. Verification 3 is to simulate a transient 1-D species advection problem such that the results are compared with a theoretical solution (Muralidhar, et al., 1993). This is used to test the accuracy of the solver for solving equation (9) using the operator-splitting method based on equations (10) and (11). Verification 4 uses the results of a previous pore-network model (Shaeri, 2012) to examine our I-P algorithm implementation and thus establish the accuracy of our P-N simulation.



### 3.1 Slit Flow

Verification 1 is using a 2-D incompressible laminar flow in a slit between two parallel plates to test the N-S solver with its Hayase QUICK scheme and SIMPLER algorithm. To simulate a fully-developed slit flow, the periodic boundary conditions are set on the inlet and outlet sides of the tunnel, and the inlet side is given a higher pressure while the outlet side is given a lower pressure. No-slip wall boundary conditions are applied on the top and bottom sides, as shown in Figure 7.

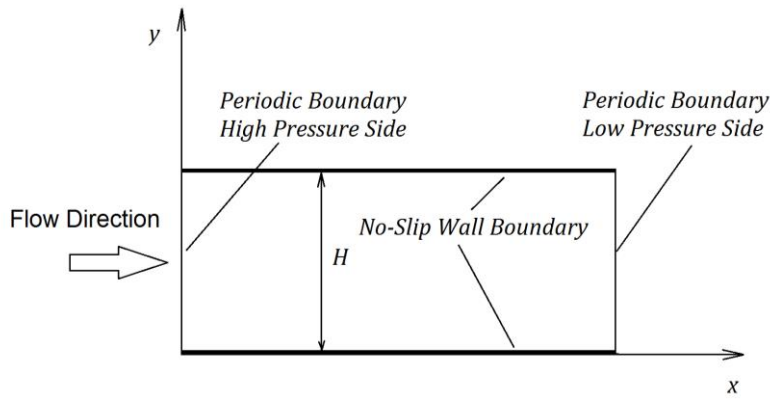


**Figure 7. A schematic describing the geometry and boundary conditions of the considered 2-D slit flow**

In this verification, the distance between slits  $H = 0.1 \text{ m}$ ; the tunnel length is set equal to  $H$ ; pressure difference between the inlet and outlet is  $0.0003276 \text{ Pa}$ ; the fluid is air with its density as  $\rho_{air} = 1.204 \text{ kg/m}^3$ , and dynamic viscosity as  $\mu_{air} = 1.813 \times 10^{-5} \text{ Pa} \cdot \text{S}$ .

The analytical solution to this problem is:

$$u(y) = \left(-\frac{dp}{dx}\right) \frac{H^2}{8\mu} \left[1 - \left(\frac{y}{H/2}\right)^2\right] \quad (14)$$

According to equation (14), the peak velocity for this case is  $0.2259 \text{ m/s}$  while the average velocity is  $U_{avg} = 0.1506 \text{ m/s}$ . As expected, the peak velocity is 1.5 times the average velocity.

The Reynolds Number  $Re = \rho_{air}U_{avg}H/\mu_{air} = 1000$ .

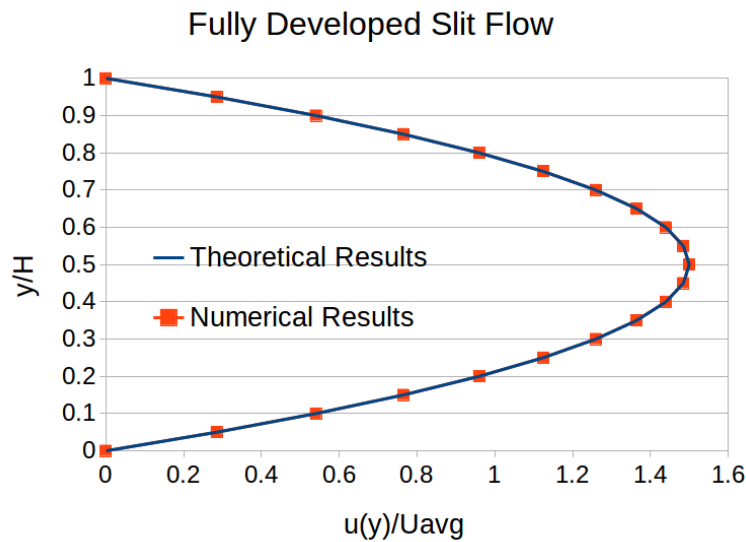


**Figure 8. Velocity profile comparison between theoretical and numerical results**

The comparison between the numerical and theoretical results is presented in dimensionless form in Figure 8. The numerical results agree perfectly with the analytical results, thus establishing the accuracy of our numerical solution for steady-state laminar flow in 2-D.

### 3.2 Backward-Step Flow

Verification 2 is using a 2-D incompressible laminar flow in backward-step geometry, as shown in Figure 9, to test the N-S solver with its hybrid scheme and SIMPLE algorithm.

The backward step geometry is chosen, because it is widely studied through experiments and

numerical simulations. By doing this verification, we can examine the ability of our implementation to capture the detachment of channel flow at the back of the step and subsequent re-attachment.

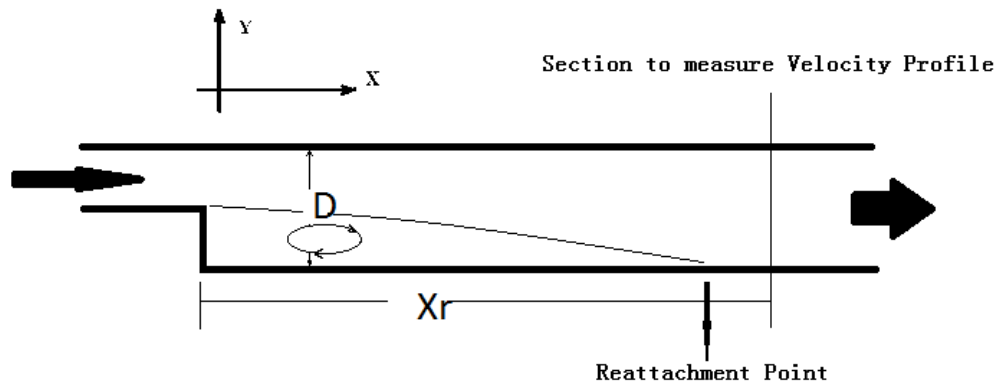


**Figure 9. A schematic of the backward-step flow geometry**

As shown in Figure 9, the tunnel height after the step,  $D$ , is  $0.03\text{ m}$ ; the tunnel height before the step is  $D/2$ . The tunnel walls have no-slip wall boundary conditions. The flow's inlet average velocity is  $U_{avg} = 0.4041\text{ m/s}$  and the fluid is air just the same as that in Section 3.1. So the Reynolds number  $Re = \rho_{air}U_{avg}D/\mu_{air} = 805$ . To make the results comparable to the experiment and simulation by (Lee & Mateescu, 1998), the inlet velocity is not uniform—instead it is assigned the fully-developed velocity distribution calculated from equation (14).

Figure 10 shows the velocity contour of our numerical simulation. Note that there are three cross sections after the step; their locations are  $x = 5D$ ,  $x = 6D$ ,  $x = 7D$ , and they are marked respectively as black, red and blue lines. Their colors correspond with the colors used in Figure 11, which shows the velocity profiles at the said cross sections.

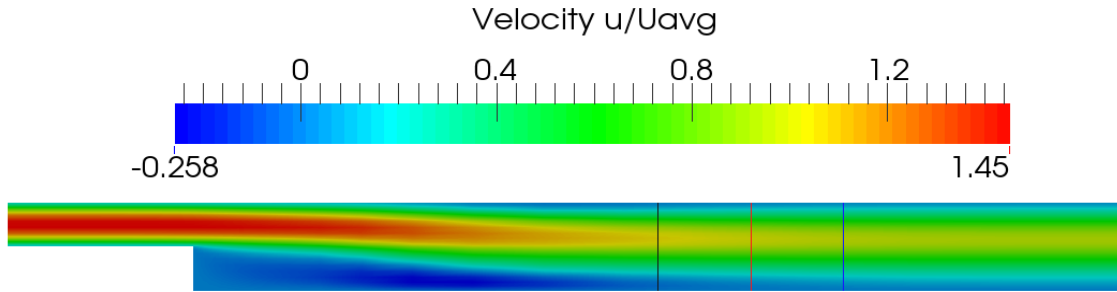


**Figure 10. Velocity contour for the backward-step flow**

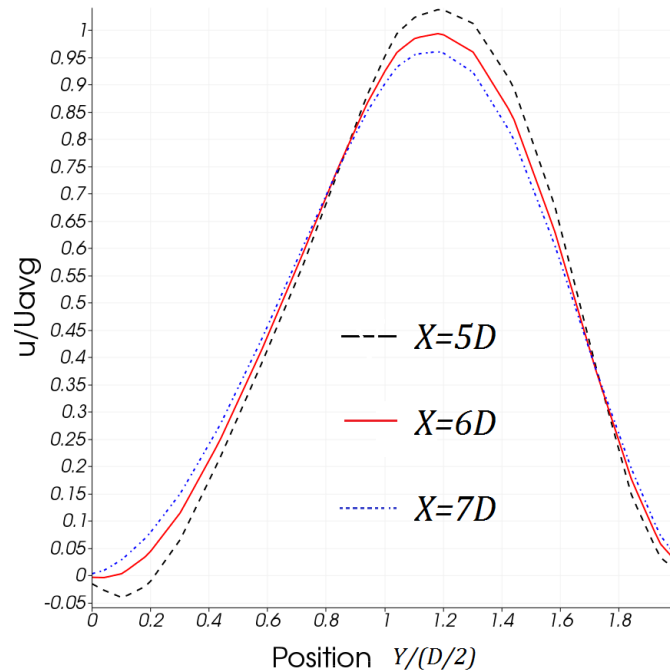


**Figure 11. Numerically obtained backward-step flow velocity profiles at different cross-sections**

In Figure 11, the lower left corner at  $Y = 0$  is the velocity near the lower wall of the tunnel. We observe that the velocity turns from negative to positive right between section  $x = 6D$  and  $x = 7D$ , which implies that the reattachment point is located between these two sections. This result is almost identical to the numerical results presented by Lee & Mateescu and is only a little off from their experimental result of  $7D$ . This means our numerical implementation of the outside

flow involving complex flow-circulation and flow-reattachment physics is quite accurate, and it allows us to believe that our external-flow simulation can handle much more complex flow geometries than currently used.

### 3.3 Advection of a Gaussian Concentration Distribution

Verification 3 uses a 1-D salute transport problem with analytical solution to compare with the results from our code to examine the accuracy of the operator-splitting solver of equations (10) and (11). This is a 1-D advection problem along the  $x$  axis as shown in Figure 12. We set an initial Gaussian or bell-shaped concentration distribution on the left side of the 1-D domain. As time goes by, the Gaussian distribution will dissipate and will be pushed to the right due to fluid flow from the left side.

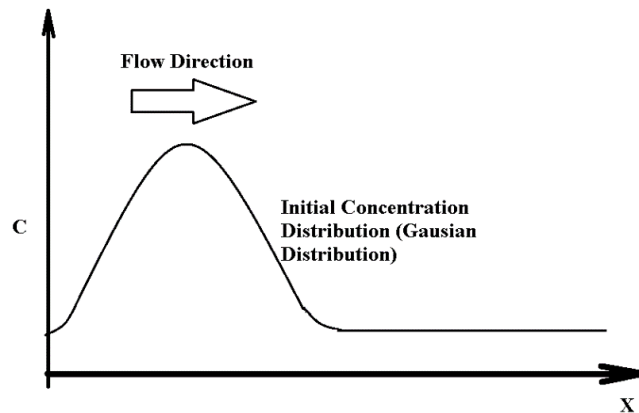


**Figure 12. Schematic description of the code verification carried out by using the advection of Gaussian concentration distribution**

The results of this problem can be calculated by numerically solving equations (10) and (11). Its theoretical solution (Muralidhar, et al., 1993) is given as:

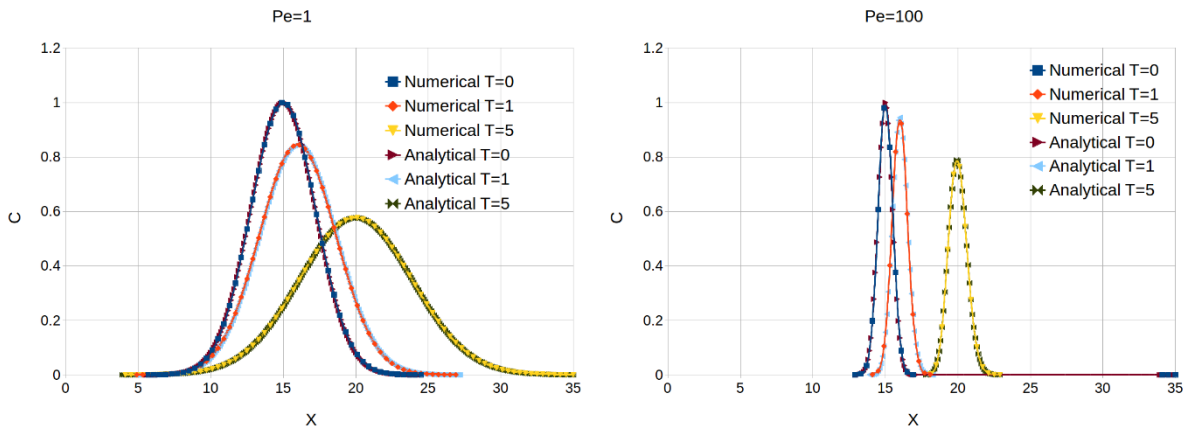
If the Initial distribution is described as

$$t = 0, C(x, 0) = e^{-\alpha(x-x_0)^2} \quad (15)$$

in which  $\alpha$  is a constant parameter for controlling the width of the bell-shaped curve and the  $x_0$  is a constant locating the center of the curve. The analytical solution to this problem is given as

$$C(x, t) = \frac{1}{2} \sqrt{\frac{Pe}{\pi t}} e^{\left(\frac{x-t}{2}\right)^{Pe}} \int_0^x F(x, y, t) dy \quad (16)$$

$$F(x, y, t) = e^{-\alpha(y-x_0)^2 - \frac{yPe}{2}} \times \left[ e^{-(x-y)^2 \frac{Pe}{4t}} - e^{-(x+y)^2 \frac{Pe}{4t}} \right]$$



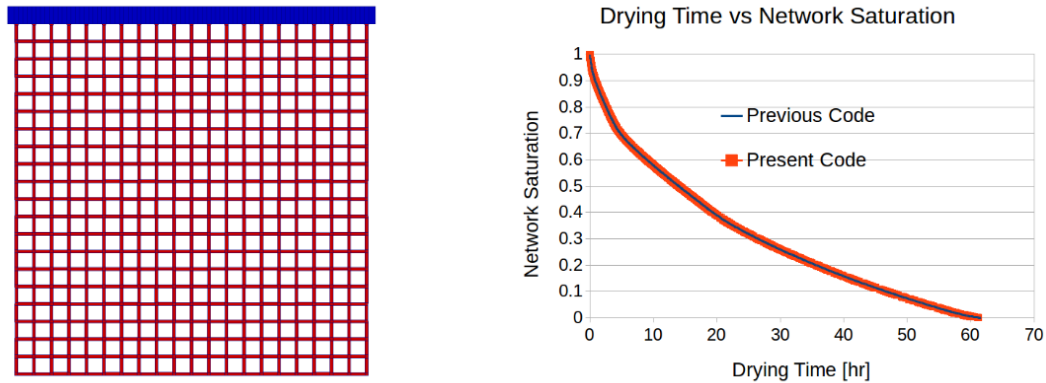
**Figure 13. Advection of Gaussian concentration distribution (Left  $Pe = 1$ , right  $Pe = 100$ ): a comparison of the numerical solution with the analytical solution**

Figure 13 compares the analytical solution, equation (16), with the numerical results obtained from solving equations (10) and (11) for two different Peclet number values. We observe that at the higher  $Pe$  with advection dominant, the curves seem to be translating downstream with the flow. However, at lower  $Pe$  with diffusion dominant, the curves seem to be rooted on the left side and seem to be merely stretching with time. But both sets of curves show a decay in the maximum

height with time, the lower  $Pe$  being more so. But it is heartening to note that the numerical results match perfectly with the analytical solutions for the considered high and low  $Pe$  cases.

### 3.4 Verification of the I-P Algorithm Based Network Drying Module

To validate our I-P algorithm based numerical code for simulating drying inside the pore-network, we compared our results with the results obtained by our previous, independently-developed code (Shaeri, 2012).



**Figure 14. Verification of drying physics implementation (left: calculation domain; right: drying time-vs-network saturation plot)**

This is a  $20 \times 20$  network with one side open to the environment of constant species (water vapor) concentration set equal to 0, as shown in Figure 14. The left side shows that initially the network is filled with liquid, colored as red; and the environment concentration is set as a constant of 0, colored as blue. The right side plots the drying time-vs-network saturation. The network saturation is defined as the ratio of the liquid mass present currently in the network versus the liquid mass corresponding to the fully-saturated network. The results from the present code match

perfectly with the results obtained from the previous code, thereby established the accuracy of our numerical implementation of the I-P algorithm.



## **4 RESULTS FROM FORMULATION I AND DISCUSSIONS**

By doing these four previously-mentioned verifications, we examined the most critical solver in our algorithm, i.e., the solver of equation (9). The results were good, so it is reasonable to believe that the results of the whole simulation would be accurate to a large extent. The validated numerical implementation of the proposed algorithm is now used to study the slow drying problems of porous media in laminar flow.

The topics studied in this chapter include mesh refinement, time-step selection, space discretization schemes, operator-splitting/non-operator-splitting algorithms, influence of Peclet Number, and influence of pore-network structures.

### **4.1 Problem Description & Calculation Domain**

To study all the topics stated above, a calculation domain of pore-network laying under a slit is designed (Figure 15). The top of the porous medium opens to the external flow field. The dry air comes from the left side and flows laminarily toward the right side, and taking away the water vapors coming out of the porous medium.

There are two major reasons for choosing this geometry. Firstly, the slit flow has an analytical solution (velocity) for comparison. Secondly, the disturbance by the porous medium to the flow field is minimized, so the vapor concentration boundary-layer thickness is easy to control, which

gets thicker as the inlet velocity decreases. Despite this simplicity in simulation domain, it is possible for us to answer some important questions about the outside-inside coupling in drying simulations.

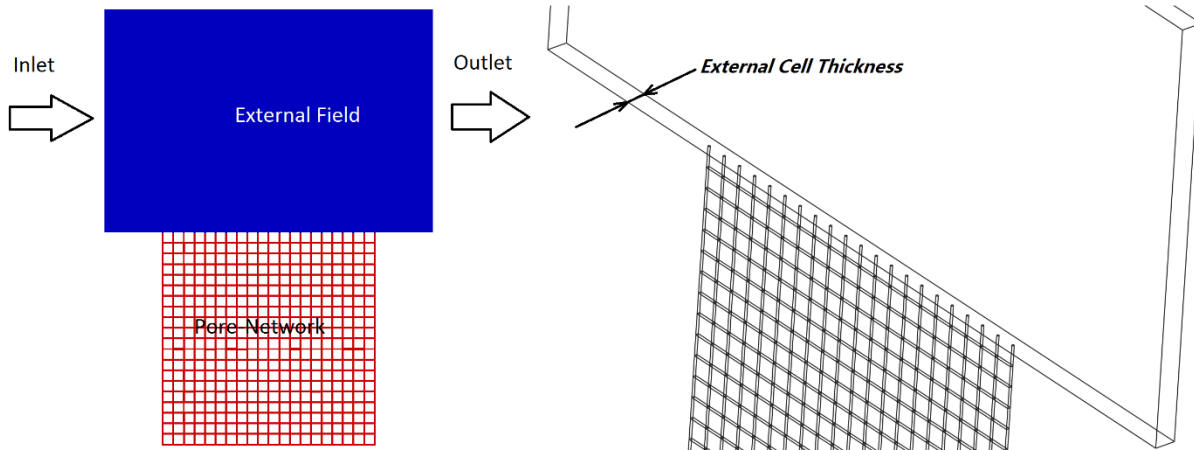


**Figure 15. Simulation domain and problem description**

The pore network has  $20 \times 20$  pores, and there are 820 throats connecting the pores. The throat lengths are set to a constant value of  $5 \times 10^{-4}$  m. The whole pore network is of the size  $0.0105$  m  $\times$   $0.0105$  m while the slit-tunnel height is set to  $0.0105$  m.

Note that the solver for pore network is 3D, which is required to simulate throats with different cross-sections, such as circle, hexagon, square, and triangle. However, the external field solver is 2D. To couple these two together, a thickness equal to the length of the throats is assigned to the external cells (Figure 15).

The throat diameter was randomly assigned with its average being  $9 \times 10^{-5}$  m. The specific diameter of each throat was assigned by a random function designed by us which was controlled

by two input parameters: the random seed number (RSN), and the maximum variation percentage (MVP) (which is the maximum a throat diameter can deviate from its average value).

The liquid inside the pore-network is water. The environment is set as the sea level and the room temperature at 20°C. Under these conditions, the fully-saturated-vapor concentration is  $C_{sat} = 0.9592 \text{ mol/m}^3$ . The external field has a flow coming from the left side, the velocity distribution is fully developed slit-flow which could be calculated from equation (14), in which  $\left(-\frac{dp}{dx}\right)\frac{H^2}{8\mu}$  is related to the average velocity which in turn is controlled by the Peclet Number. The inlet-velocity average is variable, but the vapor concentration of inlet air is set to be a constant at  $C_\infty = 0.2878 \text{ mol/m}^3 = 0.3 \times C_{sat}$ .

*Table 2. Material properties and parameter values used in the present work*

Air Density $\rho_g$	1.204 $kg/m^3$
Air Viscosity $\mu_g$	$1.813 \times 10^{-5} \text{ Pa} \cdot s$
Water Density $\rho_l$	998.2 $kg/m^3$
Water Viscosity $\mu_l$	$1.002 \times 10^{-3} \text{ Pa} \cdot s$
Water Vapor Mass Diffusivity $D$	$2.119 \times 10^{-5} \text{ m}^2/s$
Saturated Concentration $C_{sat}$	0.9592 $mol/m^3$
Surface Tension $\gamma$	$7.266 \times 10^{-2} \text{ N/m}$

For all the following cases, the average slit-flow inlet velocity is specified by Peclet Number.

The characteristic length used to calculate the Peclet number is the width of the pore-network (which is also the slit width), the characteristic velocity is the average inlet velocity, and the characteristic mass diffusivity is that of water:

$$Pe = \frac{U^* l^*}{D^*} = \frac{U_{InletAvg} l^*}{D}$$

The values of various material properties used in these calculations are summarized in Table 2. *These values are also used in all the rest simulations in this thesis if not specified specifically.*

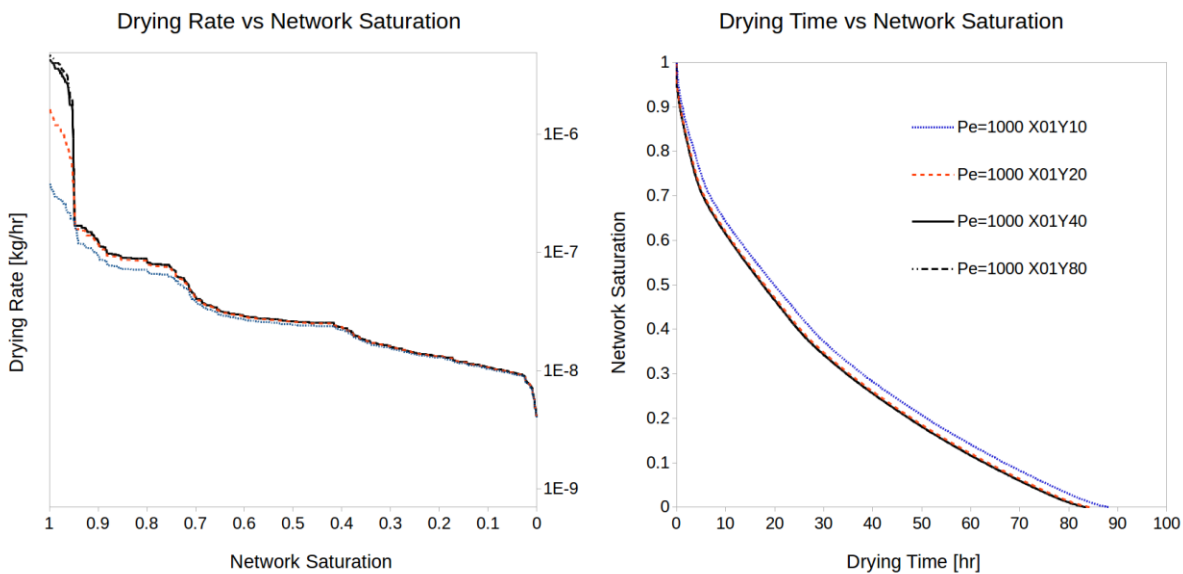
For all the following cases in this chapter, the default values of the parameters of the random number generator function are: RSN value is 1, MVP value is 5%. And the Environment Concentration  $C_\infty = 0.2878 \text{ mol/m}^3$ ; the Reference Length used when talking about Reynolds number is  $l^* = 0.0105 \text{ m}$ .

## 4.2 Mesh Refinement Study

Our previous research on coupling network model with the outside flow required a very fine outside mesh for simulation, in which several outside cells were required to be adjacent to each inside throat at the interface (Beyhaghi, et al., Under Review). This requirement is rather restrictive, so we examine this aspect again in another way. The previous work refined the mesh in both  $X$  and  $Y$  directions at the same time. In this paper, we instead refine the mesh one direction at each time in order to find out which direction's refinement influences the results the most.

Considering that the CBL thickness is very critical to the drying rate simulation (Beyhaghi, et al., Under Review), the  $Y$  direction mesh is refined first because it is related to the concentration boundary layer development. And later the  $X$  direction mesh is refined. For both these cases, the Peclet number is set to a large value, 1000.

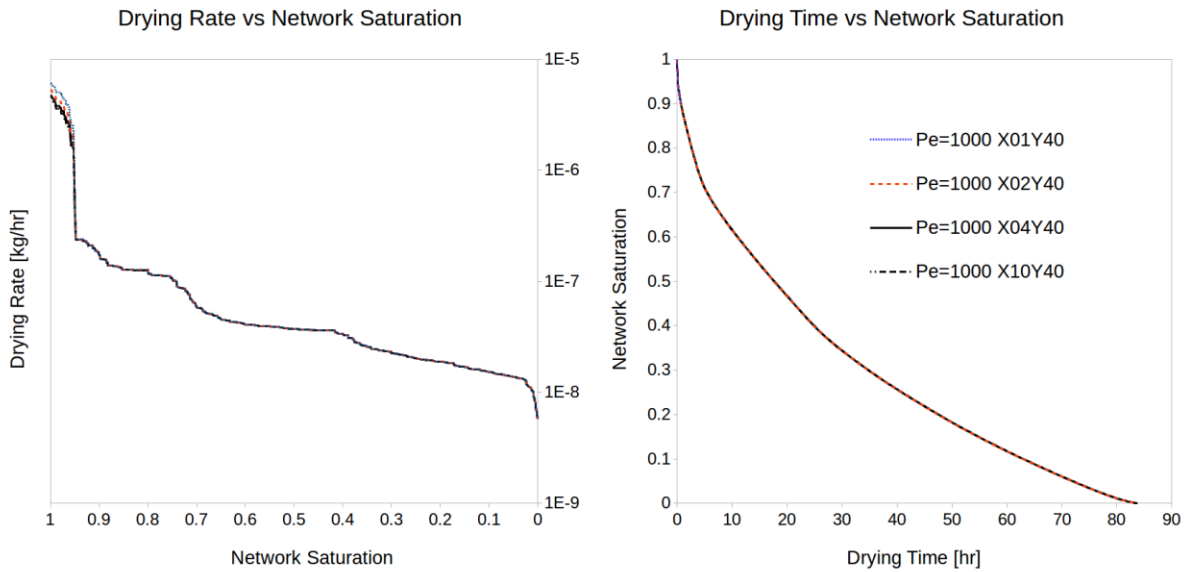
The results of the  $Y$  direction refinement are as shown in Figure 16. It is clear from the left graph that the  $Y$  direction mesh refinement is very critical to drying rate, especially to the drying rate of the early drying period. The  $Y$  direction mesh refinement has some influence on the total drying time, but the influence is not significant because only the early drying period is influenced by this numerical experiment.



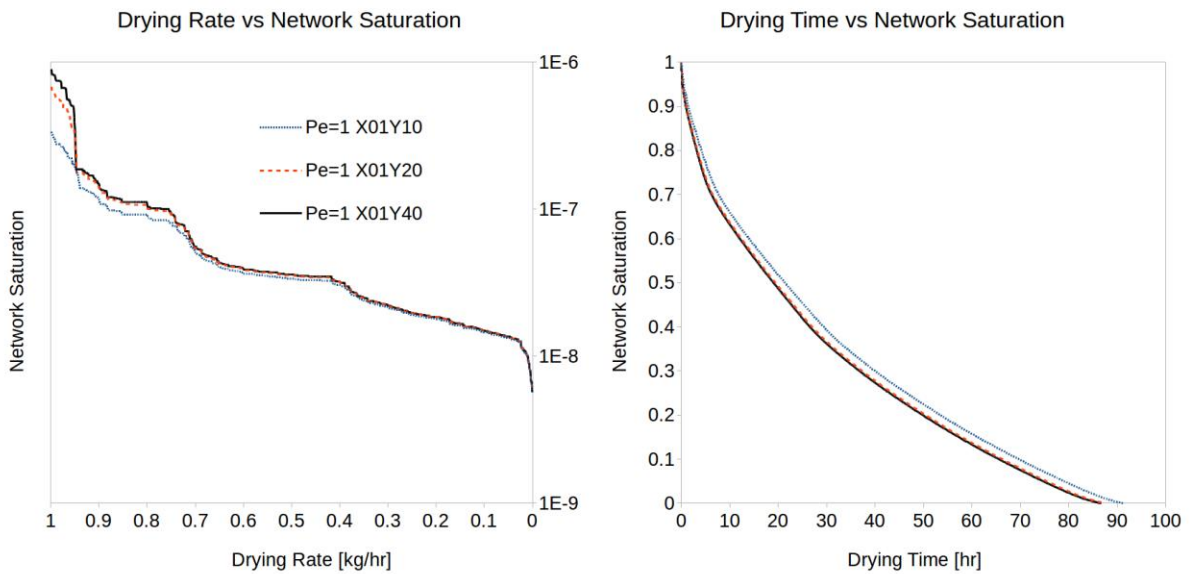
**Figure 16. Results of mesh refinement in the  $Y$  direction,  $Pe = 1000$  (Note:  $X04Y40$  means use parameter 04 for  $X$  direction meshing, and use 40 for  $Y$  direction meshing. Higher number implies denser mesh)**

Figure 17 shows the results of  $X$  direction mesh refinement. We observe that the  $X$  direction

refinement has negligible influence on the drying rate, even during the early drying period. As for the drying time, it remained almost unchanged. It is clear that the  $X$  direction refinement does not influence the results significantly and hence can be avoided.



**Figure 17. Results of mesh refinement in the  $X$  direction,  $Pe = 1000$**



**Figure 18. Results of Mesh Refinement in  $Y$  direction,  $Pe = 1$**

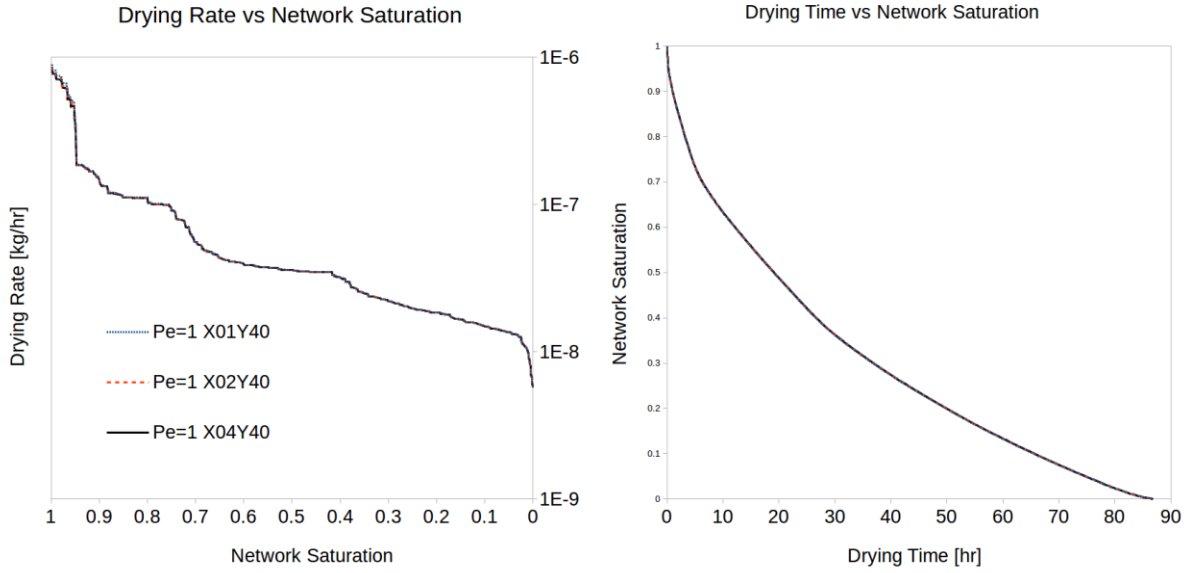


**Figure 19. Results of Mesh Refinement in  $X$  direction,  $Pe = 1$**

We also examined the same thing for  $Pe = 1$ ; the results, as shown in Figure 18 and Figure 19, show the same trend as mentioned above. Comparing Figure 18 and Figure 16, we can also observe that the difference between  $Pe = 1$  X01Y40 and  $Pe = 1$  X01Y20 is smaller than the difference between  $Pe = 1000$  X04Y40 and  $Pe = 1000$  X04Y20. This means that a coarser mesh is acceptable when computing the low Peclet-Number cases.

The final mesh chosen is as shown in Figure 20: it is less dense than the mesh used in Beyhaghi's work (Beyhaghi, et al., Under Review). And from the results, we conclude that only mesh refinement normal to the concentration boundary layer is critical to the evaporation results. And the mesh refinement influences the drying rate of the early period much more than that of the late period.

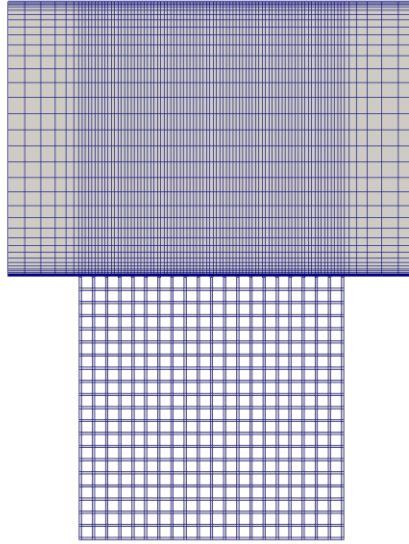


*Figure 20. The final chosen mesh for the coupled inner-outer flow drying simulation*

### 4.3 Time Step Selection

After doing the space mesh refinement, we ask if the time step refinement will have any effect. It is well known that the time for the network to dry out one throat (which is on the order of the time step for the internal drying simulation) is much longer than the time needed for the flow to sweep across the whole length of the porous medium. The question is whether we need to use finer time-steps for the external evaporation simulation compared to those for the internal drying simulation?

We examined this by using time sub-steps: we can set the external-field time-step exactly the same as the time to dry out one throat or set it to the latter's half by setting the number of sub-steps to be one or two, respectively. Figure 21 shows the results of both these cases, and they are exactly the same. This means that refining the time-steps for the concentration transport equation for the



outside flow is unnecessary. The success may be attributed to the implicit time-marching algorithm proposed in this paper.

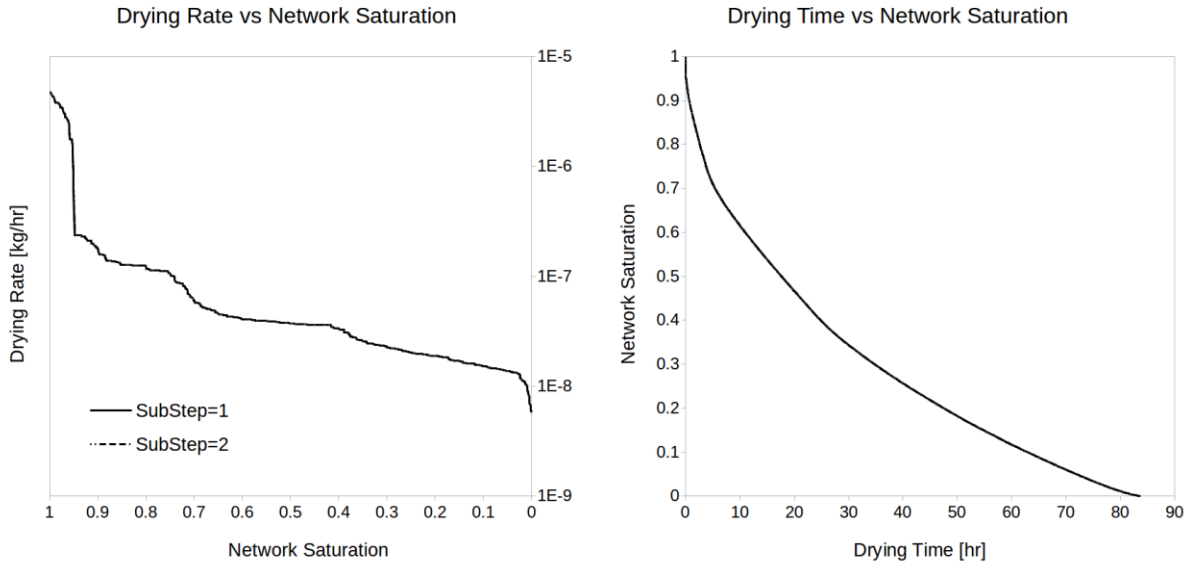


**Figure 21. Time step selection**

#### 4.4 Influence of Schemes for Space Discretization

This group of cases, we compared the Hybrid scheme with the Hayase QUICK scheme. These schemes were used to discretize the advection terms of equation (9). As shown in Figure 22, they both yielded identical results.

This comparison shows that for a simple case like drying in laminar flow between two slits, both Hybrid and QUICK schemes can get satisfactory results. This study will be carried chapter 5 again when the film effect is added and when the geometry is more complicated.

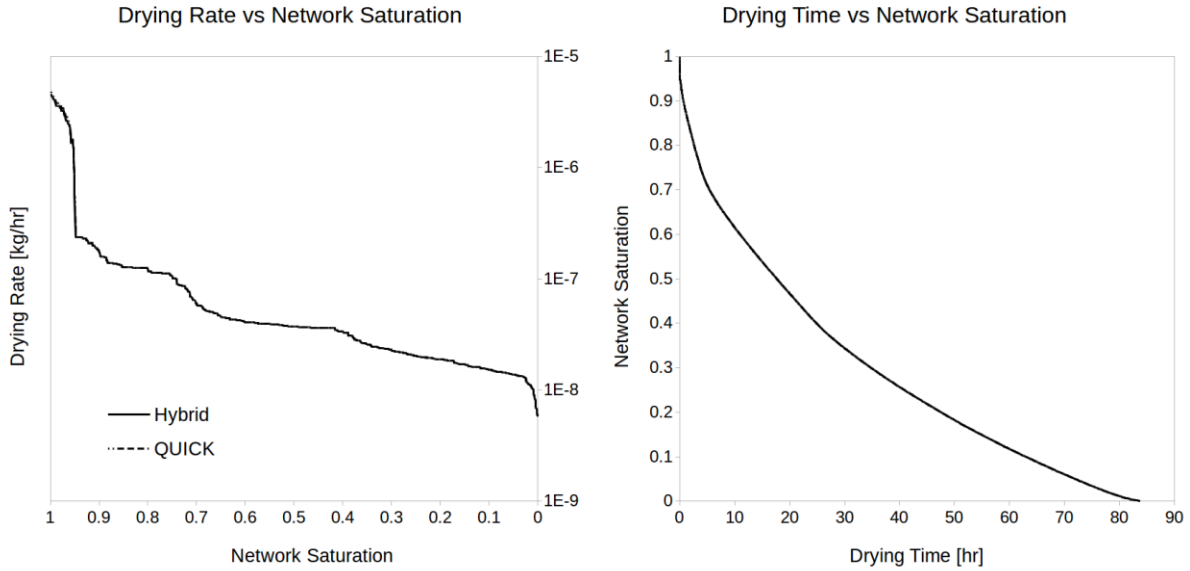


**Figure 22. Comparison between the hybrid and QUICK schemes,  $Pe = 1000$**

## 4.5 Operator-Splitting Method vs Non-Operator-Splitting Method

In this section, we compare two drying cases for  $Pe = 1000$  : One using the operator-splitting method and the other using a non-operator-splitting method, which implicitly solves the equation (9) as a whole.

Operator-Splitting method is widely adopted in high Peclet-Number mass transfer problems to increase numerical stability (Muralidhar, et al., 1993). Our implementation of the operator-splitting algorithm is also tested in the verification sections. However, from the results shown as in Figure 23, both the methods yield almost identical results, except the operator-splitting method is not as stable as the non-operator-splitting method used here.

Note that the operator-splitting method used in this comparison first calculates the convection

terms and then the diffusion terms. Another operator-splitting method, obtained by changing the order to first diffusion-then convection, was also tried, but the drying rate was found to be scattered over an undesirably large range, so it is not displayed here.

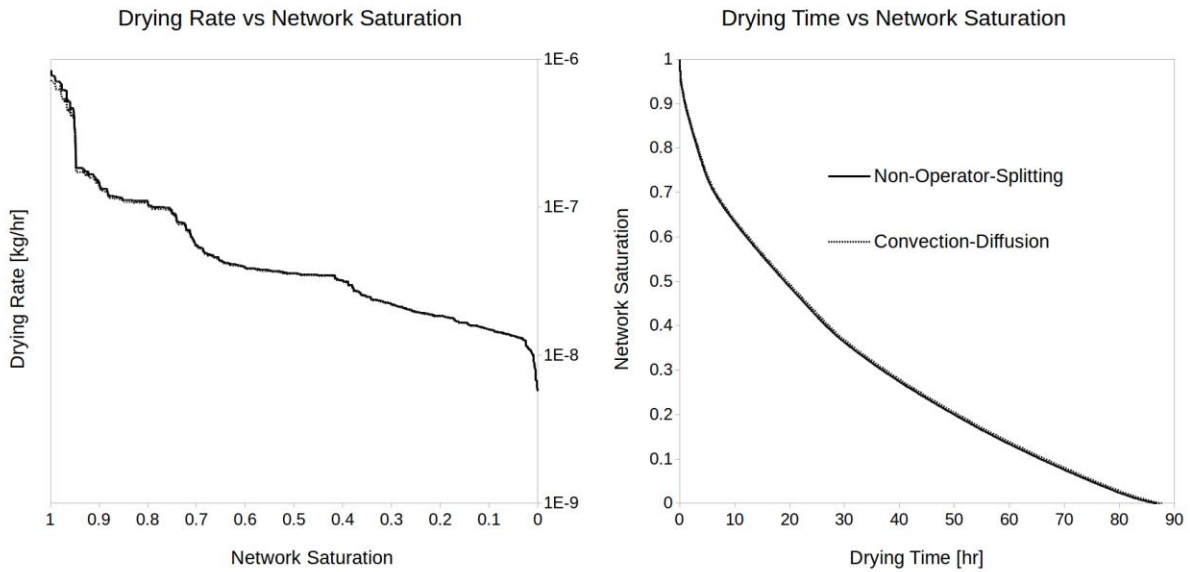


**Figure 23. Effect of using the operator-splitting scheme for  $Pe=1000$**

The non-operator-splitting method adopted here turns out to be better than operator-splitting method when solving equation (9) in both the external and internal domains. The reason may be that the physics of both domains are different: the external field has both convection and diffusion, while the pore-network has only diffusion. We will follow this recommendation in our future implementations of the proposed drying algorithm.

## 4.6 Influence of Peclet Number

In this numerical experiment, four cases are tested. All the other settings are the same except

for the Peclet Number: the dimensionless number is increased from 1 to 1000 by increasing the inlet velocity.

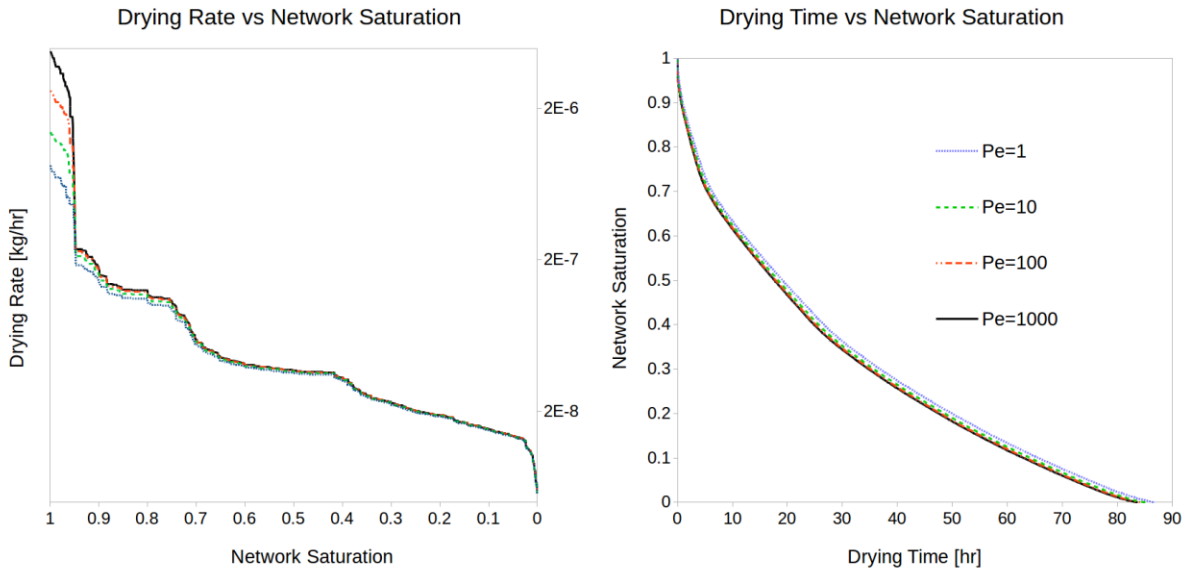


**Figure 24.** *Influence of Peclet number on the drying kinetics*

From the results as shown in Figure 24, we can see that total drying time is shortened slightly when the Peclet Number is higher. This is reasonable because increasing the Peclet number implies stronger advection and faster transport of moisture away from the wet porous medium. Another explanation is that the concentration boundary layer will be thinner (i.e., CBL thickness will be smaller); as a result, the concentration change from the wall to the upper limit of the concentration boundary layer will be sharper than in the lower  $Pe$  case. Hence the porous medium will dry up faster. Note that the mass-flux out of the porous medium, reflected in the drying rate, also follow this trend: larger the Peclet Number, larger the mass flux.

However, the difference in the total drying time is not so large—this is because the mass flux

difference only varies much during the early period of drying. When the drying front progresses deep into the pore-network, the resistance offered by the empty network for vapor transport dominates the overall drying and hence the influence of increasing  $Pe$  decays with time (which corresponds to the decrease in network saturation).

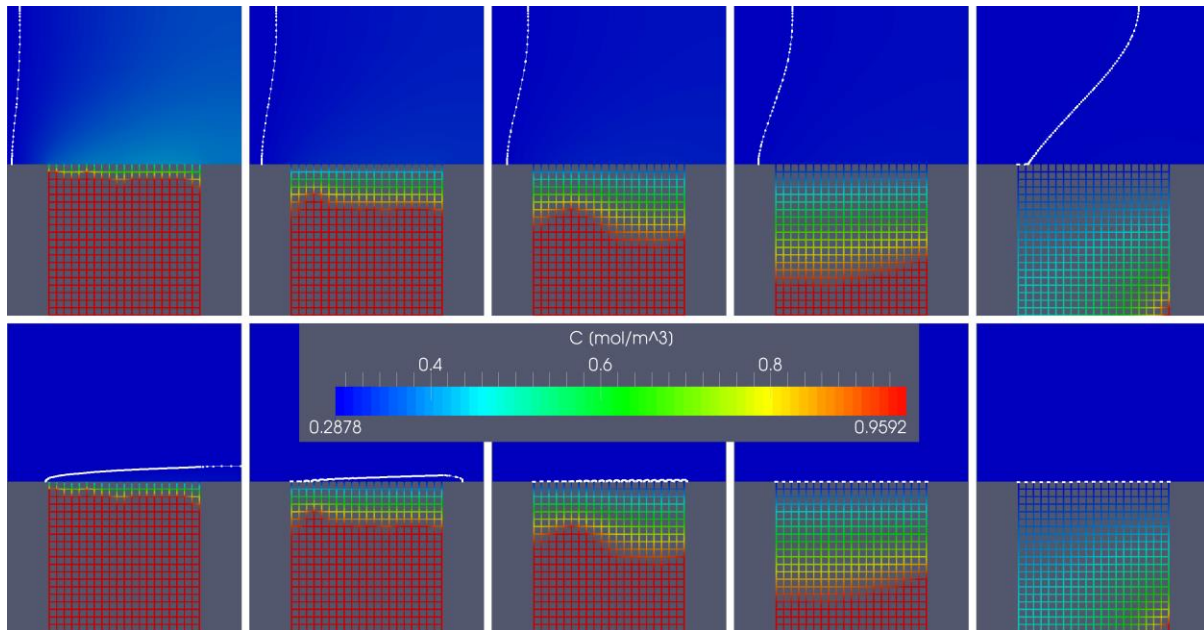


**Figure 25. Phase distribution of different time step (Notes: 1: top row:  $Pe = 1$ ; bottom row:  $Pe = 1000$ ; 2: from left to right, time step 100, 300, 500, 700, 820; 3: the white line in the outside flow field shows the position of the concentration boundary layer (CBL)).**

Now we compare the effect of the two Peclet numbers on saturation distribution inside the network as well as on the CBL. The phase distributions of these two cases are quite similar for different times, as shown in Figure 25, because the network microstructures for these two cases are the same. But the outside vapor concentration distributions are different because of the differences in their Peclet numbers: the larger Peclet number has a thinner CBL.

## 4.7 Influence of Pore-Network Structure

In this section, we keep all other settings constant, and only change the microstructure of the pore-network by changing the RSN and MVP values mentioned above, as shown in Table 3. The results are shown in Figure 26.

*Table 3. Influence of random-number-generator parameters on the pore-network structure (Nomenclature: the case P1DR5 implies RSN=1 and MVP=5)*

	Random Seed Number (RSN)	Maximum Variation Percentage (MVP) of the Throat Diameter
P1DR5	1	5
P2DR10	2	10
P1DR0	1	0 (Uniform Diameter)

It is clear that, of all our parametric studies done till now, the network microstructure influences the drying rate and drying time the most. A uniform network dries almost 25% faster than its non-uniform counterpart. Hence the pore-level microstructure is the most important parameter affecting any drying pore network.

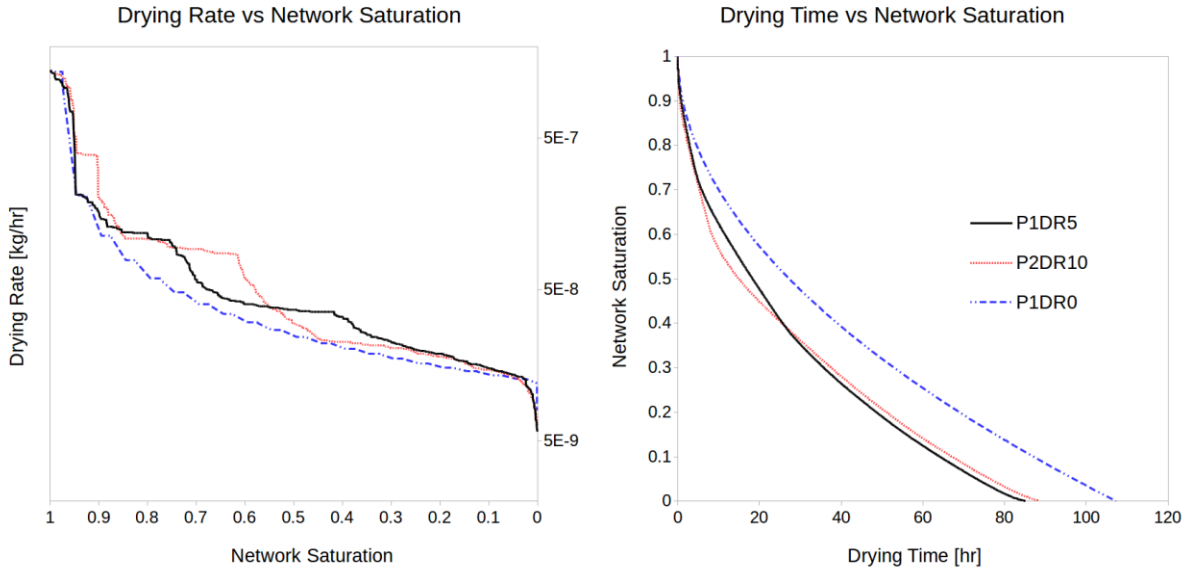


**Figure 26. Influence of pore-network structure on drying kinetics**

## 4.8 Conclusions

This chapter broadly studied the factors influencing the multi-scale problem of isothermal slow-drying simulation of a porous medium in laminar flow. And we can draw the following important conclusions:

1. Mesh refinement is important in the direction normal to the concentration boundary layer formed in the outer flow.
2. The influence of the space discretization schemes on the drying simulation is negligible.
3. Time-step refinement for the outside concentration boundary layer has no influence on the proposed simulation.
4. The outside air velocity influences the drying of a porous medium, especially at the initial

stage, but the overall impact is not as large as imagined, especially when the pore-network is deep.

5. The micro-structure of the pore-network, in terms of throat diameter distribution, influences the drying the most.



## 5 FORMULATION II: P-N MODEL FOR DRYING WITH FILM EFFECT

In the previous three chapters, we developed and examined the new fully-coupled, implicit algorithm for predicting drying in porous media placed in a laminar air flow. In this chapter, the algorithm will be developed further to include the crucial film effect without adding further complexity to the overall drying algorithm. The external flow field calculation is exactly the same as stated in chapter 2. The mechanisms of predicting vapor transport in the external field is also the same. The only difference is in modeling of the evaporation physics after adding the film effect.

### 5.1 Physics of Evaporation in Pore-Network

During drying, the network will be invaded by air, and the liquid phase will recede away from the open interface, leaving a liquid film climbing in the corners of the throats, as shown in Figure 27. How far the film extends into the dried region depends on many factors including the liquid properties, porous-media material properties, throat size, and cross-sectional shape of the throats (Yiotis & Boudouvis, 2003) (Prat, 2007). During the drying process, the pore network will have the *gas regions* (where the throats and pores are completely devoid of liquid and filled with mixture of air and water vapor), the *film regions* (similar to the gas region with the exception of liquid films being present at throat corners), and the *fully-saturated liquid regions* (where throats and pores are full of liquid).

In the gas region of the pore network, diffusion is still the unique mass transportation mechanism as stated in chapter 2.

In the liquid region of the pore network, the liquid flow still follows the I-P rule under most circumstances (Prat, 1993), even when film effect is considered.

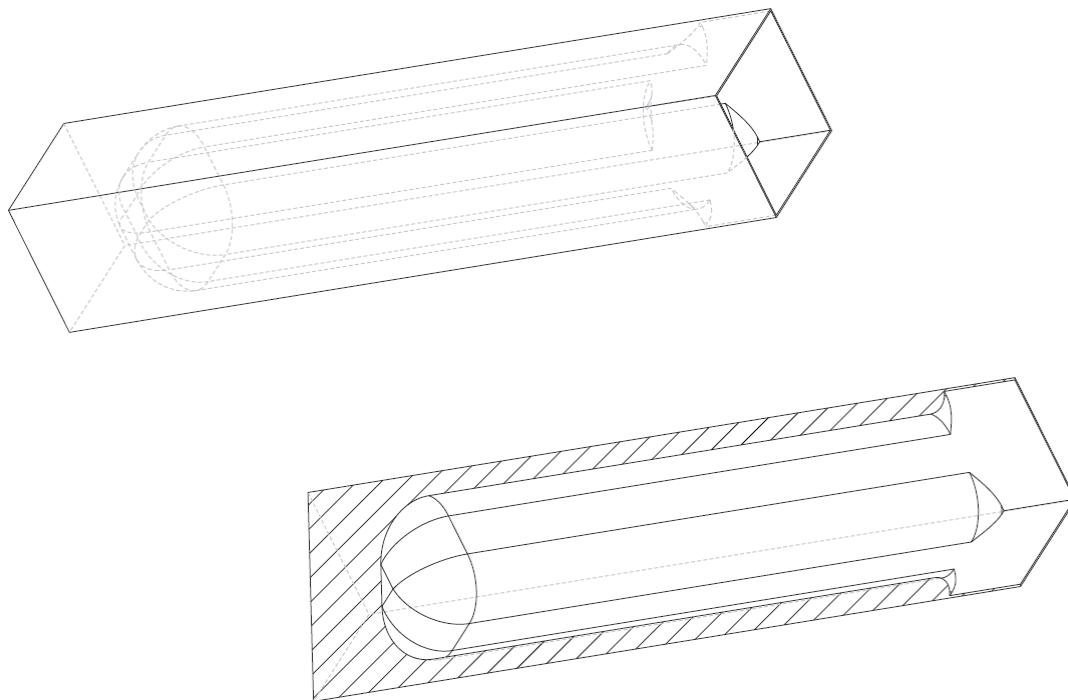


**Figure 27. A typical set of “fingers” created by the liquid film climbing at the corners of a square cross-section throat**

In the film region of the pore network, mass transfer is mainly through flow in liquid films because mass flux through diffusion in air is zero. (The vapor concentrations at the center of throats correspond to the saturated vapor pressure and hence remain unchanged along throat lengths due the tiny space where the film fingers exist (Prat, 2007)).

There are usually two kinds of films existing in throats: the large one existing at the corner of

throats, and the thin films existing between film ‘fingers’ (Figure 28). The mass transport through thin films is usually ignored because their thickness is on the order of a few nanometers.

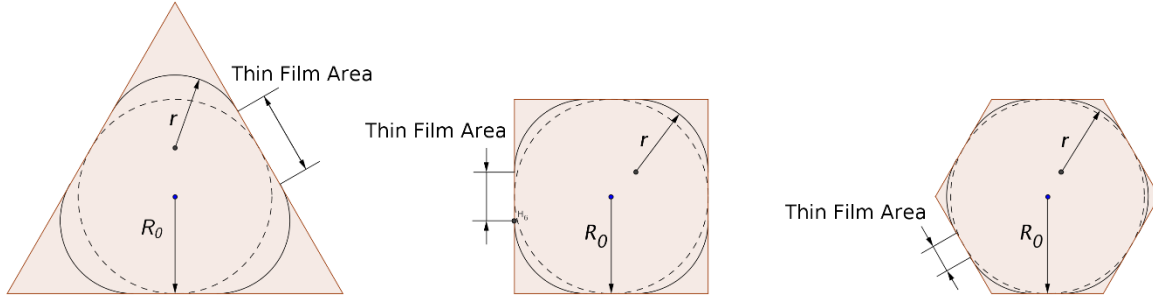


**Figure 28. Cross section of various throats showing thin films existing between the thicker films attached to the corners**

The liquid motion in the corner-film fingers follows the Poiseuille Law as

$$Q_F = -\frac{A_C r^2}{\beta \mu_l} \frac{dp_l}{d\delta} \quad (17)$$

where  $Q_F$  is the volume flux,  $A_C = r^2 \psi_4$  is the cross-section area of the corner when there is no round corner and  $\psi_4 = \left[ \frac{\cos \theta}{\sin \alpha} \cos(\alpha + \theta) - \frac{\pi}{2} + \alpha + \theta \right]$ , liquid pressure  $p_l = -\frac{2\gamma \cos \theta}{r}$ ,  $r$  is the curvature radius of the film as shown in Figure 28 and  $\mu_l$  is the liquid viscosity.  $\beta$  is the geometrical factor of the considered cross-section (Zhou, et al., 1997) and is described as

$$\beta = \frac{12 \sin^2 \alpha (1 - \psi_5)^2 (\psi_1 - \psi_5 \psi_2) (\psi_3 - (1 - \psi_5)(R_C/r))^2}{(1 - \sin \alpha)^2 \psi_5^2 (\psi_1 - \psi_5 \psi_2 - (1 - \psi_5)(R_C/r)^2)^3} \quad (18)$$

where  $\psi_1 = \cos^2(\alpha + \theta) + \cos(\alpha + \theta) \sin(\alpha + \theta) \tan \alpha$ ,  $\psi_2 = 1 - \theta/(\pi/2 - \alpha)$ ,  $\psi_3 = \cos(\alpha + \theta)/\cos \alpha$ ,  $\psi_5 = (\pi/2 - \alpha) \tan \alpha$ .  $\alpha$  is the half of the corner angle while  $\theta$  is the contact angle, as shown in Figure 29.

If the throat corner is rounded with radius  $R_C$ , then the film finger cross section area

$$A_F = A_C - R_C^2 \psi_4(0) \quad (19)$$

where  $\psi_4(0)$  is the value of  $\psi_4$  when  $\theta = 0$ .

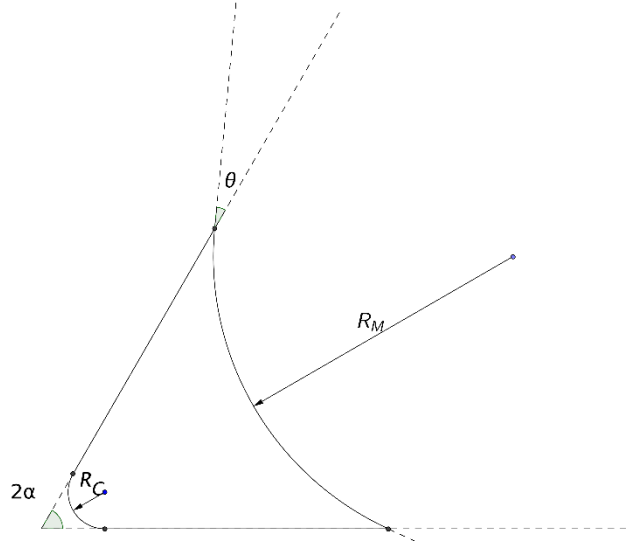


**Figure 29. Geometrical details of a typical corner film**

On combining equation (17) and (18), we get the volume flux going from a pore through a single film finger as

$$Q_F = \frac{\kappa \gamma r^2}{\mu_l} \frac{dr}{d\delta} \quad (20)$$

where  $\kappa = \psi_4/\beta$ .

By incorporating equation (20) with equation (7), we get a unified mass-balance equation which works for pores in both the film and gas regions:

$$\sum_j \dot{m} = \sum_j \dot{m}_F + \sum_j \dot{m}_G = \sum_j \frac{N\kappa \rho_l \gamma}{3 \mu_l} \frac{r_i^3 - r_j^3}{\delta_{ij}} + \sum_j MDA_{ij} \frac{C_i - C_j}{\delta_{ij}} \quad (21)$$

$$= 0$$

At the liquid-film interface (i.e., the interface of the liquid and film regions), the film curvature radius at the throat reaches its highest value  $R_M = \frac{R_0}{\chi}$  where  $R_0$  is the radius of the largest inscribed sphere in the throat (Figure 28) and  $\chi$  is a geometry factor that can be expressed (Prat, 2007) as

$$\chi = \cos\theta + \sqrt{\frac{(\theta_c - \theta + \sin\theta \cos\theta)}{\tan\theta_c}} \quad (22)$$

The liquid-film interface can be tracked using the I-P algorithm while ignoring the viscous effects in the bulk liquid region. And there exist situations in which the viscous effects can be neglected in the bulk liquid, but not in the film (Prat, 2007).

At the film-gas interface (i.e., at the interface of the film and gas regions), the film radius is zero and the gas mole concentration corresponds to that of the saturated vapor. To save the effort of explicitly tracking the film-gas interface, we introduce two constants for the network:  $\varphi_1 = \frac{N\kappa \rho_l \gamma}{3 \mu_l}$ , and  $\varphi_2 = MDA_{avg}$ . Here we need make a convenient but error-introducing assumption [which is also being used by other researchers (Yiotis, et al., 2004) (Prat, 2007)] which is assuming  $A_{ij}$  being equal to  $A_{avg}$  such that  $A_{avg}$  is calculated from the median value of throat radius for the whole network. Then the conservation of mass as applied at various pores leads to

$$\sum_j \dot{m} = \sum_j \frac{(\varphi_1 r_i^3 + \varphi_2 C_i) - (\varphi_1 r_j^3 + \varphi_2 C_j)}{\delta_{ij}} = \sum_j \frac{\phi_i - \phi_j}{\delta_{ij}} = 0 \quad (23)$$

Here  $\phi_i$  is a function of the film curvature radius,  $r_i$ , and the mole concentration,  $C_i$ . By solving for  $\phi$  in the pore network field, the mass transport can be calculated without considering the movement of the film-gas interfaces.

Only one boundary condition is needed to solve equation (23), which is at the interface between liquid and film regions. At this interface,

$$\phi_{Bulk} = \varphi_1 R_{M,avg}^3 + \varphi_2 C_{sat} \quad (24)$$

Here  $R_{M,avg} = (R_{M,max} + R_{M,min})/2$  is the pore-network average of the maximum film-curvature radius.

## 5.2 Dimensionless Analysis

To do the dimensionless analysis on equation (23), we can get two capillary numbers, one for bulk liquid ( $Ca$ ) and the other for film  $Ca_F$ , defined as

$$\begin{aligned} Ca &= \frac{\mu_l^* D^*}{\gamma^* \delta^*} \\ Ca_F &= \frac{3\mu_l^* D^*}{N\kappa\gamma^* \delta^*} \end{aligned} \quad (25)$$

where  $\mu_l^*$ ,  $D^*$ ,  $\gamma^*$ , and  $\delta^*$  are the reference values of the viscosity, mass diffusivity, surface tension and length, respectively. If we choose  $\delta^*$  to be the diameter of throats,  $Ca$  can reflect

the ratio of viscous to capillary forces in the bulk liquid. While inside the film, a geometrical  $3/N\kappa$  is added to reflect the condition in the film.  $\kappa$  is a very small number related to the cross-section shape of the throat, and is  $2.086 \times 10^{-2}$  for triangle,  $1.893 \times 10^{-3}$  for square, and  $8.817 \times 10^{-5}$  for hexagon. These values usually make  $Ca_F$  hundreds of times larger than  $Ca$  which implies that the viscous effect in film flow is much larger than in the bulk liquid. So there exist situations in which the viscous effects can be neglected in the bulk liquid but not in the film (Prat, 2007).

### **5.3 Fully-Coupled Implicit Solution for Vapor Concentration in External Flow-Field and Pore Network**

Calculating mass transport in the external field needs solving for concentration  $C$  in the external field, while calculating the same inside the pore network requires solving for  $\phi$  in the network. Previous researchers solved the outside and inside concentration fields using the time-marching explicit method (Yiotis & Boudouvis, 2003) (Prat, 2007), which is sensitive to the selection of time step. However, this is a multi-scale problem only temporarily. The time needed for emptying each throat in the pore network is usually much higher than the time needed for significant changes to happen in the outside flow field.

This effort seeks a novel way to implicitly solve both the fields simultaneously. The first effort is in finding the relationship between  $\phi$  and  $C$ . When the film radius is zero,  $\phi$  increases

with  $C$ . But when the film radius is non-zero,  $C$  stays at its saturated value while  $\phi$  increases with the film radius. This trend is depicted as a piece-wise curve in Figure 30.

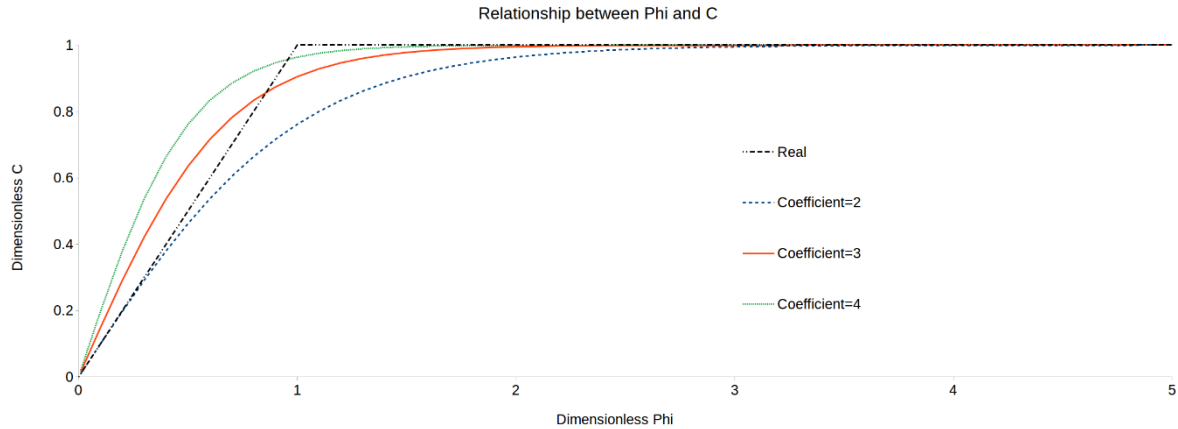


**Figure 30. Relationship between dimensionless  $\phi$  and  $C$ : the real relationship, and the 3 approximated relationship by setting different coefficient  $c = 2, 3, 4$  in Eq. (26)**

To avoid using small time-steps to catch the sharp break point of the piece-wise curve shown in Figure 30, some approximation curves are proposed using the logistic function:

$$C = \frac{2}{1 + e^{-\frac{c\phi}{\varphi_2}}} - 1 \quad (26)$$

Here a coefficient  $c$  is being used to control the shape of the curve. Figure 30 depict changes in the approximation curve when  $c$  is set equal to 2, 3 and 4. With this relationship, the pore network field and the outside field can be solved implicitly in a fully coupled manner by solving Eq. (6), (23), and (26) together.

The connection between the flow-field cells and the pore-network pores is the same as chapter 2, as shown in Figure 5. And their formulations are also similar to the one described in our



previous work (Xu & Pillai, Under Review), the only difference is that when the pore-network pores are considered, the  $\phi$  value is calculated instead of the vapor concentration  $C$  (Figure 31).

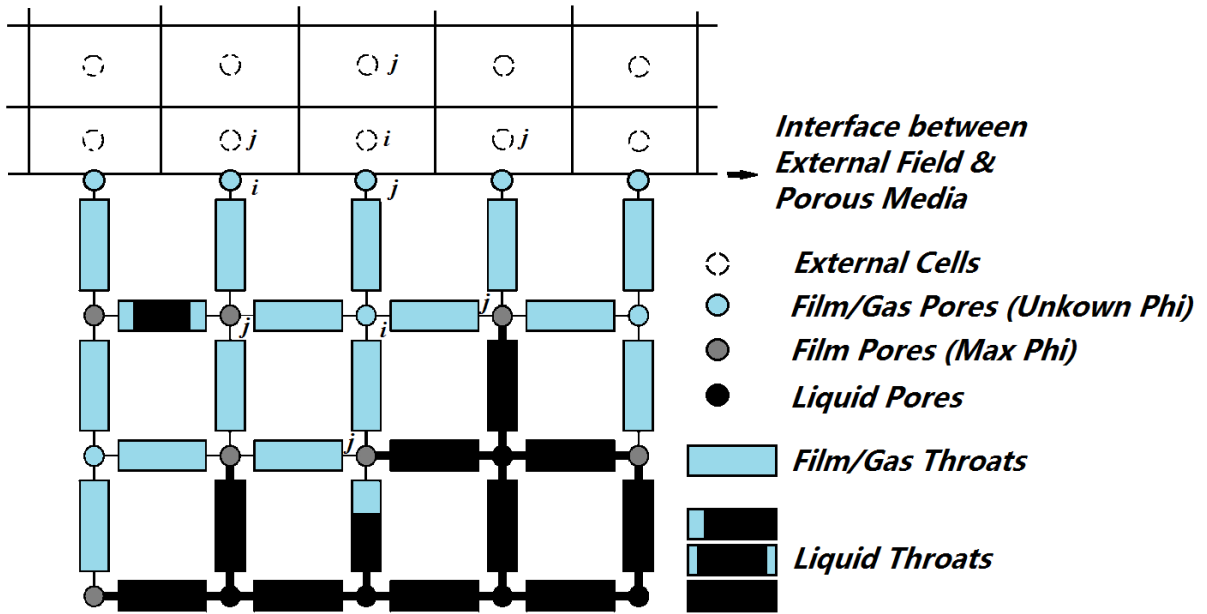
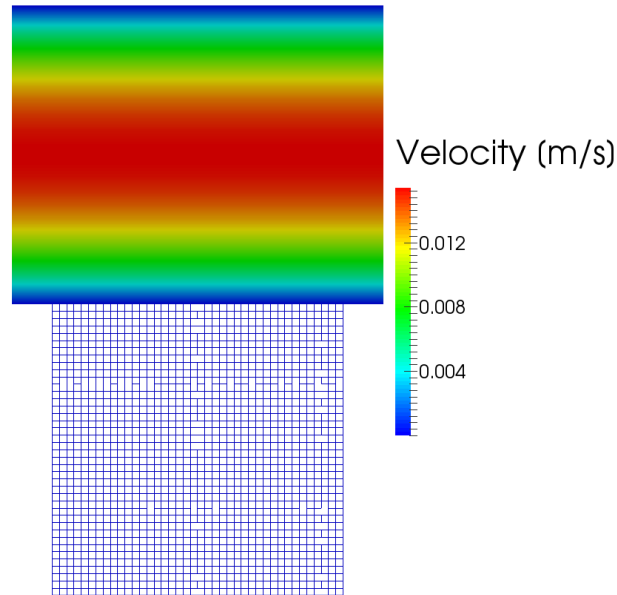


Figure 31. Coupling of the outside-flow node cells and the P-N pores - with film effect

## 6 EXAMINATION OF THE PROPOSED NUMERICAL METHOD

### 6.1 Testing the Approximation for the Relationship between Concentration, $C$ , and $\phi$

Before studying the other cases, the above-mentioned approximation for the relationship between  $C$  and  $\phi$  is tested with the drying of a  $40 \times 40$  pore network which is placed adjacent to a fully developed tunnel flow. The network consists of throats with square cross-sections: the throat length is  $500\mu m$  and the randomly-distributed hydraulic diameter range is  $5\mu m \pm 2.5\%$ . As shown in Figure 32, the slit width is  $2cm$  with the external flow field  $Pe = 500$ .



*Figure 32. A  $40 \times 40$  pore network put by side of, and open to, a slit flow during drying*

When studying drying problems, the most important results are the drying rate and drying

time, hence we compared these results when using different value for coefficient  $c$ . Figure 33 shows that the drying rate-vs-network saturation and the network saturation-vs-drying time curves almost overlapped for these cases. (The network saturation is the ratio between the remaining liquid mass and the original liquid mass. Hence it is a measure of the amount of moisture left in a P-N or a porous solid.)

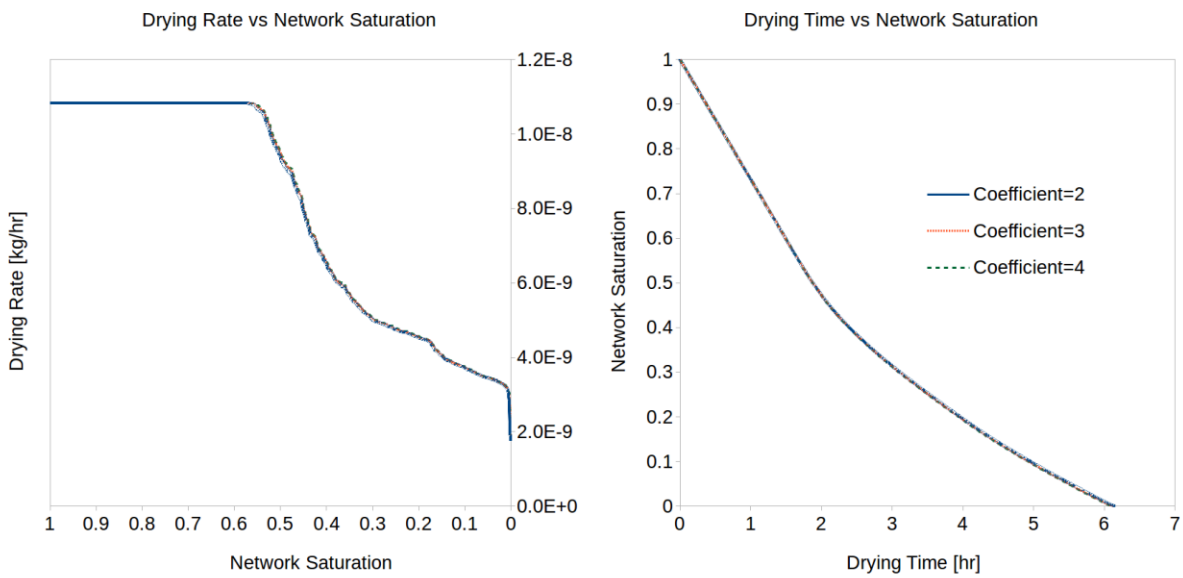


**Figure 33. A comparison of the evolution of drying rate and drying time for different approximations for the parameter  $C$**

As shown in Figure 30, the approximation curves are quite close to the real piece-wise linear curve. If all the three approximation curves generate the same results, it is not hard to conclude that the real piece-wise linear curve will also generate similar results. *For the rest of this thesis, coefficient  $c = 3$  is used.*

## 6.2 Modified Drying Algorithms

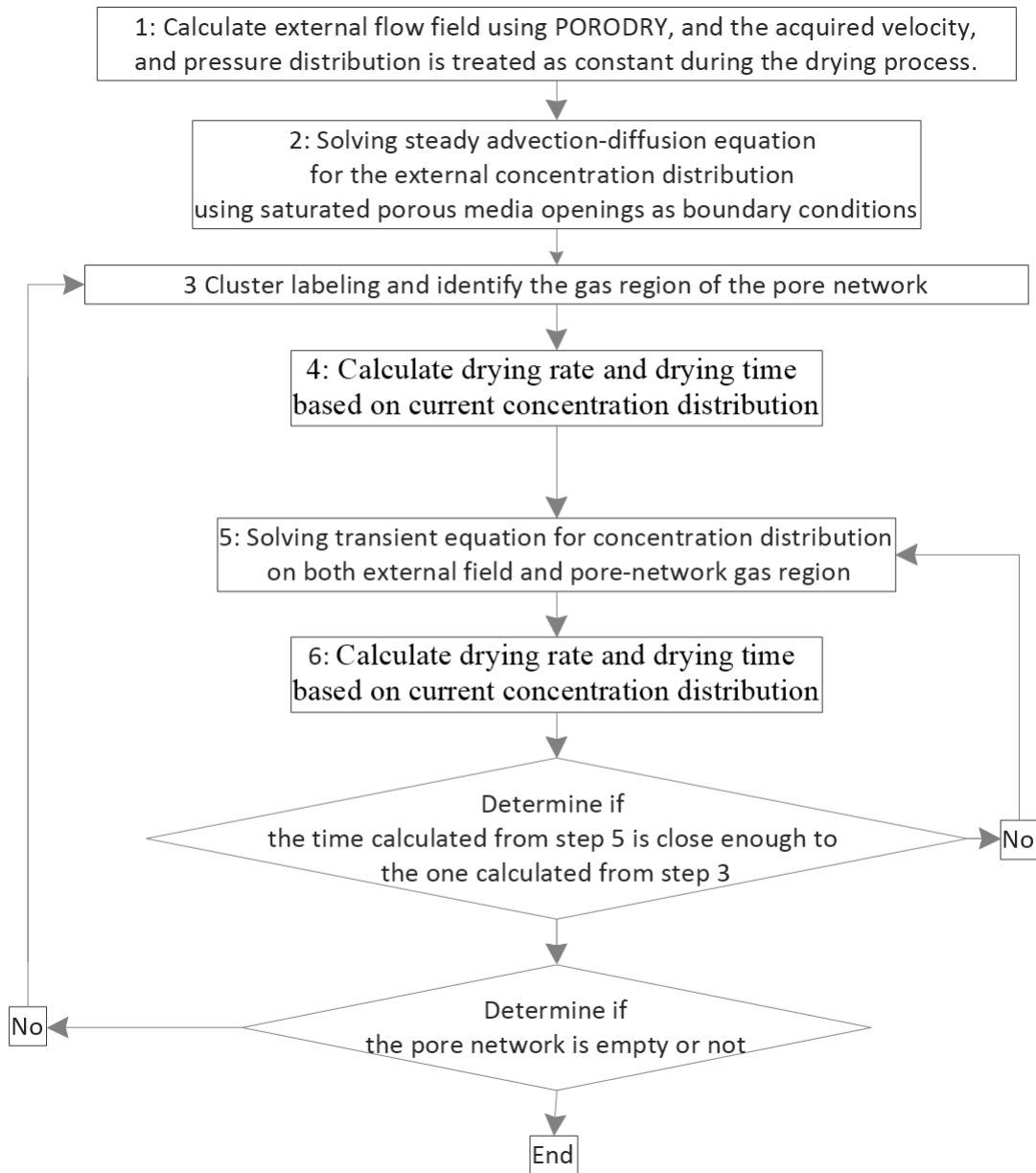


**Figure 34. Modified drying algorithm**

As stated in chapter 5, the drying algorithm after including the film effect can be exactly the same as the one used in chapter 2. The only difference is to calculate  $\phi$  instead of  $C$  when solving

the transient vapor-concentration equation. All calculations done with this algorithm are found to be satisfactory.

Here we present another algorithm, which is modified from the original one given earlier. On comparing the original algorithm (Figure 6) with the modified one given here (Figure 34), we note that only one non-iterative step is added: the second step. This step is used to initialize the external field with the liquid-saturated openings of the pore-network at saturated vapor-pressure conditions.

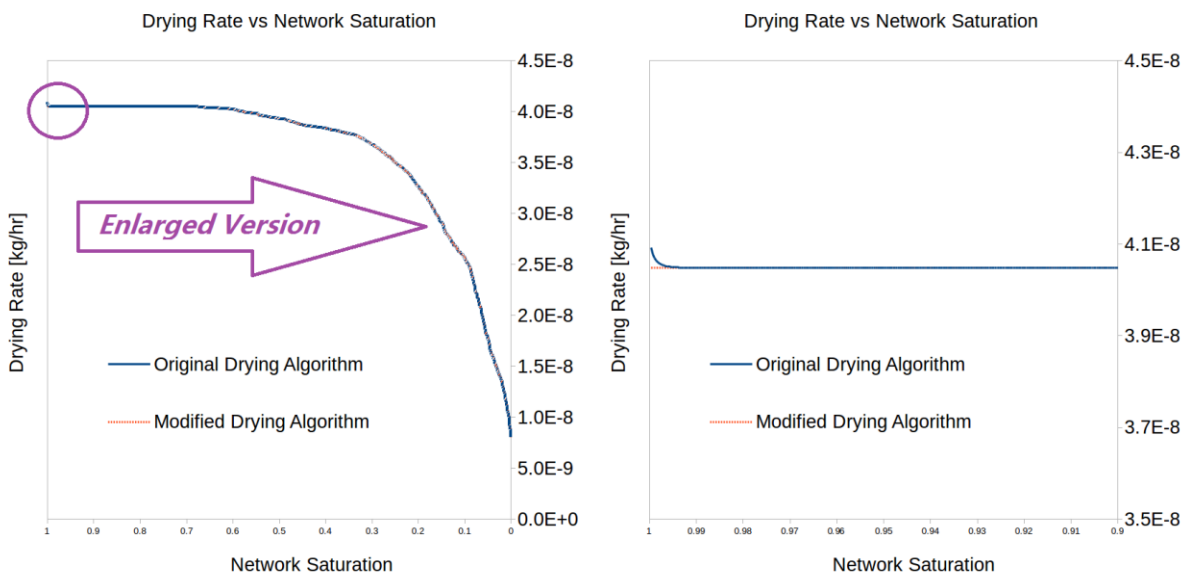


**Figure 35. A comparison of the predicted drying rates obtained using the original drying algorithm and the modified algorithm**

The comparison is shown in Figure 35 where the drying rates predicted by these two algorithm are indistinguishable from each other. Only at the beginning of the drying process did the drying-rate plot change from a decreasing curve to a straight line. These two algorithms actually represent two different physical conditions. The original one involves inserting the porous

medium in the external flow field with a uniform (initial) vapor concentration. While the modified one is placing the pore network in the external flow field with the fully-developed (initial) vapor concentration distribution.

It is clear that both algorithms provide virtual identical predictions. There are no particular drawbacks with the either algorithms, but we just *used the modified version to calculate all the rest of the simulations.*

### 6.3 Time Step Selection

This study is similar to the study conducted in section 4.3. After the film effect is added, we ask if the time step refinement will have any effect. We note that the time needed for the network to dry out one throat (which is on the order of the time step needed for the internal drying simulation) is *still* much longer than the time needed for the flow to sweep across the whole length of the porous medium. The question is whether we need to use finer time-steps for the external evaporation simulation compared to those for the internal drying simulation?

As shown in Figure 36, the drying rate and drying time calculated from all types of sub time-steps overlapped with each other; only the drying rate calculated from “SubStep=1” is slightly different from the other results at the later stage of the drying process. This maybe because, at the later stage, the time-scale difference between the external-field and pore-network computations is larger because it takes longer to dry out one throat when the drying rate decreases

after the drying front has receded into the porous medium.

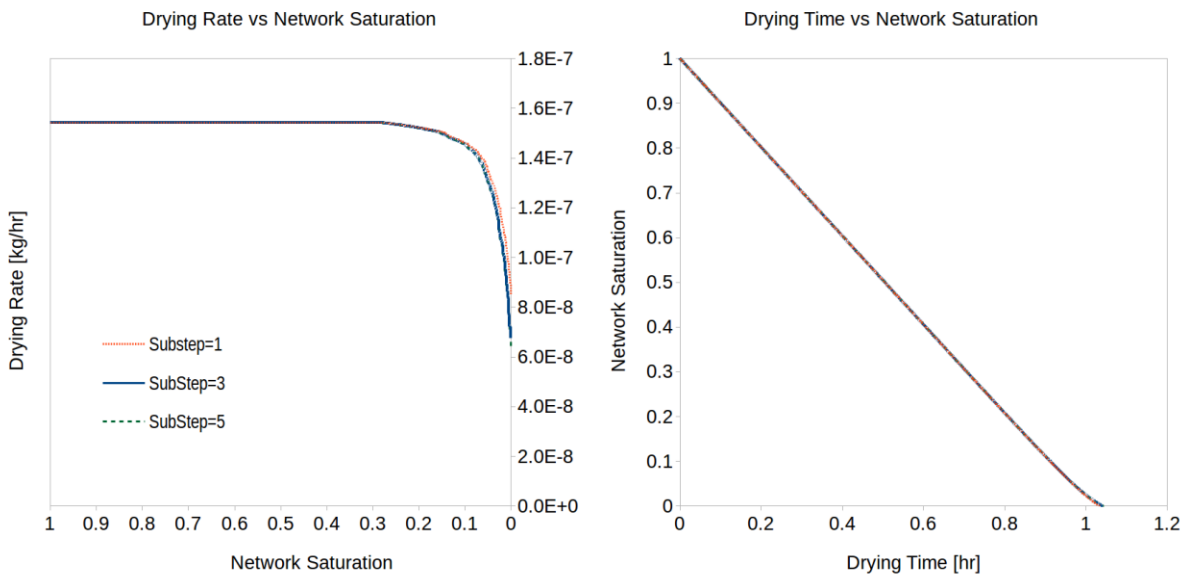


**Figure 36. Effect of different sub time-steps on the drying characteristics of pore network (For example, “SubStep=5” means that the drying time step is divided into 5 sub steps)**

However, when the film effect is not considered, this deviation did not occur. So it is possible that the newly-proposed logistic function also contributed some errors. In any case, *for the remaining simulations, the sub time step is set equal to 3.*

## 6.4 Comparisons between Spatial Discretization Schemes

This study compared the Hybrid scheme and Hayase QUICK scheme on a square network with hydraulic diameters of the throats falling in the range  $10\mu\text{m} \pm 5\%$ . The velocity contours are shown in Figure 37. It is apparent that there are only very slight differences between them. The maximum velocity in the field is 0.0134m/s for the Hybrid scheme and 0.0135m/s for the QUICK scheme. The wake created after the square using the Hybrid scheme is slightly smaller and

shorter than the one created using the QUICK scheme. However, one can hardly notice these differences in the flow field.

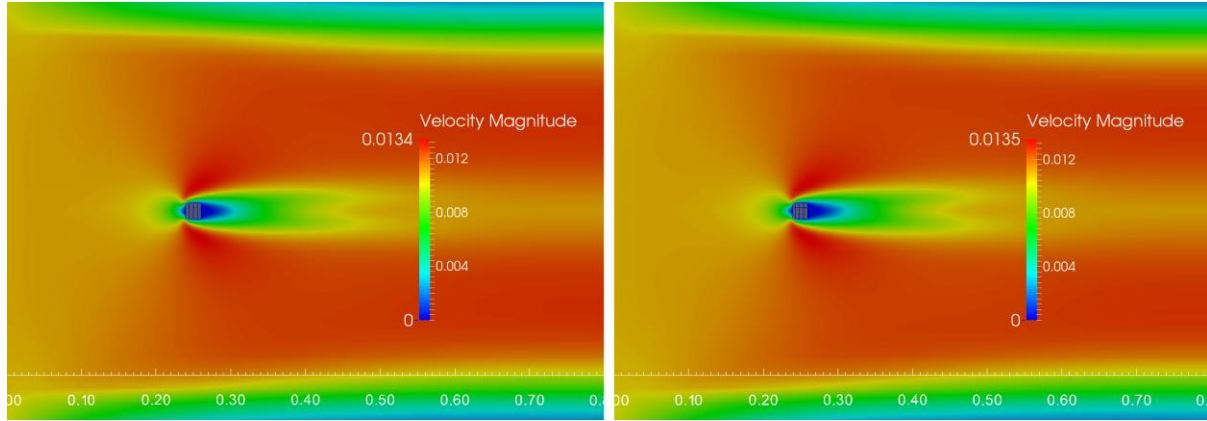


**Figure 37. Velocity field comparison (left: hybrid scheme; right: QUICK scheme)**

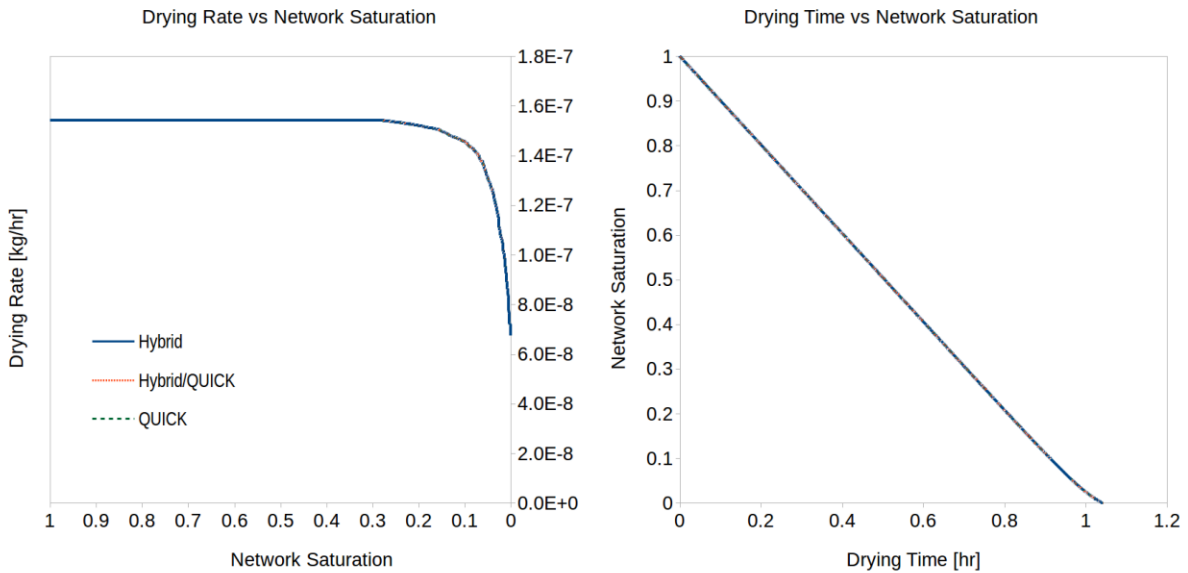


**Figure 38. A comparison of the drying characteristics as predicted by three different spatial discretization schemes**

As shown in Figure 38, the legend entry “Hybrid” means using the Hybrid scheme when calculating the outer flow-field and vapor concentration distribution; the legend “QUICK” means using the Hayase QUICK scheme for the same; while the legend “Hybrid/QUICK” means using



the Hybrid scheme when calculating flow field and using the Hayase QUICK scheme when calculating the vapor concentration distribution. Since the velocity contours overlapped for the schemes, it is not surprising that the drying rate and drying time plots overlapped with each other too. Hence it was concluded that there is no need to explore this issue any further, and *for the remaining cases of this article, all calculations are performed using Hybrid scheme.*

## **7 IDENTIFYING FACTORS INFLUENCING THE FILM EFFECT**

According to Eq. (17) to (22), the extension of film is influenced by its throat diameter, throat cross section shape. However, this study will find out more factors which may influence the film extension except the intrinsic characteristics of the network, such as the external conditions.

To simplify the situations and make the influential factors stand out, this study is tested in a  $40 \times 40$  pore network which is put by side a fully developed slit flow as shown in Figure 32. The networks consist of throats with  $500\mu m$  length, whose hydraulic diameter and cross section shape vary. The external velocity and humidity also vary.

### **7.1 Influence of Throat (Hydraulic) Diameter**

This study compared the drying of network under conditions of external  $Pe = 10$ , and external humidity 50%. The average diameter of the network changes from  $1\mu m$  to  $10\mu m$ . The throat diameter varies in a range of  $\pm 5\%$  around the average diameter.

From Figure 39, we can see that the network with larger throat diameter has larger drying rate and longer constant drying rate period. This is because the exposure area to the outside of a larger-diameter network is larger, and the film of a larger-diameter throat extends farther than a smaller throat. As the equations in chapter 5 implied, the throats with larger diameter also have larger  $R_M$ , which will help to support longer film fingers along the corners. So the constant drying

rate period is longer. Apart from this, the larger throats have larger exposure area, which makes the drying rate larger. For these two reasons, even as the networks with larger throats have more liquid, they still dry out more quickly.

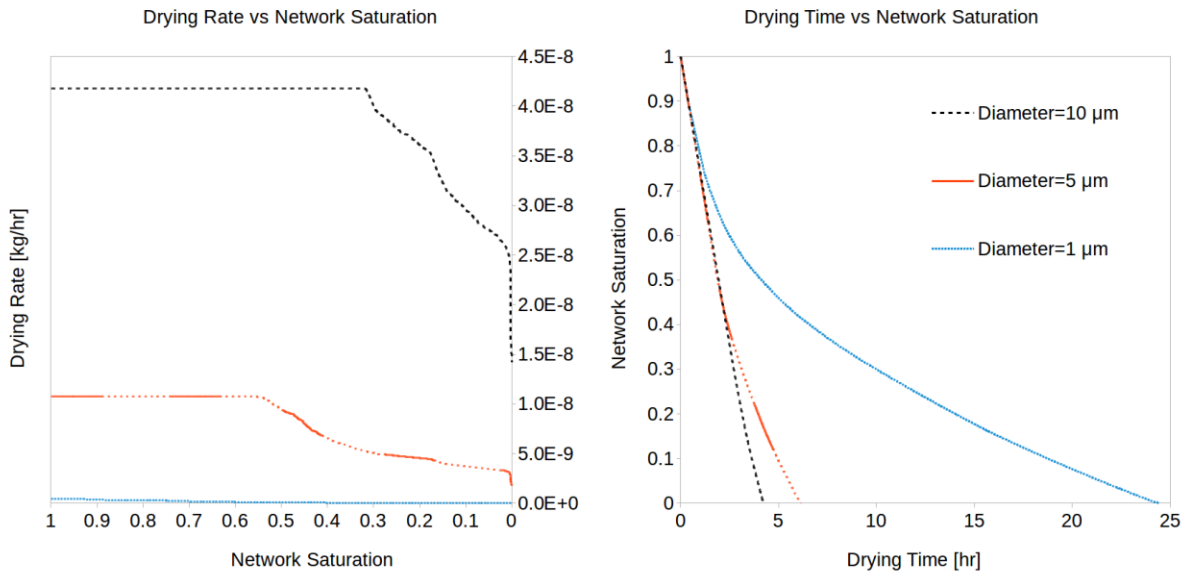


**Figure 39. Influence of throat diameter on film effect**

Figure 40 shows the contour of case  $D = 5\mu m$  respectively at 600, 1600, and 3200 steps. Note that the film extension of 1600 time steps is much shorter than the film extension of 3200 time steps. And the iso-film-radius bars also show us that: the film changing gradient of 1600-step is more abruptly than that of 3200-step. We will explain this phenomenon further in following sections.

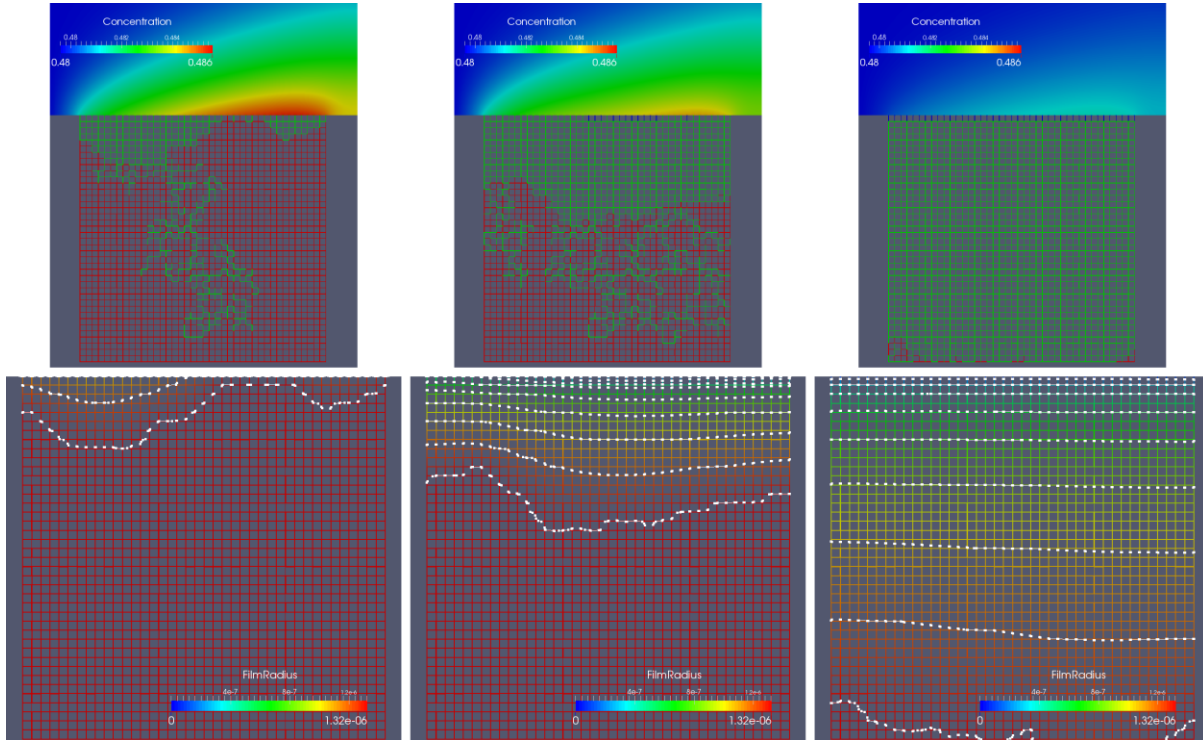


**Figure 40. Phase distribution and film radius distribution of case  $D = 5\mu\text{m}$  (upper row: the phase distribution and outside concentration; lower row: the corresponding film radius)**

## 7.2 Influence of Throat Cross Section Shape

This study compared the drying rate when the throat cross section changes among Circle, Hexahedral, Square, and Triangle. The throat diameter of this study is fixed at  $10\mu\text{m} \pm 5\%$ . The external conditions are  $Pe = 10$ , and humidity is equal to 50%.

As shown in Figure 41, the triangle network has largest initial drying rate because it has largest exposure area when the average hydraulic diameter is the same. Triangle network also has longest constant-drying-rate period, which can be explained by Eq. (18). The film extension of triangle throat is so long that the constant drying rate period extend all the way to the end.

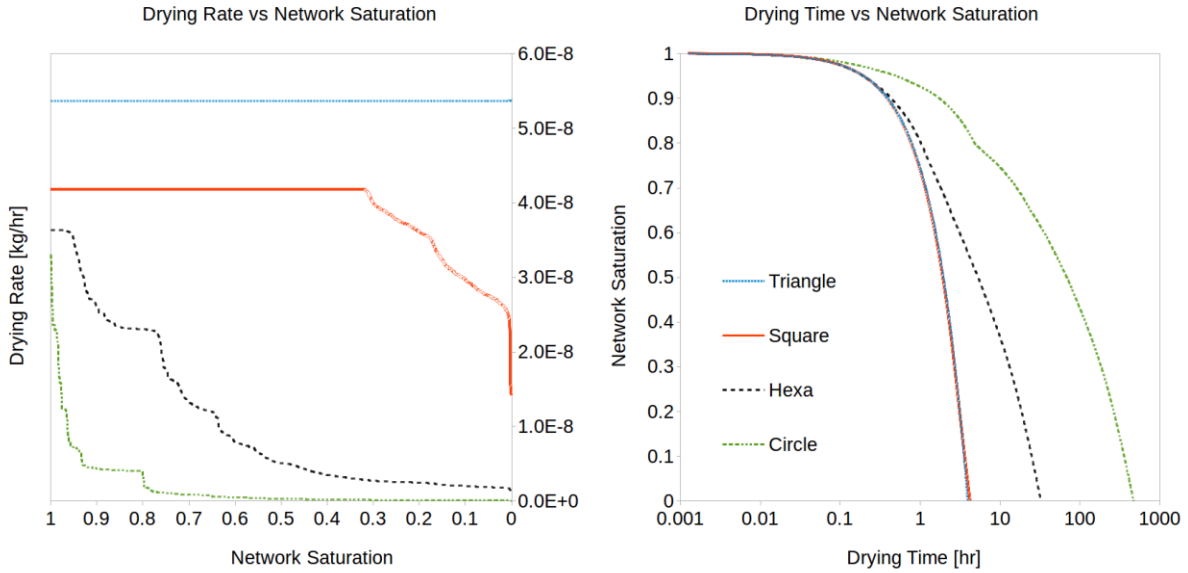


**Figure 41. Influence of throat cross section shape**

Circle throat network has no film effect, because it has no corners to hold the film fingers. Hexagon network is already very close to circle network, so its constant-drying-rate period only holds for a short period.

### 7.3 Influence of External Conditions

In this study, we used two sets of simulations to examine the influence of external conditions. In the first set, a square cross-section network with hydraulic diameter falling in the range  $5\mu\text{m} \pm 5\%$  is used. The outside Peclet number changes from 1 to 1000, and far field humidity changes from 30% to 70%.

The results of the first set are shown in Figure 42, We note that both the Peclet number and humidity influences the pore-network drying controlled by the film effect. Lower humidity makes

the drying rate significantly higher while the constant-drying-rate period much shorter. However, the Peclet number seems have only a slight influence on the drying process, which is rather difficult to believe.

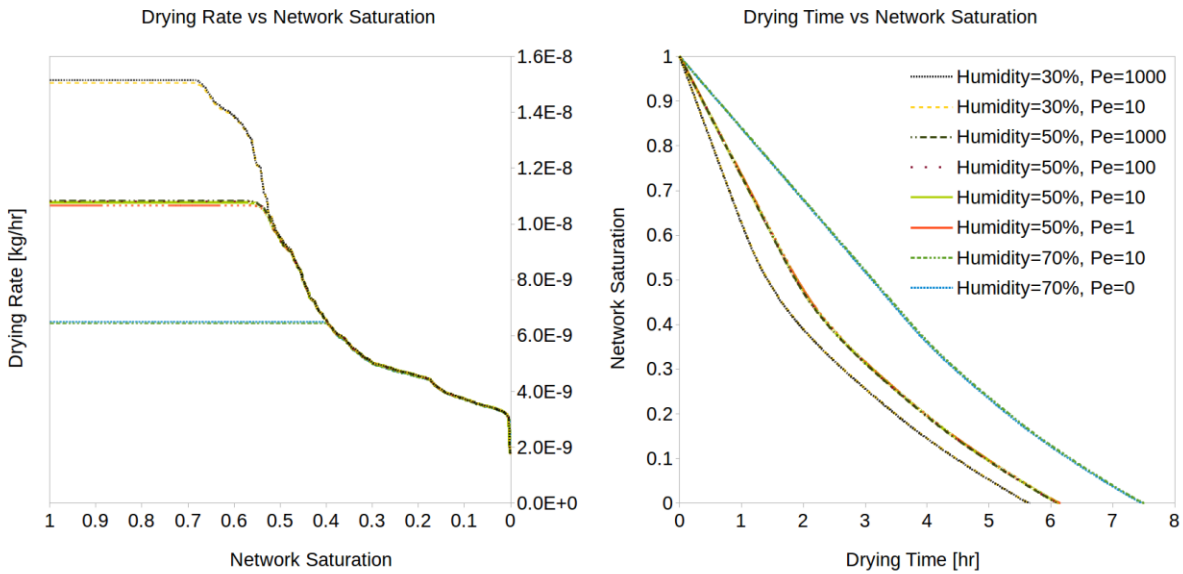


**Figure 42. Influence of external conditions on the film effect for pore diameter =  $5\mu\text{m} \pm 5\%$**

Hence, we did a second set of simulations, and this time a square network with hydraulic diameter equal to  $10\mu\text{m} \pm 5\%$  is used. The outside conditions change in the same way as they did in the first set.

The results of the second set are shown in Figure 43. The influence of Peclet number has increased a bit compared with the first set. Higher Peclet number makes the drying rate higher while constant-drying-rate period shorter too.

This is because Lower humidity and higher Peclet number all bring higher drying flux. When the drying flux is higher, a steeper changing film radius is required to transport enough liquid to

support that film extension. When the bulk liquid retreat into the inner part of the network, it will be harder for the big-flux condition to support that film, so the constant-drying-rate period is shorter.

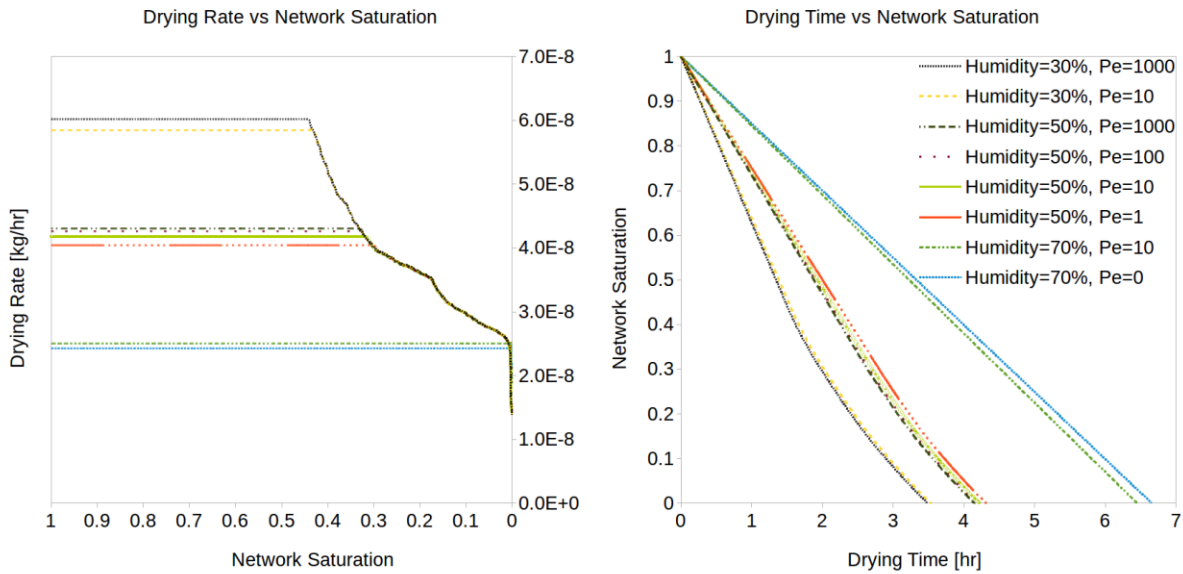


**Figure 43. Influence of external conditions on the film effect for pore diameter =  $10\mu\text{m} \pm 5\%$**

These phenomena coincide with the results shown in Figure 40. At 1600 step, the film tips are closer to the outside, which means higher drying flux, so the film extension is shorter and film radius changing gradient is steeper. At 3200 step, the film tips retreat into inner part of the network, so the film tips are farther away from the outside, which means lower drying flux, thus the film extension can be longer and film radius changing gradient is gentler.

To understand why the Peclet number has more influence on a network with bigger throats, one should refer to Figure 15. Note that the thickness of the outside finite volume is fixed. The network with smaller throats contains less liquid mass and has smaller exposure area. The changes

in the external vapor concentration under this condition are already very small, no matter how large the wind speed is. Only when there is enough vapor in the external flow field, can a larger wind speed bring a significant difference in the drying rate. However, a further 3D study is needed to corroborate this further.

## **7.4 Summary & Conclusions**

By conducting a parametric study on the drying of a square network placed next to a slit flow, it is discovered that (a) higher hydraulic diameter of the throats leads to higher drying rates and longer constant drying-rate periods; (b) the drying time increases and the drying rate decreases as the throat cross section changes from a triangle to a square to a hexagon to a circle, which can be correlated to the weakening of the film effect; (c) increasing the external flow velocity (that leads to changing the Peclet number from 1 to 1000) has little effect on the drying rates and times; (d) increasing the external air humidity from 30% to 70 % leads to a large decrease in the drying rates and consequent increase in the overall drying times.



## 8 STUDIES IN DRYING OF THIN POROUS MEDIA

Drying of thin porous media has been the subject of many research efforts and is still an active topic (Sander, 2007). Science pertaining to it is applicable to numerous industrial areas, such as paper producing, food processing, and coating (Jayas, et al., 1991) (Prabhanjan, et al., 1995).

Here we study drying in our pore network positioned at the center of a flow field. By changing the parameters such as the environmental conditions, the aspect ratio of the pore network, and the openings of the sides of the pore network to the flow field, the effects of interactions between the pore network and outside flow field on the former's drying characteristics are studied.

The basic form of the pore network considered here is a regular  $40 \times 40$  grid; the throat cross section is square with hydraulic diameter randomly falling in the range  $5\mu m \pm 5\%$ ; the throat length is set at  $500\mu m$ . The liquid saturating the network is water. The transformed thin version of this network, representing different thin porous media, with grid sizes of  $80 \times 20$  and  $160 \times 10$  representing two different aspect ratios will also be studied.

### 8.1 Square Pore Network Drying in a Flow Field

Square pore network has equal faces on each side that are normally kept closed (i.e., allowing no evaporation), so studying the drying rate and drying time by opening its different sides to the flow field is of special interest. The position of pore network in the flow field is shown in Figure 44 which presents a velocity distribution corresponding to  $Pe = 10$ . The humidity of the flowing air

is set at 50%. Note that the flow pattern shown using streamlines remains unchanged during the following cases involving different sides of the square kept open for drying.

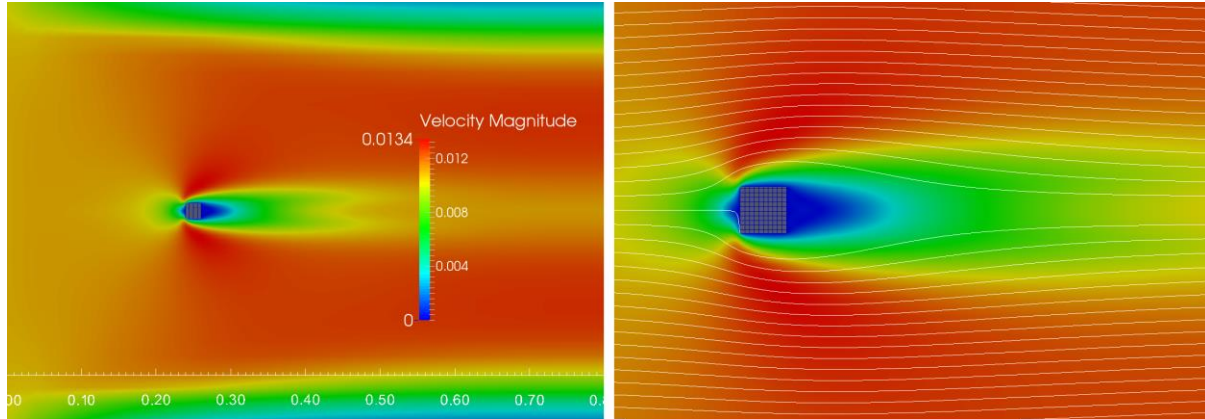


**Figure 44.** Velocity field around a square-shaped pore network at  $Pe = 10$  (left: velocity contour; right: velocity contour and stream lines)

### 8.1.1 Group 1 Simulations: One Side Open

In our first set of simulations, we seal three sides of the square-shaped network and open only one side. The N and S sides are symmetrical; so only E, N, and W side openings are studied. The E side is facing the wake, the W side is facing the incoming flow stream, and the N side is facing the top.

From Figure 45, we can see the mutual dependence of the drying rate, network saturation and drying time for different openings. Surprisingly, the total drying times for the three cases are almost identical. However, the drying rates for the three cases are different: The W case has a higher drying rate for a longer duration, but it drops below those for the N and E cases with time. It would be interesting to link the drying rates to the concentration boundary layer (CBL) thicknesses;

however, in order to check the length of this presentation, we will restrict that discussion to the subsequent cases. In fact, the study of CBL in the following cases will provide a natural explanation for the drying rates seen here.

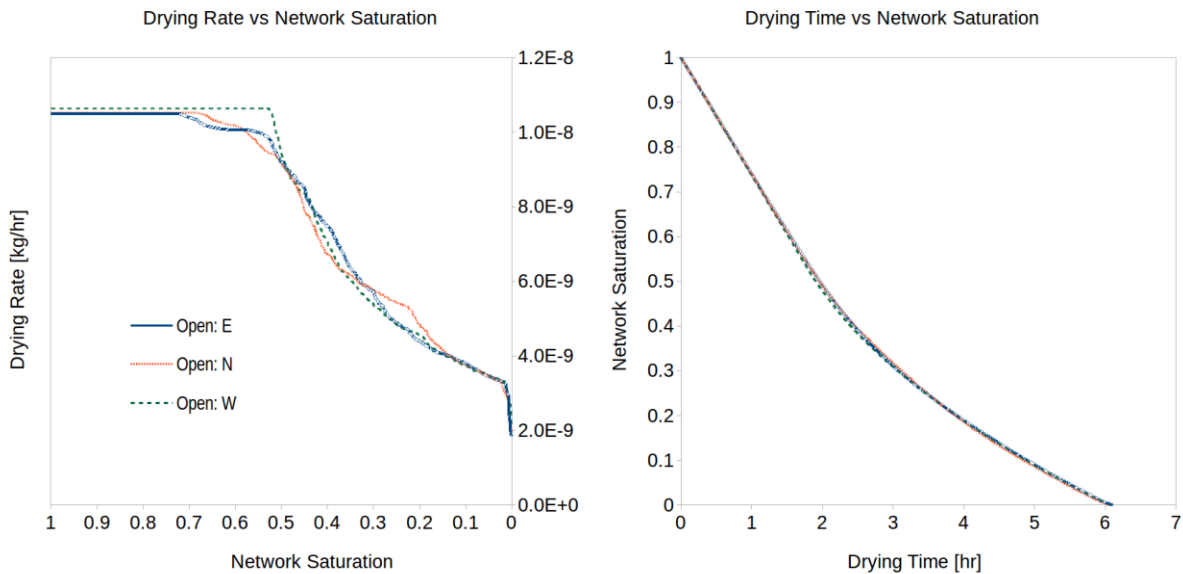


**Figure 45. Study of drying of the square-shaped pore network when its one side is kept open,  $Pe = 10$ , air humidity = 50%**

Note that the CBL is defined as a curve where the difference between the liquid-surface saturated vapor concentration and the local vapor concentration is 99% of the difference between the liquid-surface saturated vapor concentration and the environment vapor concentration.

### 8.1.2 Group 2 Simulations: Multiple Sides Open

In this group of study, three cases are tested: open N+S sides, open E+W sides, open all sides.

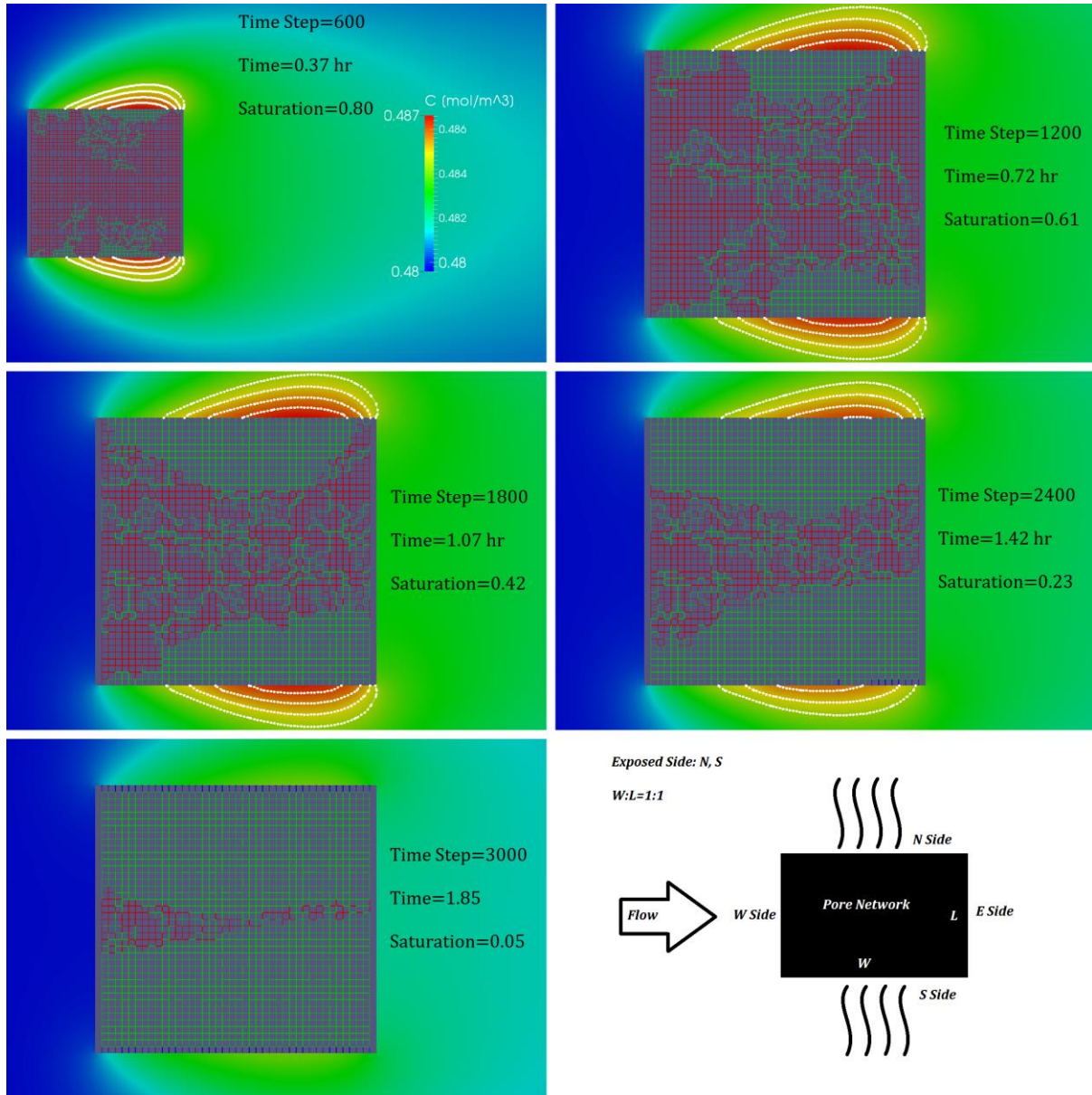


**Figure 46. Changes in the liquid phase distribution (within the network) and CBL with time: open N+S sides (the outermost of the iso-concentration lines, the white lines, marks the location of the CBL boundaries)**

Figure 46 shows the phase distribution inside the network and the outside CBL. In the picture, the red pores are fully saturated with liquid, and the green ones are those filled with corner films. One single large liquid cluster breaks up into smaller clusters as the drying front makes inroads. The overall liquid content of the network, given by the parameter network saturation and

proportional to the area under clusters, decreases with time. As one can see, the film covers the empty network almost all the way till the final steps of the drying process. As a result, the pores opening into the outer flow show the saturated concentration (i.e., vapor concentration corresponding to the saturated vapor pressure). Consequently, the CBL stays virtually unchanged for a long time. And this period is the constant drying-rate period, as shown by the long flat line in the beginning of Figure 45, left. Although the boundary of the CBL is distant from the opening sides of the pore network, the concentration gradient between throat openings and the boundary is very small—large concentration changes happen just near the throat. (Note that typically the maximum and minimum concentrations of the external field are quite close to each other in value, for example, as shown in the legend of Figure 46.)

Since the flow described by Figure 44 is symmetrical at the top and bottom, the network drying rate (as seen by liquid distribution within the P-N) seems to be almost symmetric.

The similar situation also happens when we consider the open E+W sides, as shown in Figure 44 (right) shows that the flow in front of the square P-N is ‘squished’ while the flow at the back is ‘stretched’ in terms of the streamline pattern. As a result, the backside CBL is farther away from the pore openings as compared to the front side CBL. However, this does not mean that the concentration gradient is larger in the front and hence there is higher evaporation rate. As mentioned earlier, the largest gradients seem to exist near the open throats which seem to remain unchanged in the front and the back. In fact, the liquid distribution within the P-N (Figure 47)



shows that the front part of the network is depleting rather slowly compared to the back part.

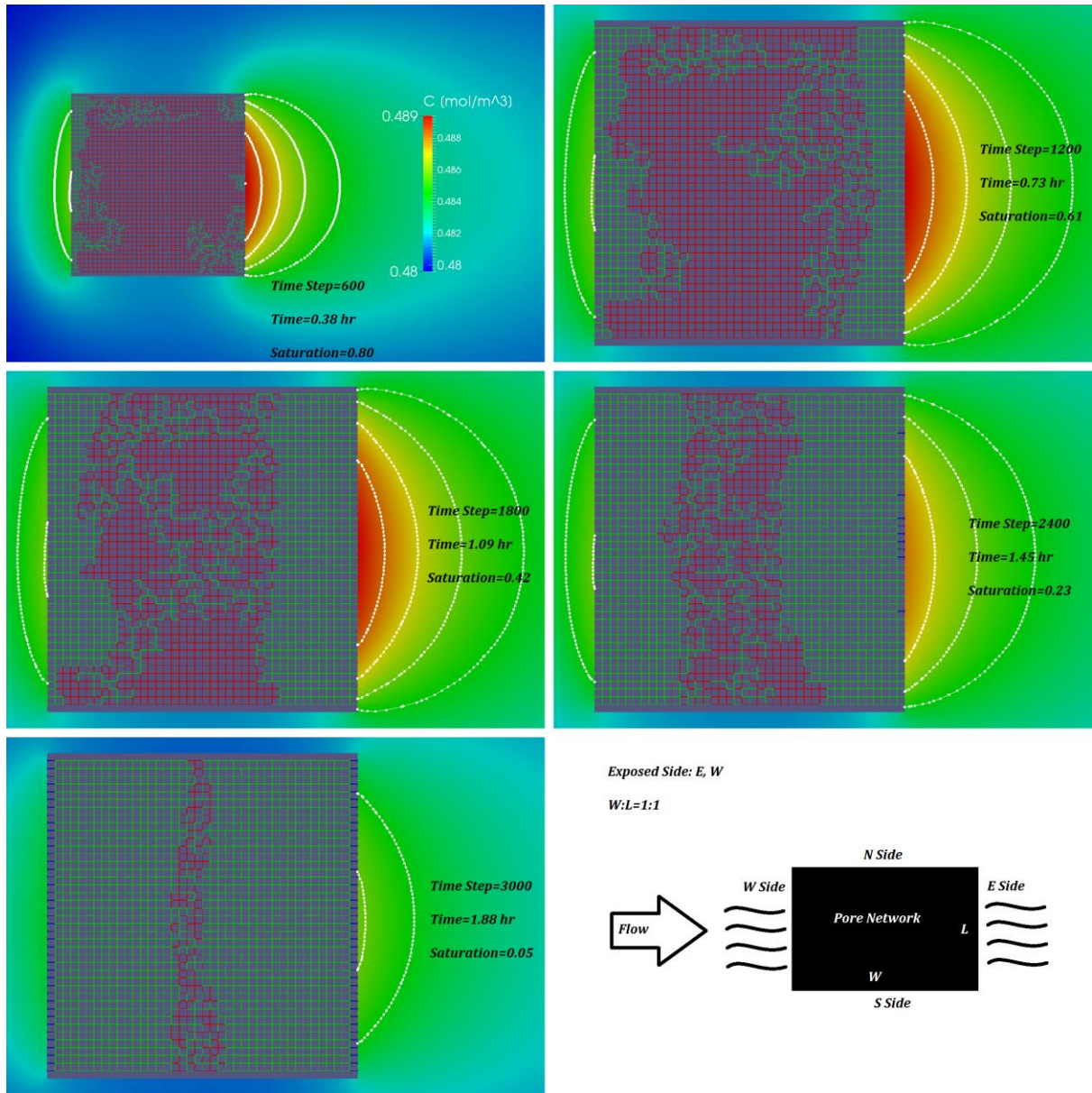


**Figure 47.** Changes in the liquid distribution (within the network) and CBL with time: open E+W sides (the outermost of the iso-concentration lines, the white lines, marks the location of the CBL boundaries)

Opening all sides is almost like adding the previous two cases. The CBL is enlarged and maintained for a long period, as shown in Figure 48. The drying front moves in from all the four

sides. However, the liquid distribution within the network is not symmetric—it seems like a diagonally-aligned patch towards the end of the drying period.

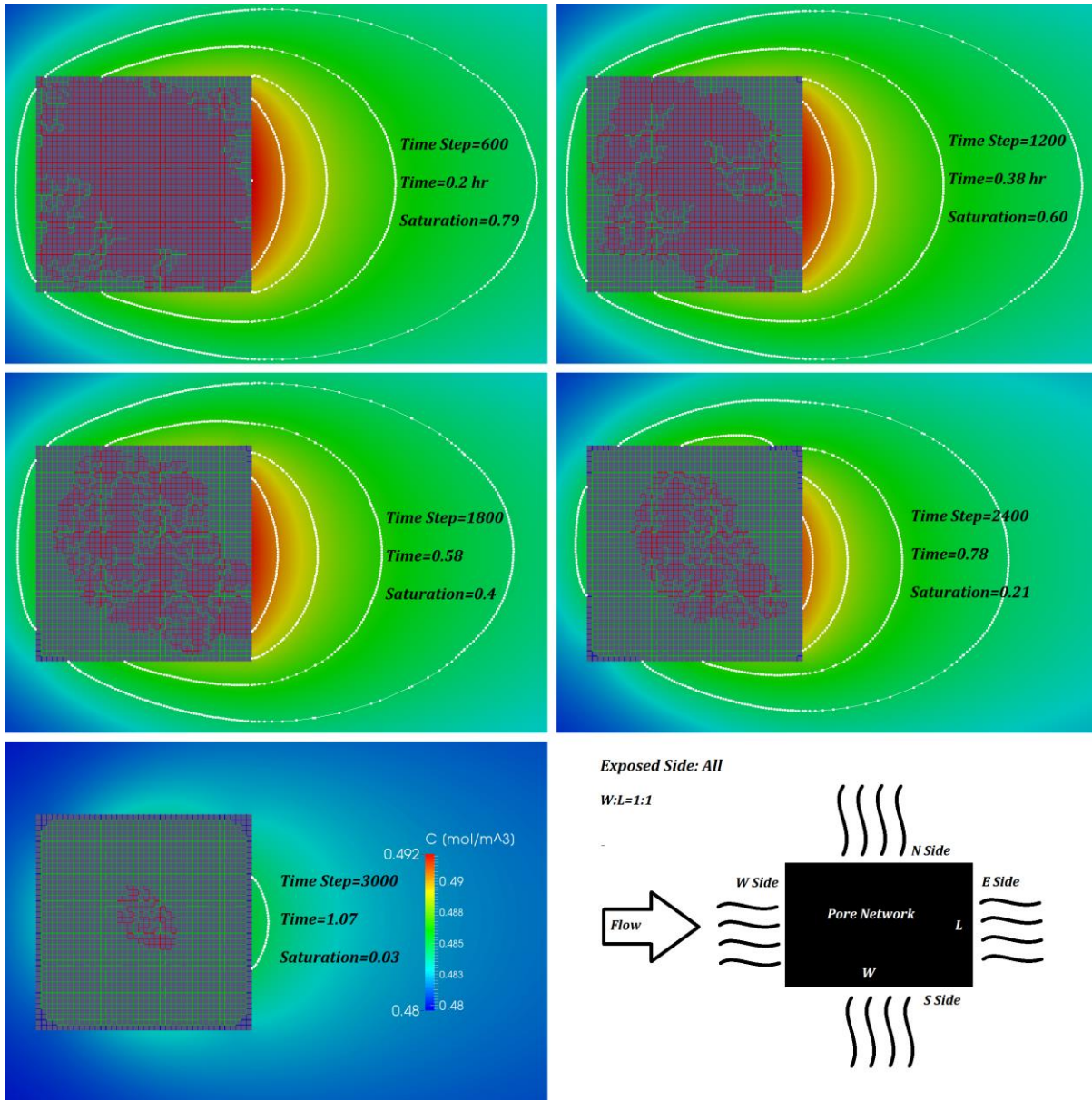


**Figure 48. Changes in the liquid distribution (within the network) and CBL with time: open all sides (the outermost of the iso-concentration lines, the white lines, marks the location of the CBL boundaries)**

It is interesting to note that in the considered cases of open N+S sides, open E+W sides and

open ENWS, the ‘empty’ network is still covered with films till the very end. This implies the total drying rate is proportional only to the open surface available for drying, with the pattern of liquid distribution in terms of liquid-cluster formations seeming to have very little impact. This seems to be evident in Figure 49, where the drying rate for the open-all-side case is only a little bit smaller than the adding of the drying rates for the open-N+S-sides and the open-E+W-sides cases. This fact is corroborated by the fact that the drying time for the open-all-sides case is around half of the drying time corresponding to opening of any two sides.

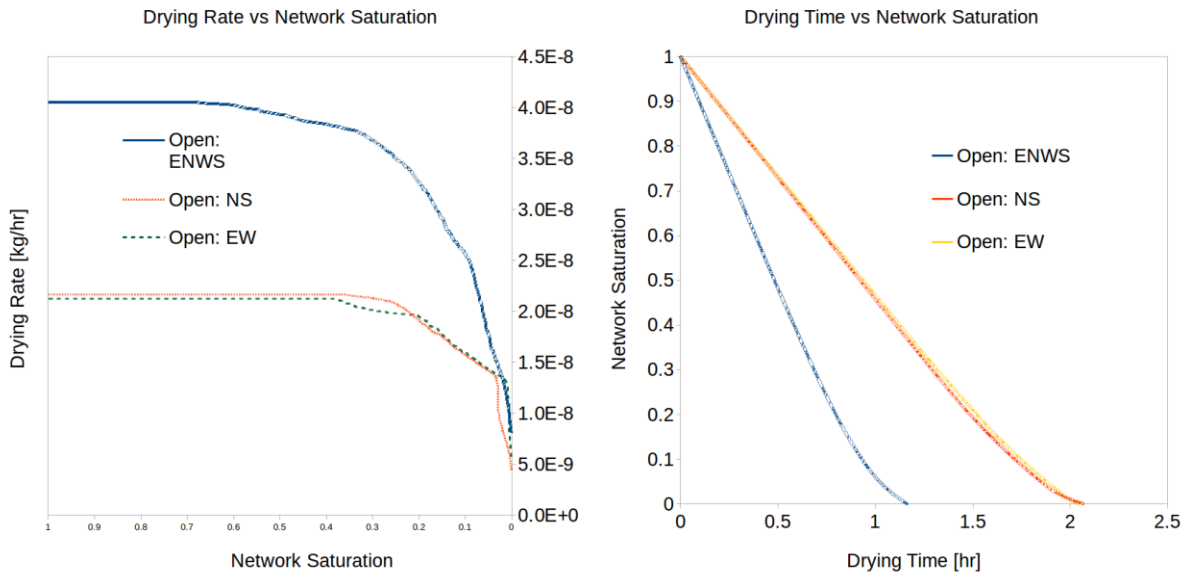


**Figure 49. Drying characteristics of the square pore network when the multiple sides are opened together.**

## 8.2 Drying of Thin Porous Media

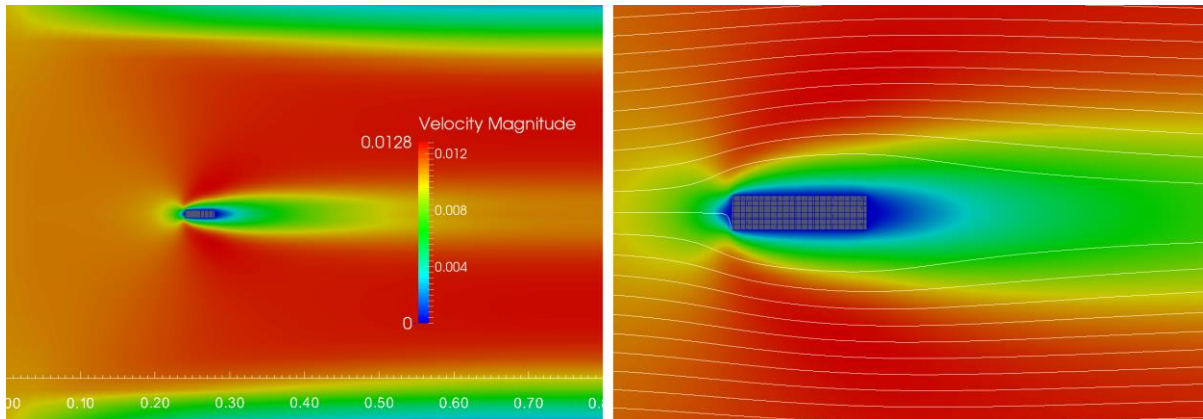
In this study, the throat attributes of the pore network considered till now do not change. Only its aspect ratio is transformed to create a thin porous medium. The outside conditions, pertaining to



velocity and humidity away from the network, also remain the same. In the following cases, the conditions that are studied are: opening all sides, opening the long sides, and opening the short sides.

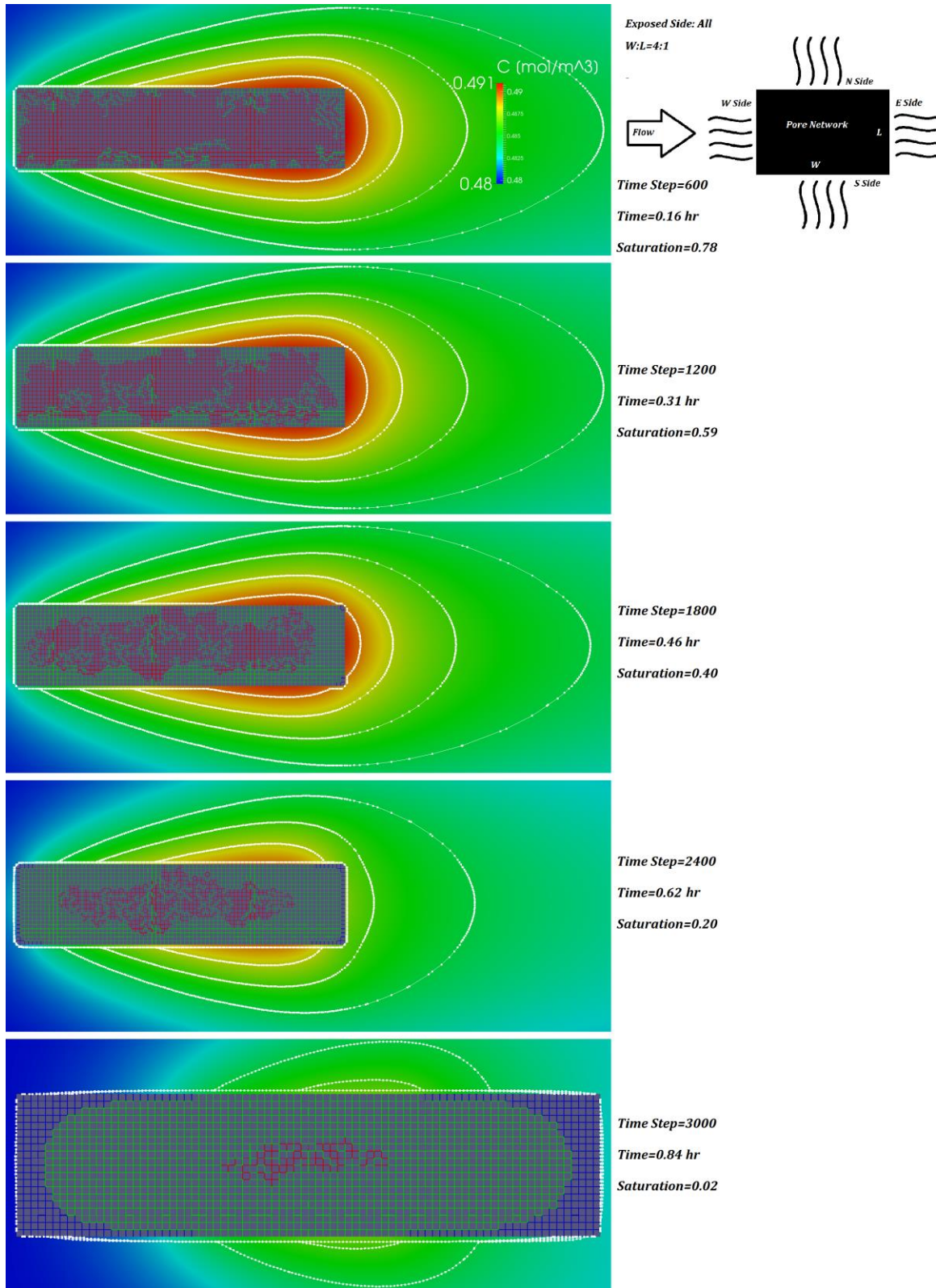
### 8.2.1 Group 3 Simulations: Aspect Ratio=4:1

Here, we study the situation when the domain aspect ratio is 4:1. The corresponding flow field around it is shown in Figure 50.



**Figure 50. Flow around a thin porous medium – horizontal, 4:1 (left: velocity distribution; right: streamline plot)**

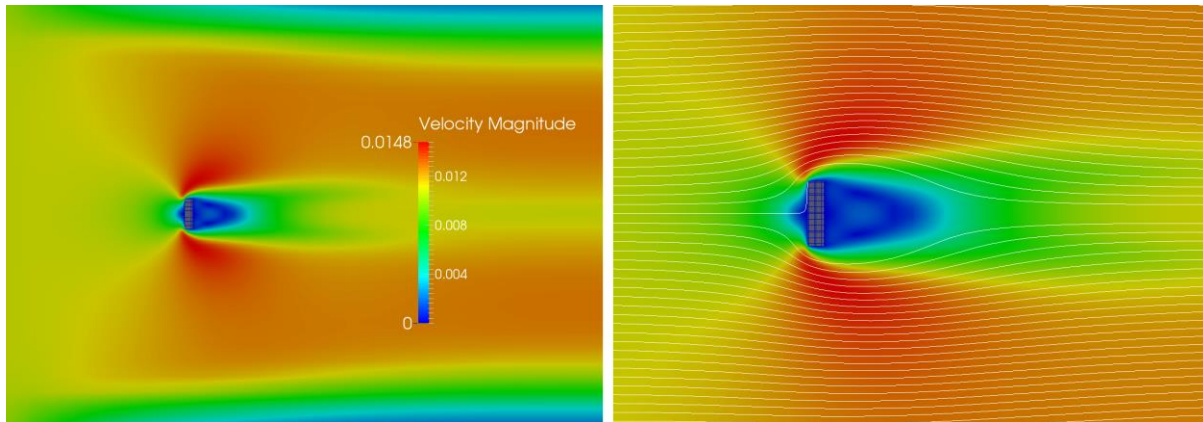
Figure 51 shows the liquid phase distribution within the network and CBL at different times. It shares some common characteristics with the corresponding figure for the square pore network, i.e., the film covers the network for a long time (almost till the end of drying) and the CBL stays unchanged for a long period.



**Figure 51. Changes in the liquid phase distribution (within the network) and CBL with time– horizontal, 4:1**

The case of drying of a thin porous medium kept vertically in the flow field is also studied.

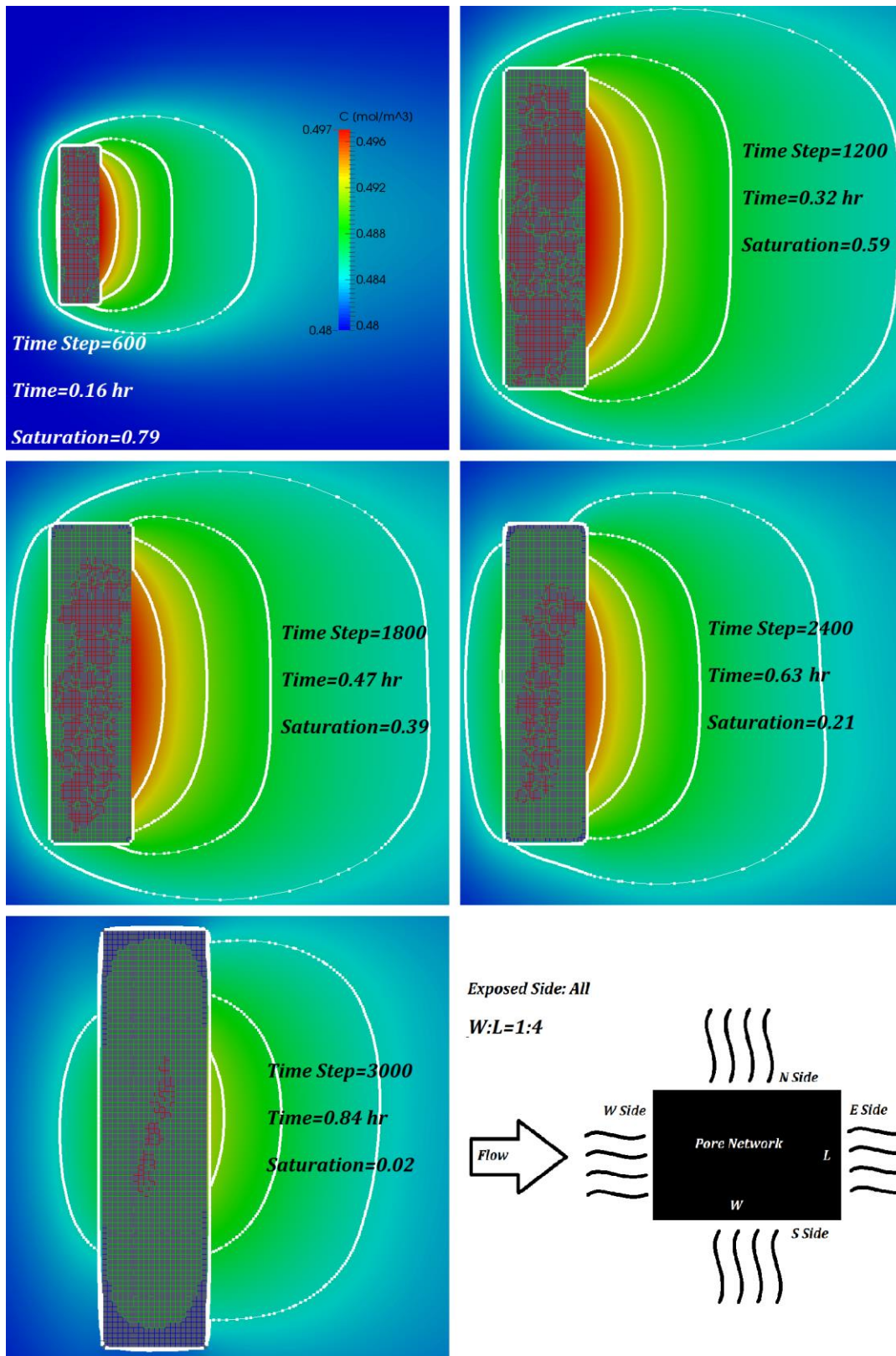
The flow field surrounding the pore network is as shown in Figure 52. Now since the area facing the flow is larger, a wider wake is created in the flow field.



**Figure 52. Flow around a thin porous medium – vertical, 4:1 (left: velocity distribution; right: streamline plot)**

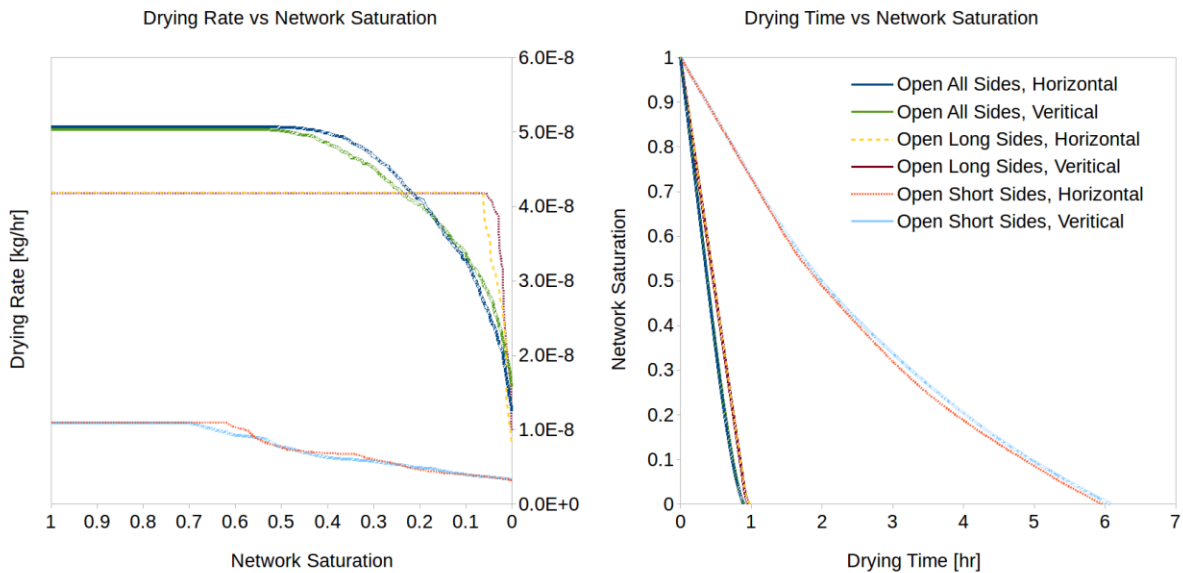
As seen in Figure 53 the pattern of concentration distribution and CBL location is completely different from the last case. But despite this obvious difference, surprisingly, the pattern of drying of pore network remains quite similar to the one seen in Figure 51. As before, the sharpest gradient in concentrations happen very near the pores—there is negligible gradients in the outer flow field. This once again indicates that the *drying is affected by the length of the opened faces rather than by the outer flow field.*





**Figure 53. Changes in the liquid phase distribution (within the network) and CBL with time– vertical, 4:1**

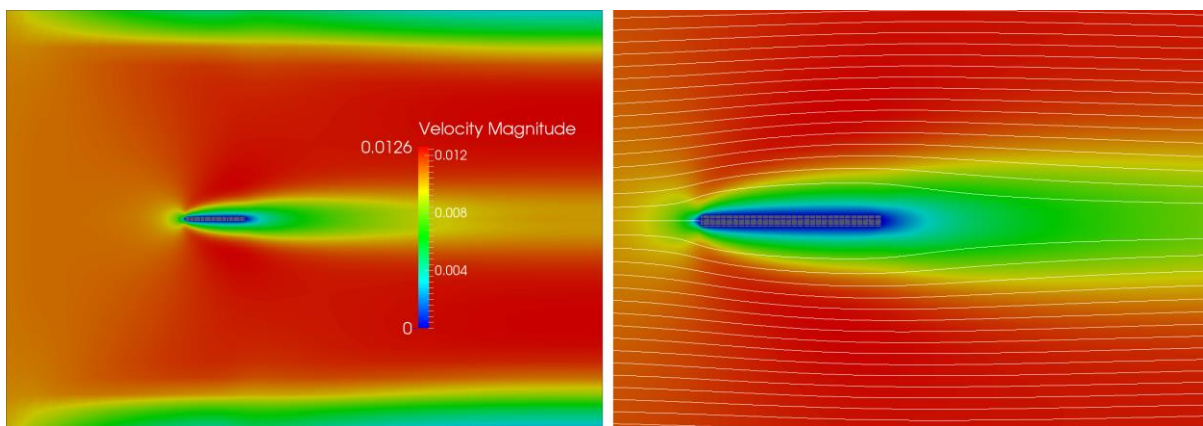
Figure 54 shows the drying rate and drying time for the pore network when opening all sides and opening two sides. Since the outer flow field is playing a minimal role in drying unlike the length of open faces, we observe that the drying rate remains virtually unaffected whether the orientation of the pore network is horizontal or vertical. However, it seems to be directly proportional to the length of open faces. (Note that the drying rates for the open-short-sides, open-long-sides and open-all-sides cases are approximately in the ratio 1:4:5 which matches the lengths of their respective open faces.) The overall drying times of the network are inversely proportional to the drying rates: the open-short-sides, open-long-sides and open-all-sides cases have their corresponding drying times in a reducing order.



**Figure 54. Drying characteristics of the thin pore network with 4:1 aspect ratio when the multiple sides are opened**

## 8.2.2 Group 4 Simulations: Aspect Ratio=16:1

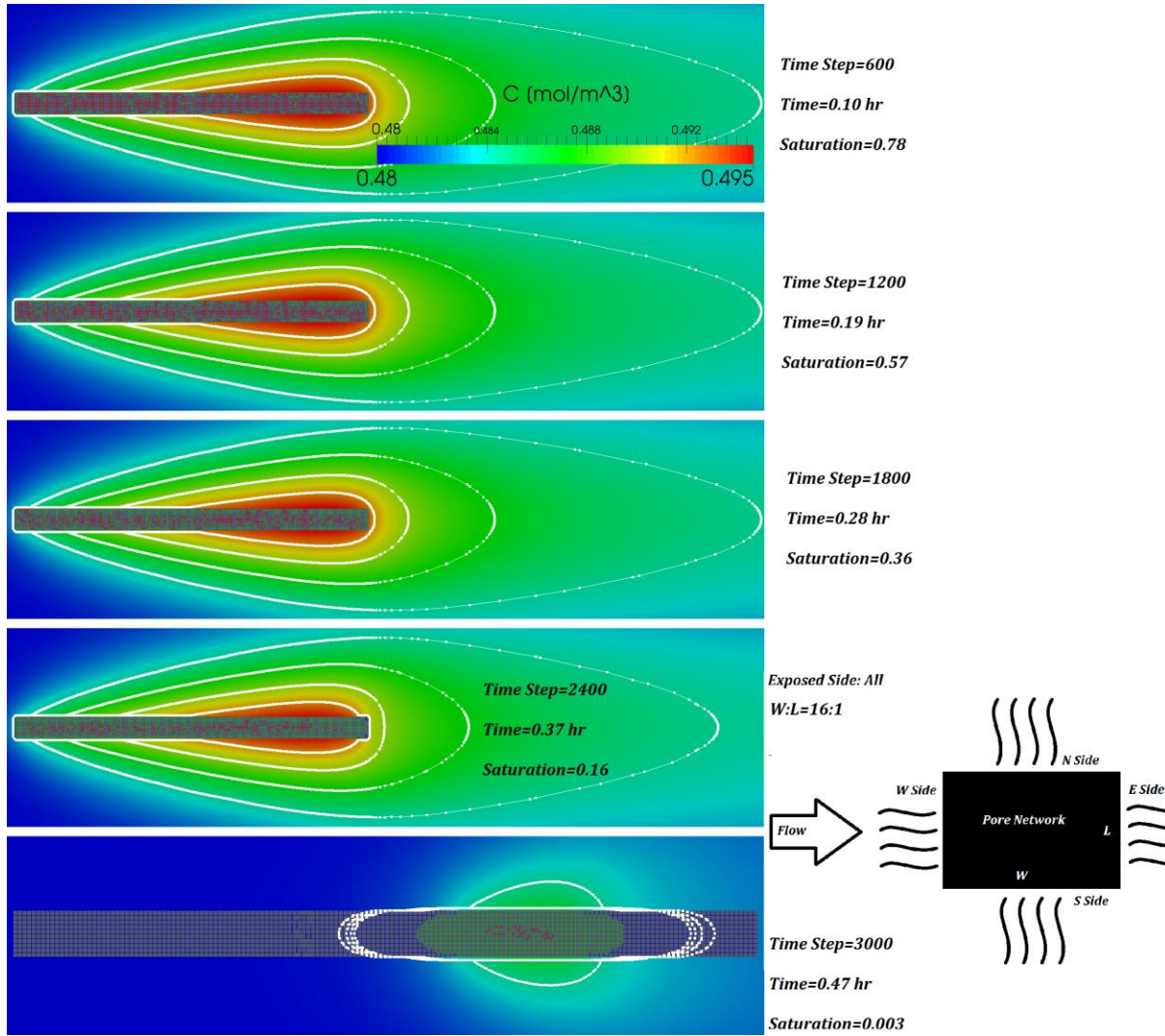
Similar to the previous case, a thin porous media with aspect ratio 16:1 and with all its sides open is inserted in the flow field and its drying studied. First Figure 55 shows the velocity distribution and a plot of streamlines around it. Because of the long, slender shape of the obstruction, the effect on the uniform flow field is quite small and the wake is quite narrow.



*Figure 55. Flow around a thin porous medium – horizontal, 16:1 (left: velocity distribution; right: streamline plot)*

Figure 56 shows the corresponding progress with time of liquid-phase distribution inside the pore network as well as the vapor concentration distributions. As expected, the CBL remains virtually unchanged till the very last. The saturation pattern is virtually the same along the length of the slender pore network—the drying front has invaded uniformly along the whole length, the empty network is wholly occupied with the film, and the liquid phase is increasingly confined to a narrow band along the center line. The interesting part is that at the final stage of drying, all the other parts of the porous medium are dry except for a small oval spot of liquid saturation at the

center of the rear half. Because the pore network is long in one direction, the length-wise retreating of the film is well observed towards the end of the drying process.



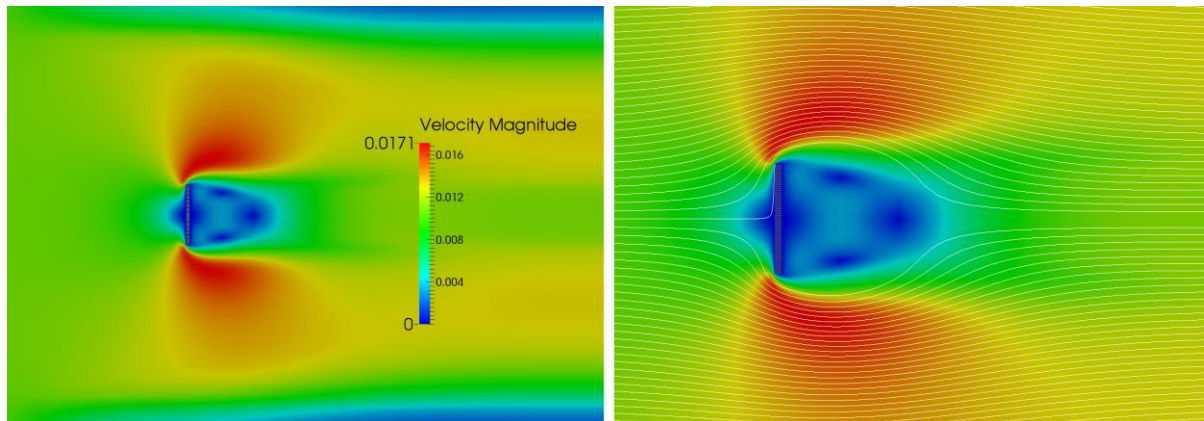
**Figure 56. Changes in the liquid phase distribution (within the network) and CBL with time- horizontal, 16:1**

Figure 57 and Figure 58 are about putting this thin porous medium vertically in the flow field. As expected, a large wake is formed behind the slender pore network. The pattern of concentration distribution and CBL location is quite similar to the earlier case of in Figure 53. However, unlike



the previous case, two wet spot are observed inside the pore network at the final stages of drying.

One can also observe the shrinking of two elliptical film regions around these wet spots.



**Figure 57. Flow around a thin porous medium – Vertical, 16:1 (Left: velocity distribution, Right: streamline plot)**

Figure 59 compares the cases of opening all sides or two long sides or two short sides. The trend is similar to the one seen in the previous experiment (Figure 54); in fact, the results have become more extreme with the increasing aspect ratio. The drying rate and drying time plots for the open-all-sides and open-long-sides come closer as the length of the short side becomes smaller. The drying rates and times for the open-short-sides are extremely different from the former two cases. This clearly indicates that the effect of side walls on drying has now become insignificant.



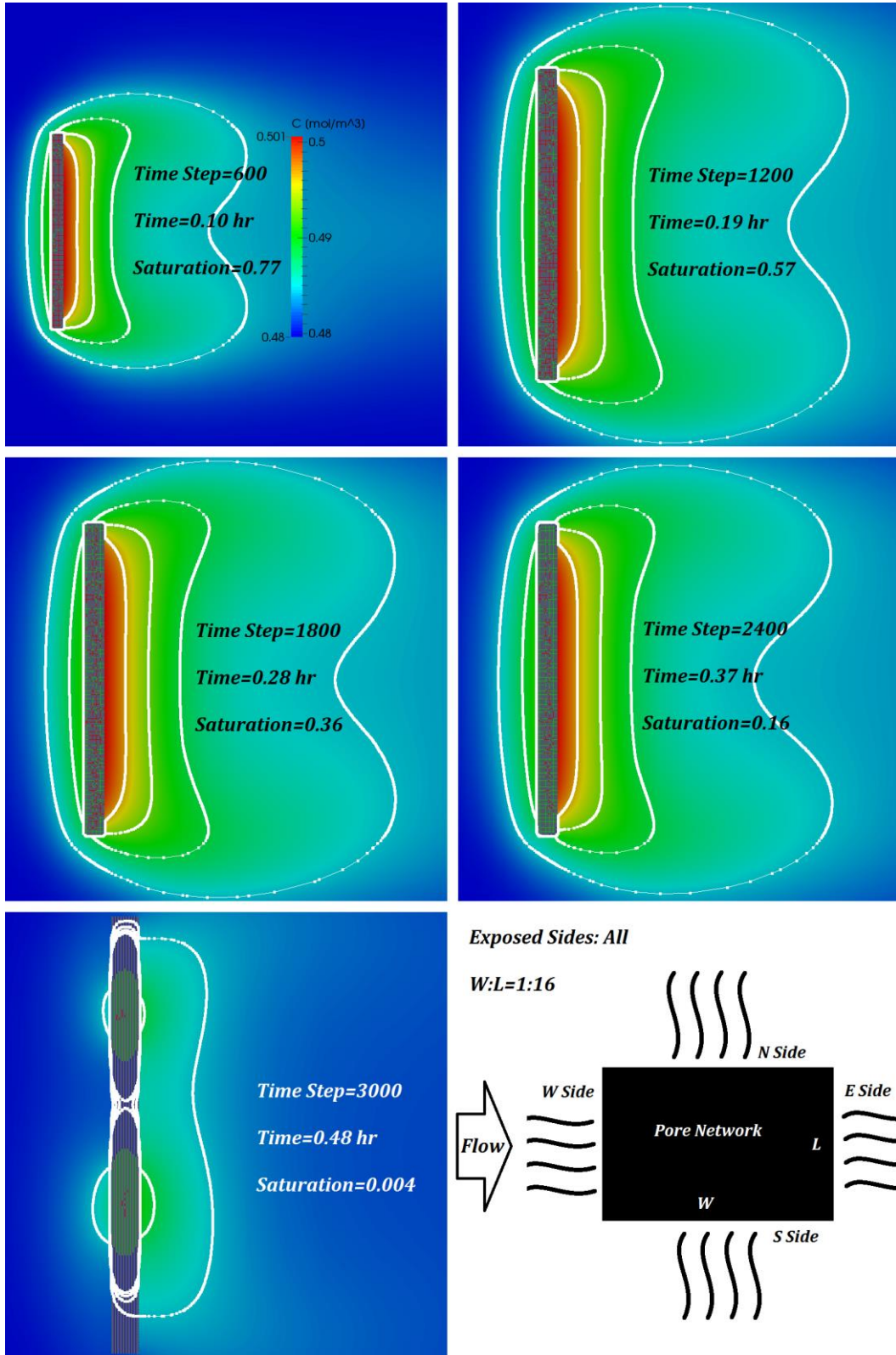
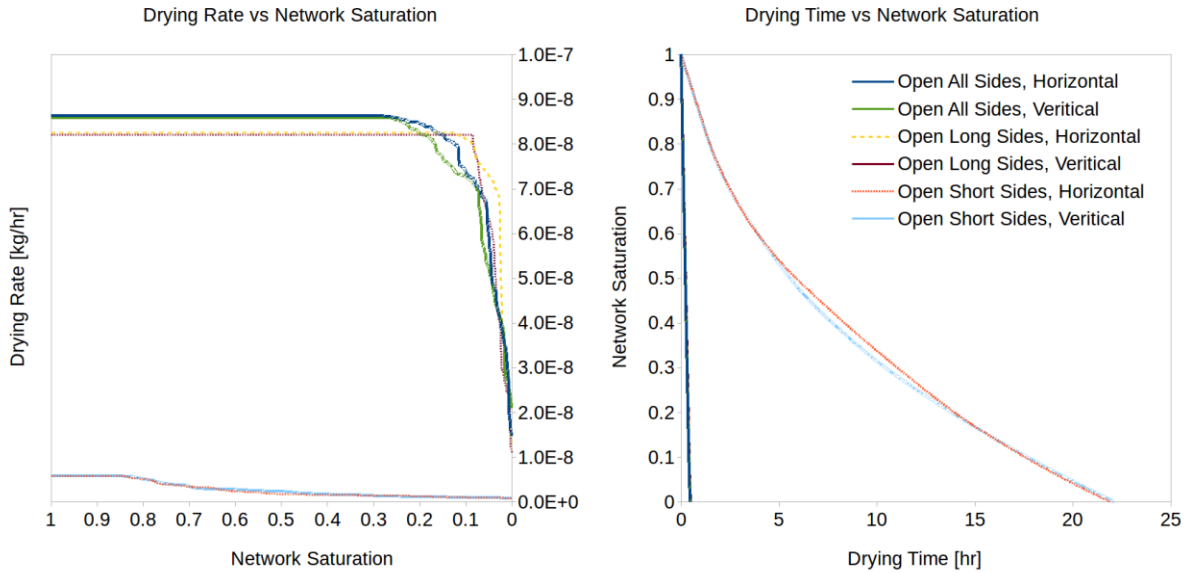


Figure 58. Changes in the liquid phase distribution (within the network) and CBL with time- vertical, 16:1



**Figure 59. Drying characteristics of the thin pore network with 16:1 aspect ratio when multiple sides are opened**

### 8.3 Comparison Between Different Aspect Ratios

As we saw in our studies, a square  $40 \times 40$  pore network can be transformed into a  $80 \times 20$  network (4:1 aspect ratio) or a  $160 \times 10$  network (16:1 aspect ratio).

A comparison of the drying rates and drying times yield some interesting insights. Figure 60 allows us to conclude that a larger aspect ratio has a better drying rate and a shorter drying time. Let us look for an explanation this. The  $160 \times 10$  porous medium has 336 opening (surface) pores and 3030 full (internal) throats. The  $40 \times 40$  porous medium has 156 opening (surface) pores and 3120 full (internal) throats. The ratio of the full-throats count by the opening-pores count for the  $160 \times 10$  network is around 9, while this value for the  $40 \times 40$  network is 20. Note that this 20/9 ratio is almost equal to the drying-time ratio between the two cases. From this point of

view, the thin porous media dry faster because they have more exposed edges and less volume. In other words, *the area to volume ratio for a body has to be higher in order to achieve faster drying characteristics.*

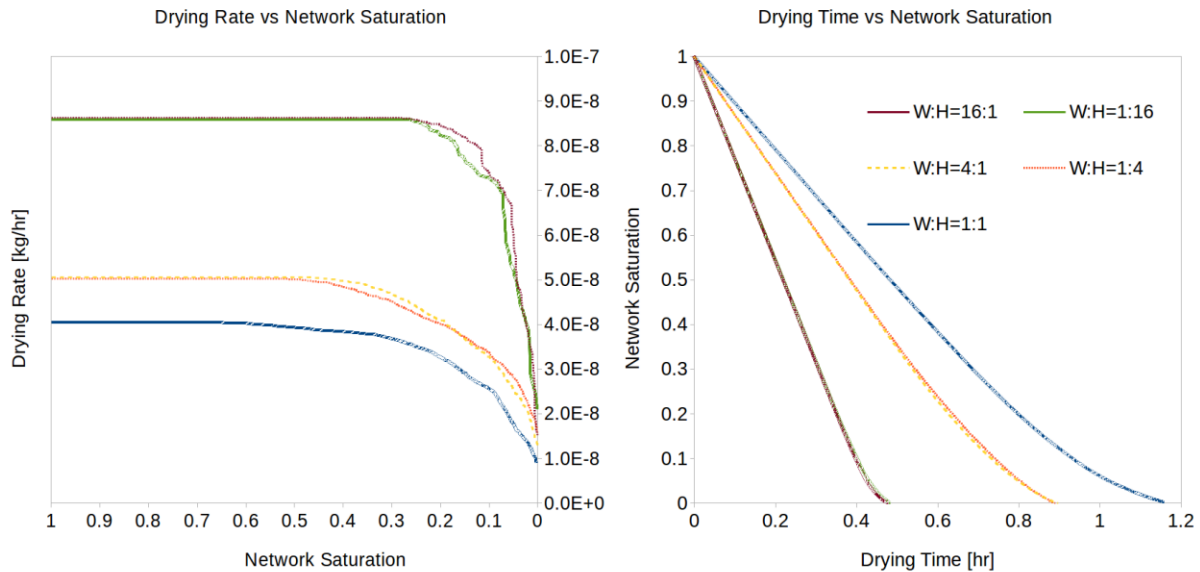


**Figure 60. A Comparison of drying characteristics of pore networks with different aspect ratios ( $W$  and  $H$  represent the P-N width and height, respectively)**

It is also important to note that *the drying characteristics for thin porous media do not change much whether they are aligned with the flow or standing perpendicular to it.*

## 8.4 Summary & Conclusions

This chapter used the model developed in chapter 5 to study pore networks with different aspect ratio positioned in the flow field. The presence of film during most of the drying period ensures that the surface pores are at saturated vapor pressure. As a result, the sharpest concentration gradients, which also control the drying rates, lie adjacent to the exposed surfaces.

Consequently, the concentration gradients in the outer flow fields are very mild and play insignificant role in the drying of this porous media. Hence orientation of thin porous media in the outer flow field is irrelevant for drying.

The studies also show that the thin porous media have larger drying rates and shorter drying times because of their larger exposure-area versus volume ratios.

## 9 DRYING OF DUAL-POROSITY PORE NETWORK

Now we will start our work on modeling drying dual-scale or dual-porosity porous media saturated with water.

### 9.1 A Comparison with Experiment

In this study, our simulation results will be compared with the results from a drying experiment done earlier in a dual-porosity pore network (Pillai, et al., 2009). The lower half of the network is composed of randomly distributed square throats ranging in  $D$  between  $0.1\sim 0.2\text{ mm}$ , and the upper half is composed of randomly distributed square throats ranging in  $D$  between  $0.7\sim 0.8\text{ mm}$ . The throat length and thickness are the same at  $1\text{mm}$ .

The experiment (Figure 61) is conducted under the conditions of environmental humidity being at 6%, and with the wind speed caused by fan-induced external circulation being unknown. In the simulation we set the environmental humidity to be 6% and did the simulations under two different air velocities corresponding to Peclet number being 100 and 400 respectively. (We used the hydraulic diameter of the network to calculate the Peclet number.) When the large-pore side is open and the external  $Pe = 400$ , the total drying time of simulation is 14.59 hours, which comes close to the experimental results of 14.16 hours. When the small-pore side is open and the external  $Pe = 100$ , the total drying time of simulation is 30.30 hours, which is close to the experimental results of 31 hours. Because the experiments were conducted under 3D conditions while our

simulation is 2D, it is hard to mimic the exact external conditions. So we manipulate the external conditions through changing the circulation speed to find a suitable setting for better drying-time agreement. A 3D study should be carried out in the future to clear this point.

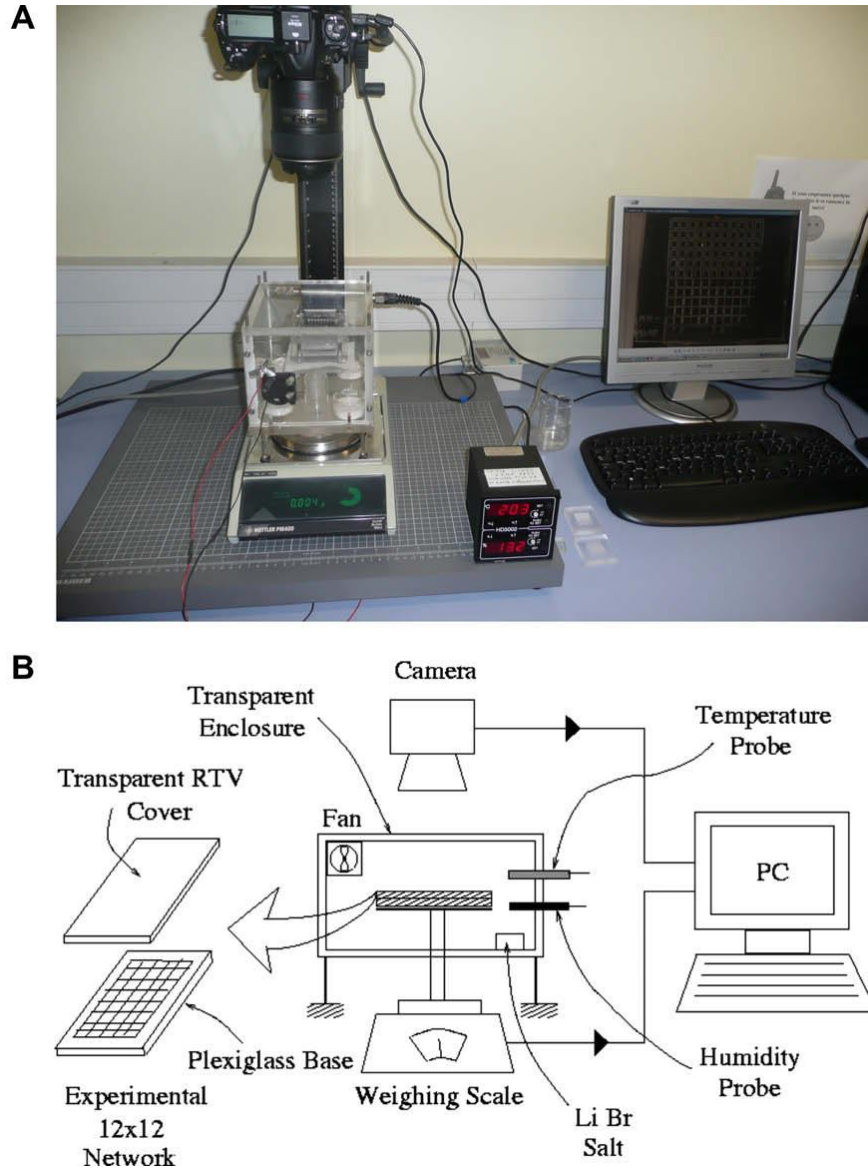


**Figure 61. Dual-porosity experiment setup (A: picture; B: a schematic describing elements of the setup; picture comes from (Pillai, et al., 2009) )**

As shown in Figure 62, we considered four different cases by altering  $Pe$  between the two

values and by opening the small-pores or large-pores sides. Interestingly the drying rates for all the four cases are constant from the beginning of the drying till the end. This is because since the throat size is relatively large for the chosen  $12 \times 12$  pore network, long enough film fingers are generated extending all the way till the network boundary during the entire drying process.

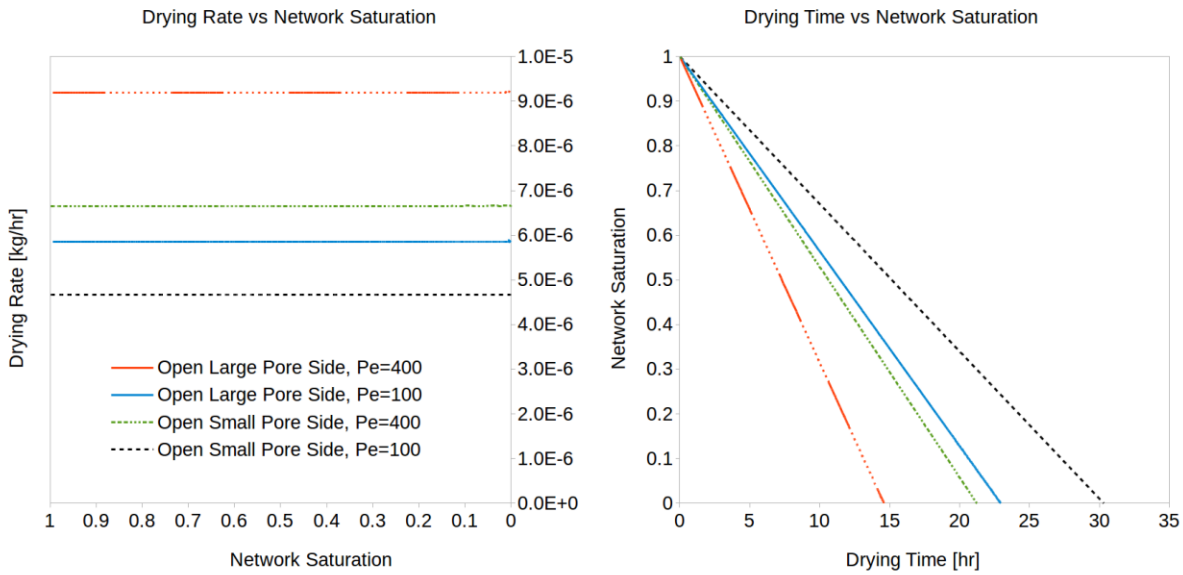


**Figure 62. Prediction of drying rate and drying time as a function of network saturation for the  $12 \times 12$  dual-porosity pore network**

As stated in (Pillai, et al., 2009), the experimental network has a large uncontrollable machining error of  $10\mu m$ . Moreover, the randomly-assigned throat dimensions were carefully matched in the experiments and the simulations of this published study. Since we cannot duplicate the exact same network for our current simulation, the liquid-phase distributions at different times will not have an exact match between experiments and the current simulation. But we compared the phase distribution at a critical time, when half of the throats are dry. As we can see from Figure 63, the simulation results match well with those of the experiments, especially in the case of

opening the large-pores side. This should be treated as a partial validation of our simulation.

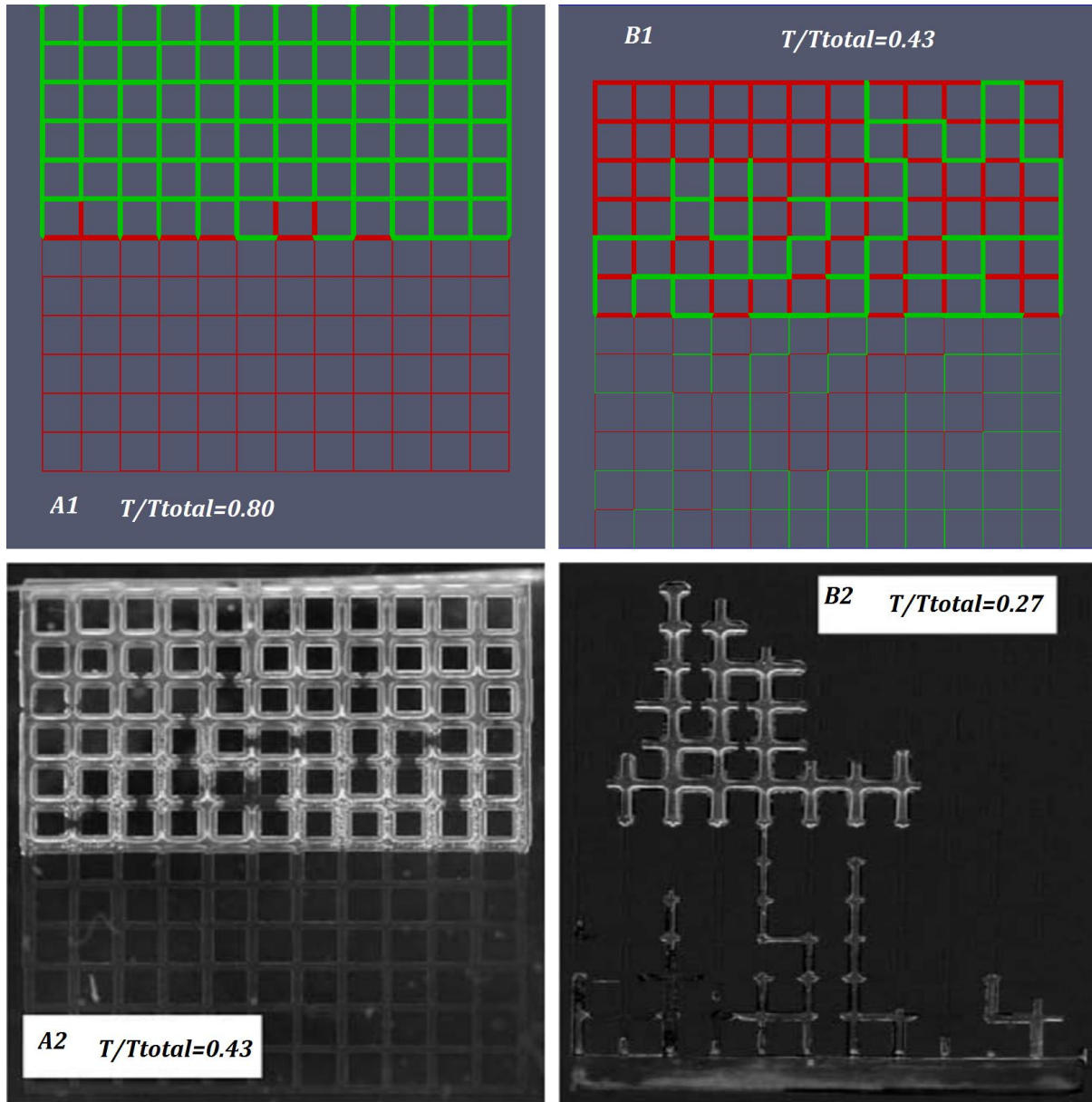


**Figure 63. Phase distribution of simulations -  $12 \times 12$  dual porosity pore network (A1: simulation results when the large-pores side is open with  $Pe = 400$ ; A2: experimental results when the large-pores side is open; B1: simulation results when the small-pores side is open with  $Pe = 100$ ; B2: experimental results when small side open; A2 and B2 are coming from (Pillai, et al., 2009) )**

We also compared the dimensionless plots of drying mass versus drying time as shown in Figure 64. The experimental results are obtained from (Pillai, et al., 2009). If the film effect is



considered, because the drying rate is constant during the entire drying process, the plot of drying mass vs drying time is a straight line. However, if the film effect is not considered, the drying rate changes as the drying progresses, and hence the obtained plot is a curve. Especially in the case of opening the small-pores side, the characteristic bilinear curve is observed.

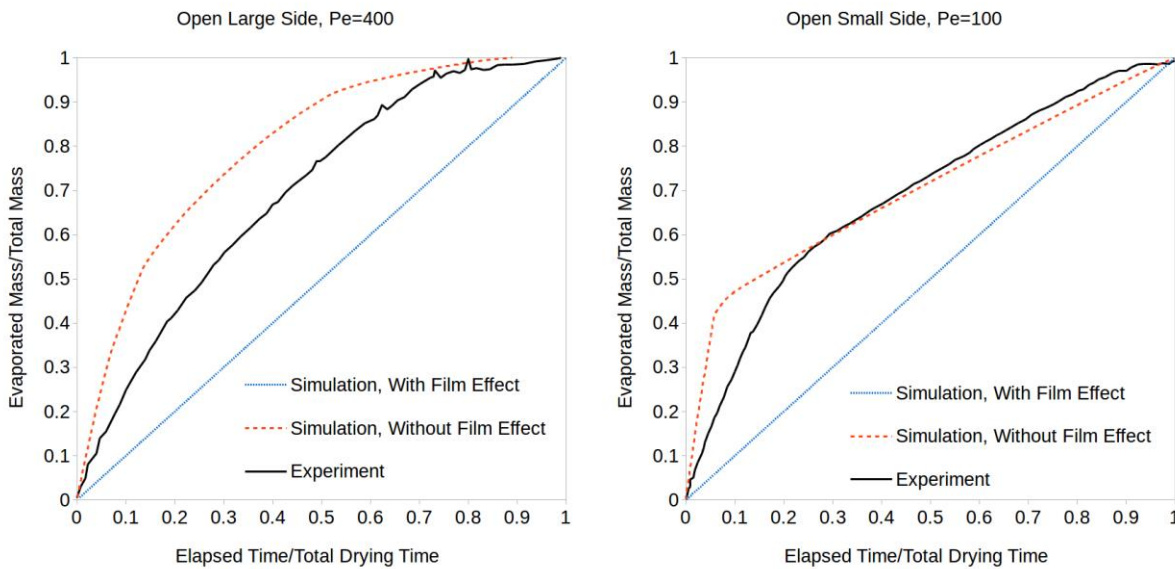


**Figure 64. Dimensionless drying mass vs drying time – comparing with the experiment**

From Figure 64 we can see, the experimental results are actually closer to the simulation results when the film effect is ignored. (This is true as far as the trends are concerned; however, the total drying time predicted by the film-less simulation is inaccurate by an order of magnitude.)

This phenomenon may be due to two reasons. Firstly, our film effect model assumes a constant film radius when it is close to bulk liquid at the saturation front; and the value is usually chosen to be the average  $R_M$  of all the throats (refer to Eq. (22)). This assumption works well when the largest and smallest throats are in a narrow range. In the case of dual-scale porous media, as

implied by its name, the  $R_M$  of the largest throat and  $R_M$  of the smallest throat are in two different scale. However, we still use the average value of  $R_M$  to represent all the throats, which actually diminished the difference between the two scales. Secondly, the pore network in the experiment may have machining errors. Because the film effect model shows that even the smallest throats of  $0.1\text{mm}$  in this network will generate a long enough film to sustain a constant drying rate through the entire drying process. As discussed in the previous section as well as in (Prat, 2007), the throat cross section shape has a major influence on the resulting film effect. If the cross section of the throats changes from square to hexahedral due to the machining error, or if there are any round corners existing in square cross-sections, the film effect, as shown in Figure 41, may be decreased significantly. So we cannot exclude the possibility that the network machining errors may be the cause of the above-mentioned deviations.

## 9.2 Square Pore Network in the Center

Here we study the drying of a dual-porosity pore network positioned at the center of a uniform flow field. By the opening sides of the pore network to the flow field, the interactions between the pore network and the outside field is initiated and the resultant drying process studied.

The basic form of the pore network is  $100 \times 100$ ; the throat length is  $500\mu\text{m}$ ; the throat hydraulic diameter of the lower (smaller-pores) portion of the network range in  $5\mu\text{m} \pm 5\%$ , and of the higher (larger-pore) portion range in  $10\mu\text{m} \pm 5\%$ .

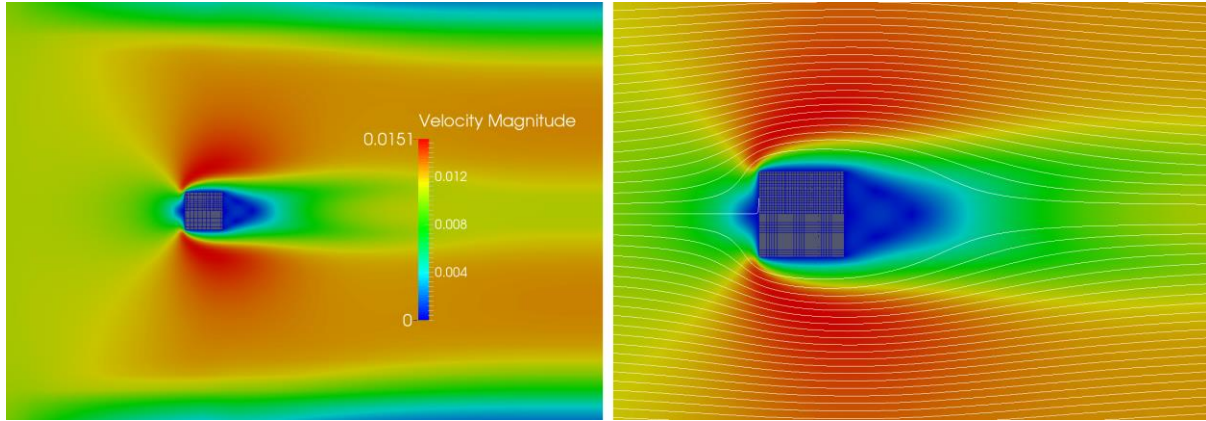


**Figure 65. Velocity field around square pore-network,  $Pe = 10$  (left side: velocity contour; right side: stream lines)**

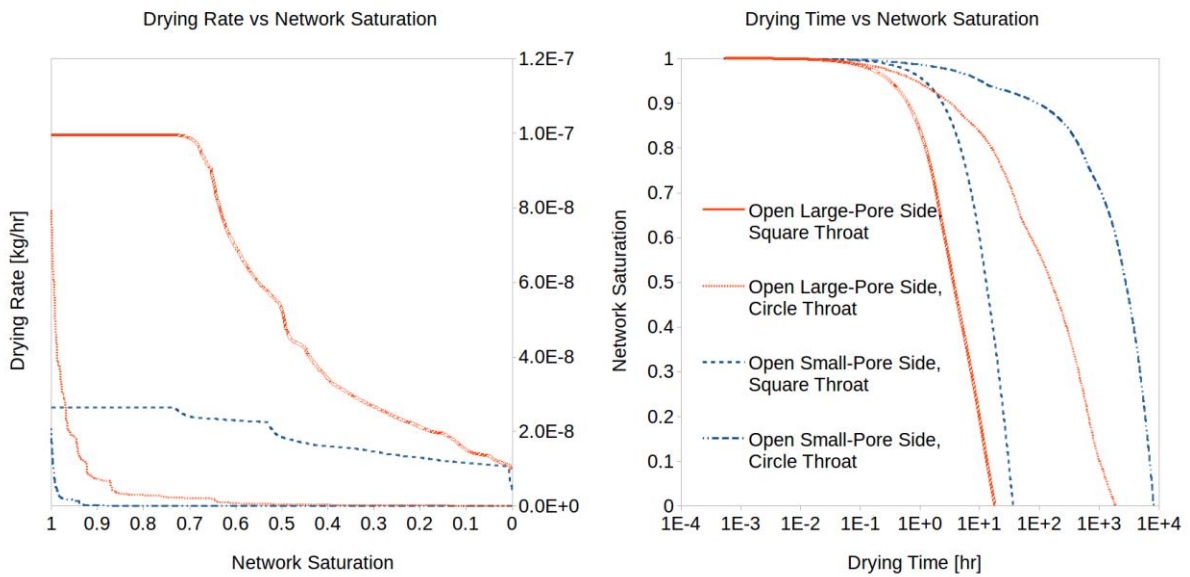
The position of pore network in the flow field is as shown in Figure 65. This is the surrounding velocity distribution for  $Pe = 10$ . The environment humidity is set at 50%.

### **9.2.1 Group 1 Simulations: One Side Open**

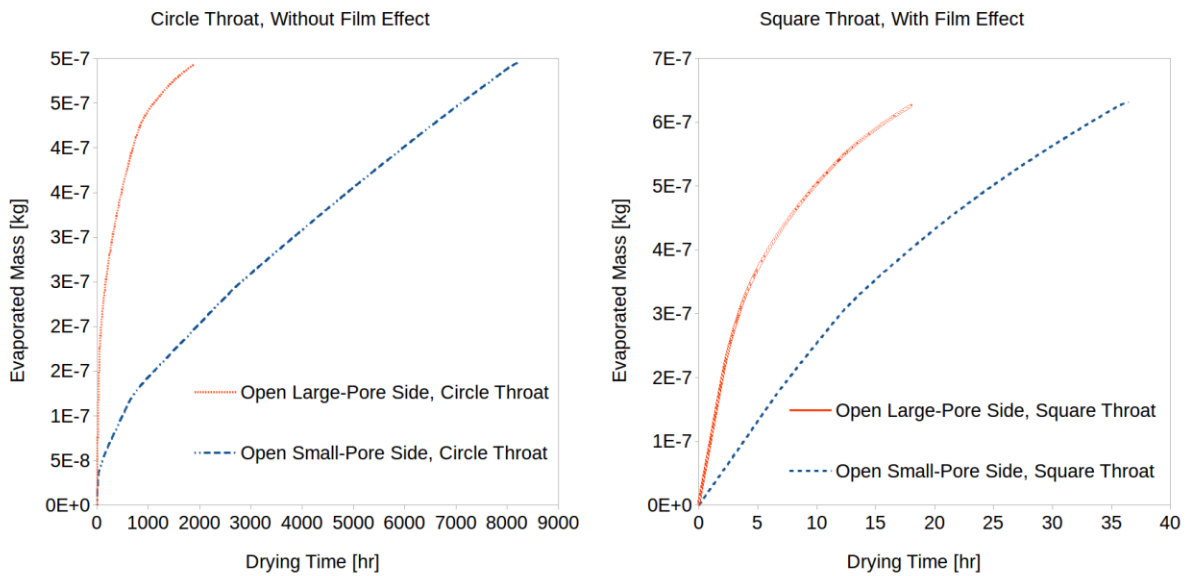
In our first group of simulations, we seal three sides of the network and open only one side. The north (top) side of the network is the larger-throat side, while the south (bottom) side is the smaller-throat side. We used networks made either of the square cross-section throats or the circular cross-section throats. The latter, for their characteristic of not allowing any film effect, are used to compare with the previous ‘film-less’ simulation done by (Pillai, et al., 2009).

Figure 66 shows the drying rates and drying times of all the cases considered in this study. Observe that when the film effect exists in the networks with square cross-section throats, the drying time is exponentially less than that for the corresponding networks with circular cross-section throats. Also note that the drying time for opening the large-pores side of the square

network is shorter than that for opening the smaller-pores side.



**Figure 66. Drying of dual porosity networks with one side open**



**Figure 67. Studying the drying characteristics of a dual-porosity network – with/without film effect**

To compare with the previous research on drying of a dual-porosity network, we also plotted the chart of drying mass vs drying time for cases without the film effect in Figure 67. This shows

exactly the same trend as observed in (Pillai, et al., 2009): the curve corresponding to opening the large-pores side is smoother, while the curve corresponding to opening the small-pores side generates a bilinear trend reported by Pillai et al. In addition, because of the film effect, the drying-rate difference is decreased—the two curves in the right figure are closer compared to the left figure. Also note that the difference in slopes of the two linear segments of the bilinear curve corresponding to the small-pores side open is smaller after including the film effect.

It is also important to notice the huge difference in the time scales involved—the drying of the circular cross-section throat network is in thousands of hours compared to the tens of hours needed to dry a square cross-section throat network! This basically highlights the incredibly important role played by liquid films in slow drying of porous media.

Let us now study the drying of the two types of dual-porosity networks in greater detail. Figure 68 shows the drying of the case when opening the larger-pores side—as shown in the figure, the larger pore region dries out completely before the drying front starts penetrating the smaller region region. This is similar to the observations reported in (Pillai, et al., 2009) for a network with no films and a constant-thickness CBL.

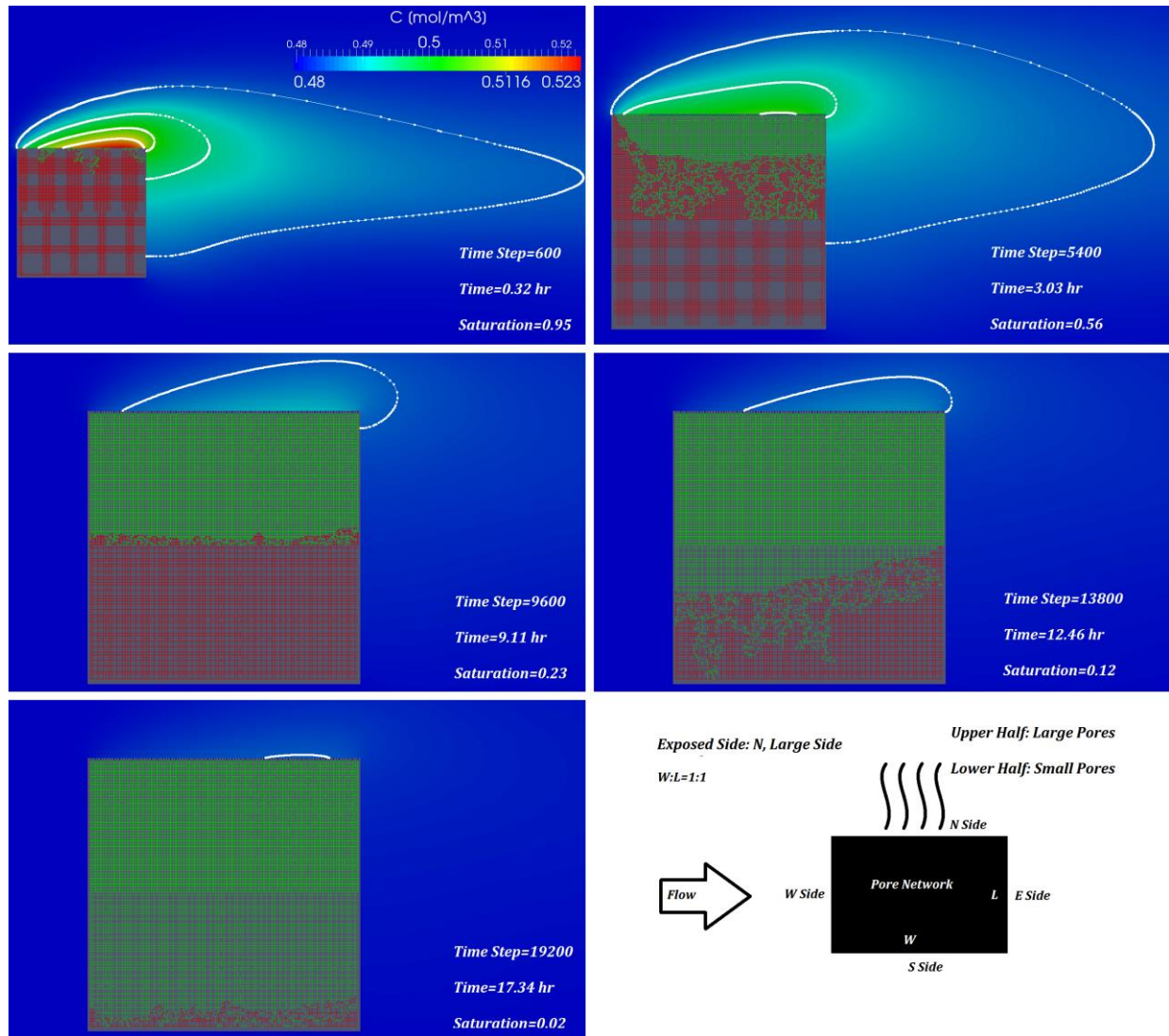


**Figure 68. Evolution of liquid-phase distribution and CBL with time in the dual-porosity network using square throats with film effect—the large-pores side is open (The outermost constant concentration curve is the CBL.)**

However, when the smaller side is open, it is a different scenario altogether (Figure 69). Even before the pores in the outer small-pore region fully dry up, the drying front starts penetrating the inner large-pore region. As postulated by (Pillai, et al., 2009), the phenomenon of ‘capillary pumping’ is at work—in a liquid cluster spanning the smaller and larger pores, the liquid migrates from the latter into the former as the capillary pressure is larger in the smaller pore region. As a



result, the larger pore region empties even as the smaller pore region exhibits small change in the liquid-phase distribution.

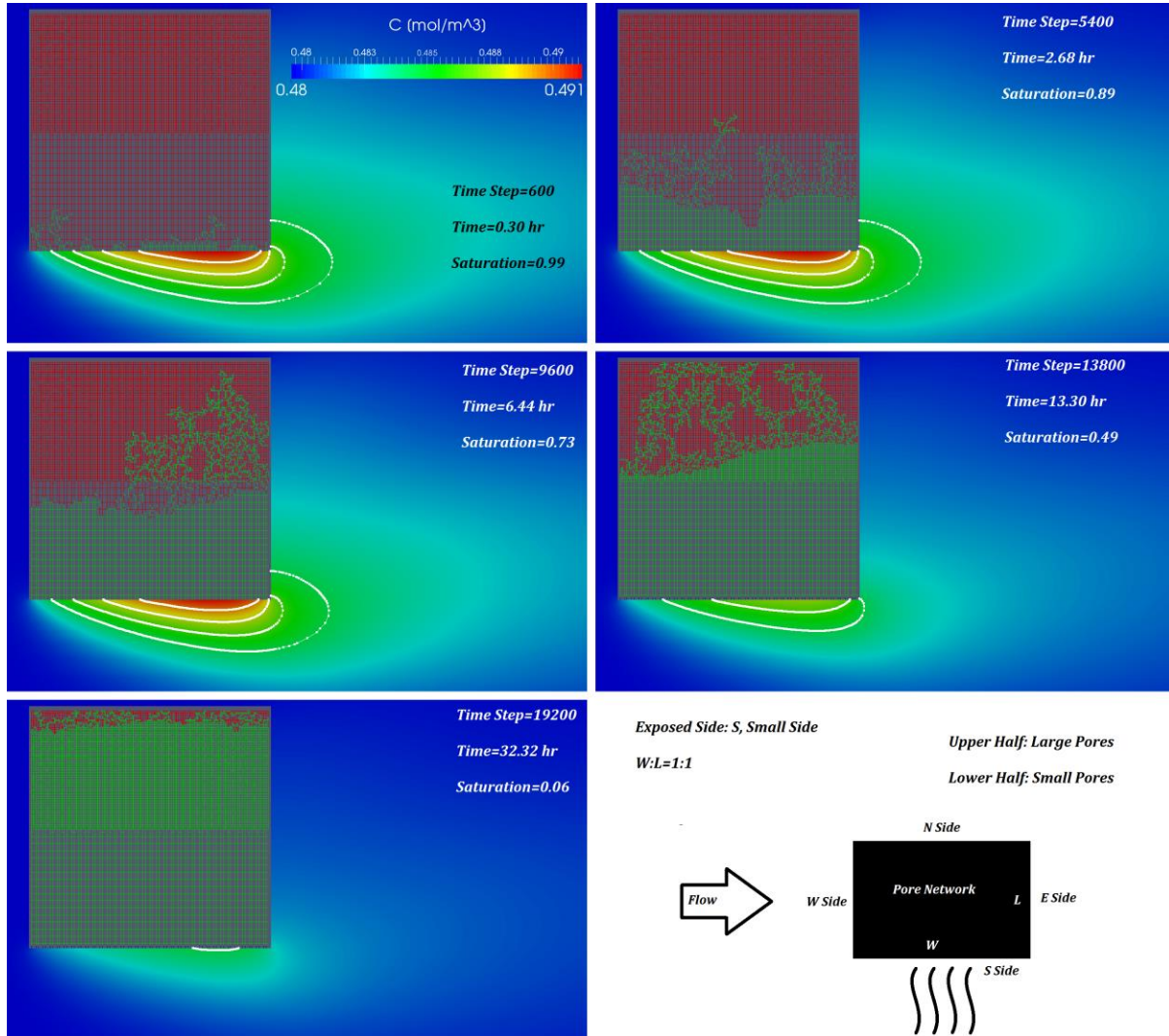


**Figure 69. Evolution of liquid-phase distribution and CBL with time in the dual-porosity network using square throats with film effect—the small-pores side open (The outermost constant concentration curve is the CBL.)**

On comparing the two above-mentioned cases, we can find that the influence of the larger-pore side open to the outside is more significant because more liquid is transported out from the porous medium into the outer flow field. (Note that the drying rate in the former is much higher

as shown by Figure 66 and Figure 67.)

Also the fact that the larger pores dry out completely before the small pores allows one to infer that such a system can be used to design an incense or an insect-control vapor delivery system: the outer pores can be filled with one type of evaporating liquid compared to the inner pores such that the first type is delivered first to the outer air field before the second type kicks in.

### 9.2.2 Group 2 Simulations: Influence of Irregularity in Pore Geometry

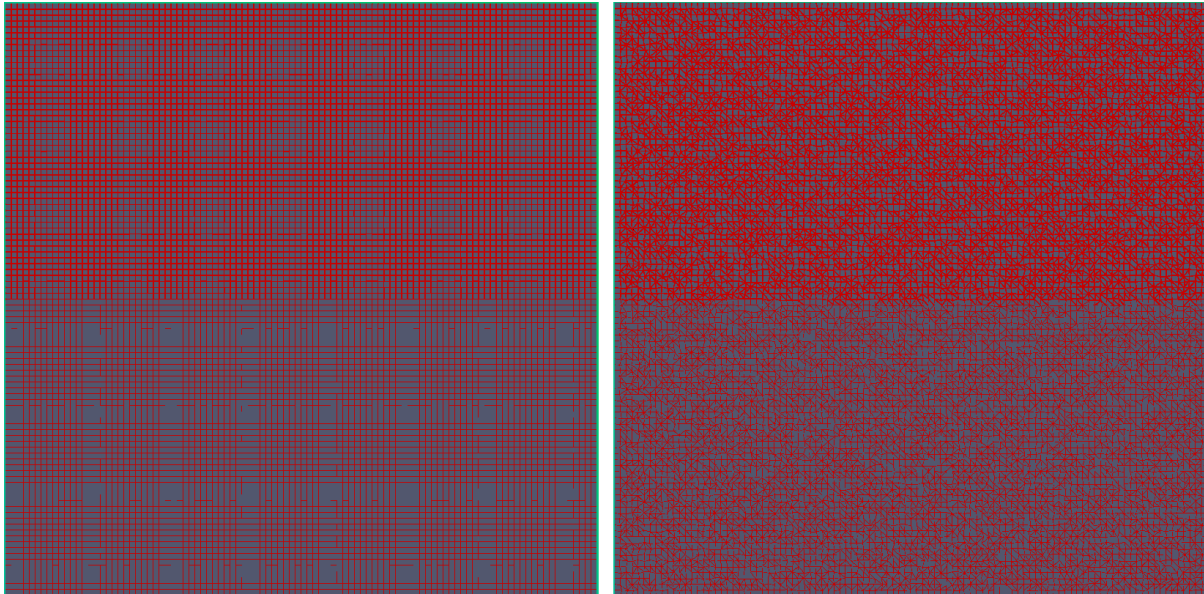


*Figure 70. Dual-porosity pore network (left: regular; right: irregular)*

In this group, all together three cases are tested. The **first** case uses uniform diameter: the throat diameters in the small pores region is set uniformly to  $5\mu m$ ; and the throat diameters in the larger pores region is set uniformly to  $10\mu m$ . The **second** case uses random diameters, which are in the range  $5\mu m \pm 5\%$  and  $10\mu m \pm 5\%$ , respectively, for the lower smaller-pores region and the upper larger-pores region. The **third** case uses random diameters as the second case. In



addition, the third case also varies the throat lengths as well as the number of throats connected to various pores (which is also called the *coordination number* for any given node or pore) (Figure 70). Note that, unlike previously, all these three cases in the present study open all their four sides to the outside flow.

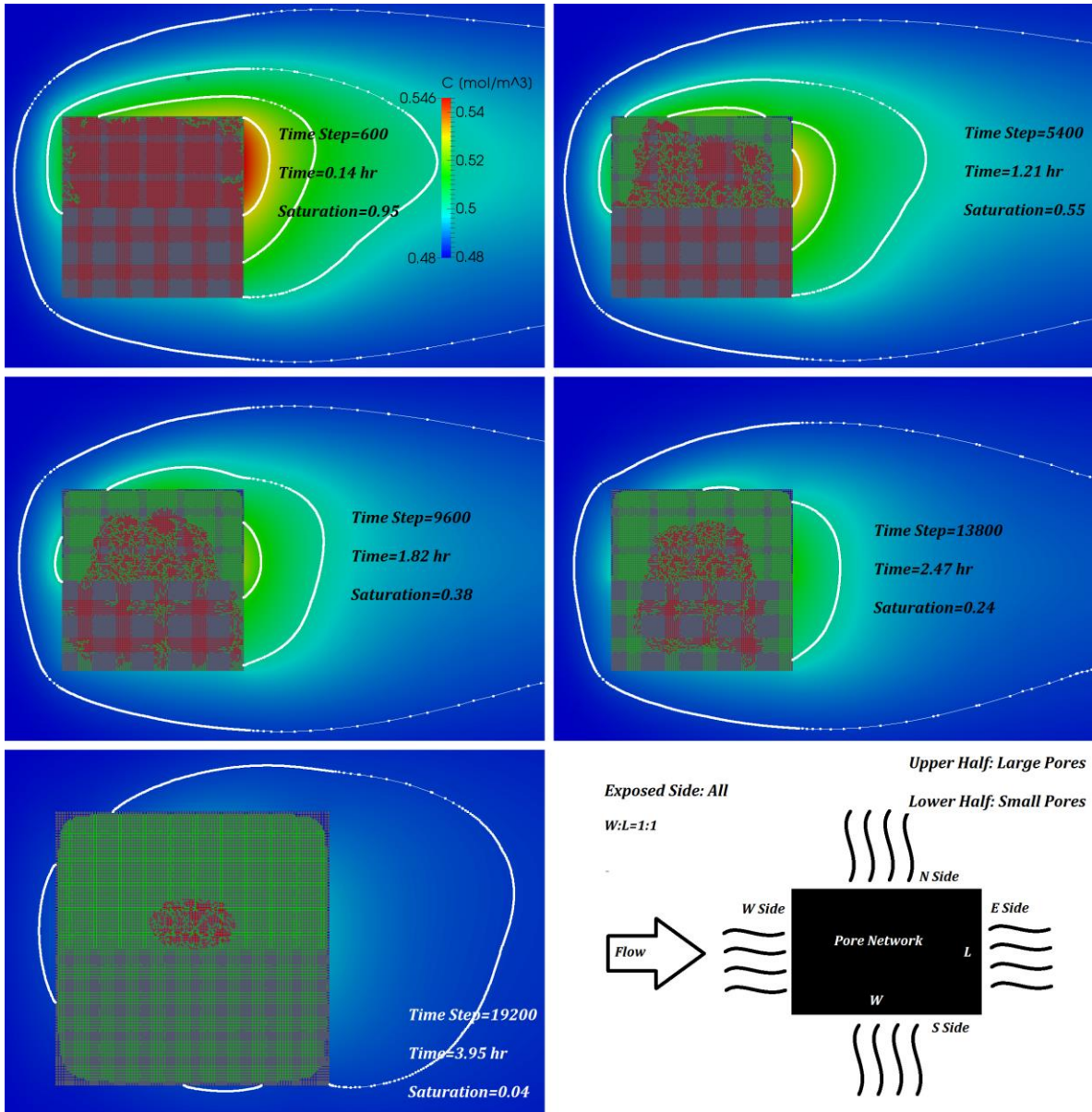


**Figure 71. Distributions of liquid-phase clusters and concentration contours – regular network, random throat diameters**

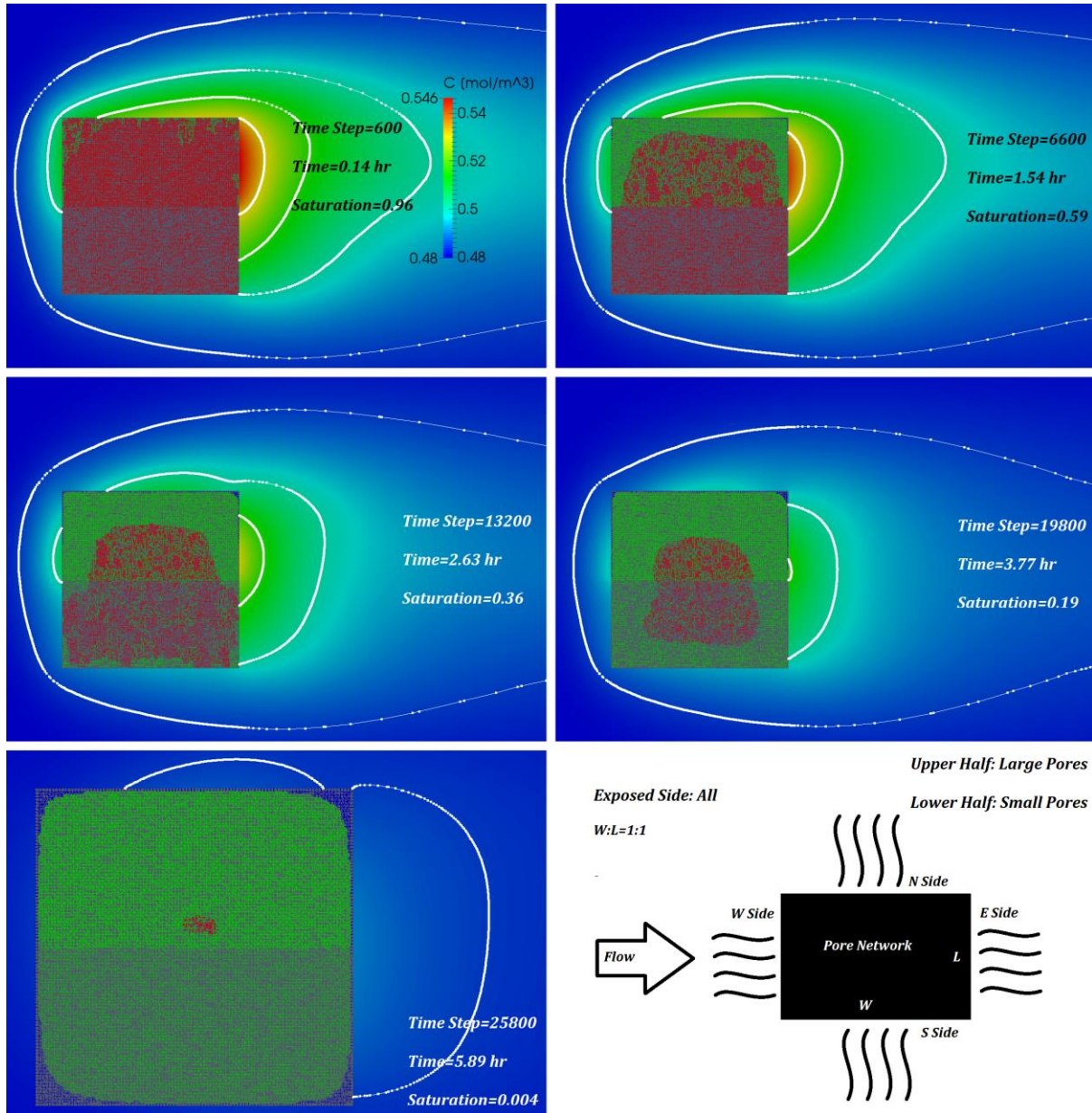


**Figure 72. Distributions of liquid-phase clusters and concentration contours – irregular network, random throat diameters**

Figure 71 shows the liquid-phase distribution inside the network and the surrounding concentration contours for the second case. Figure 72 shows the liquid-phase distribution and the surrounding concentration contours for the third case. On comparing these two cases, we can see

that the irregularity did not bring too many differences in the drying patterns observed within the network as well as in the CBL formation outside it.

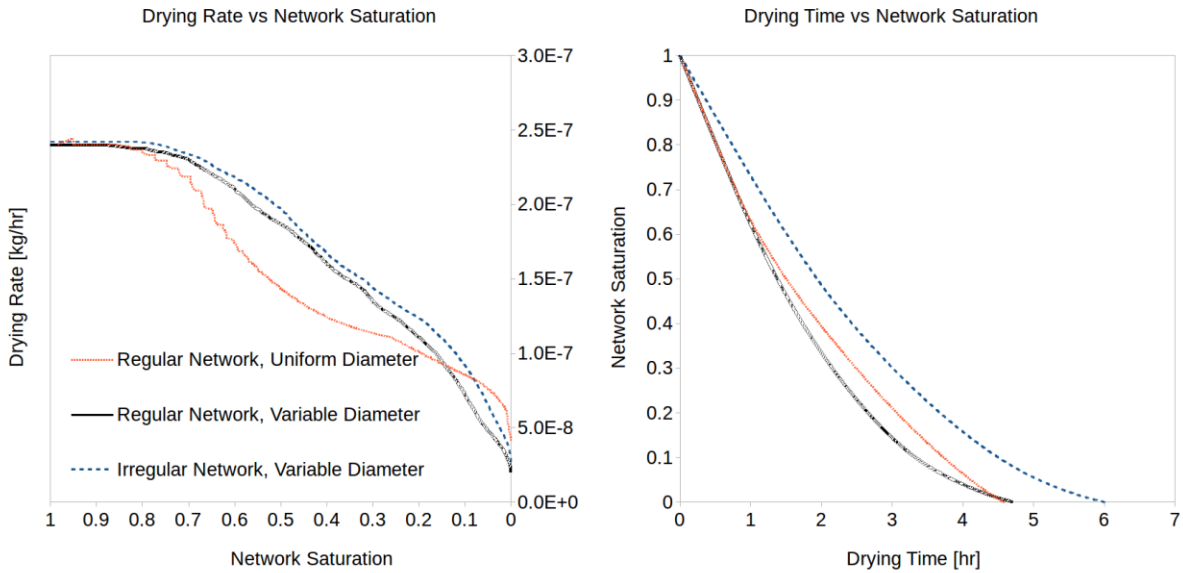


**Figure 73. Study of changes in drying rate and drying time of a dual-porosity network due to the introduction of geometrical irregularity**

Figure 73 studies the differences in drying rates and drying times between the three cases. This comparison shows that the introduction of irregularity is not influencing the drying behavior significantly. This corroborates the findings of Figure 71 and Figure 72 where not much difference in the drying patterns of two of these cases is observed. However, the irregularity does bring a big difference to the liquid mass contained within the network, hence the drying time for the irregular network is correspondingly longer.

### 9.3 Summary & Conclusions

This chapter applied the model developed in chapter 5 to study the drying in a dual-scale

porous media. At first, the drying simulation of a square-shaped and dual-porosity pore network is compared with a previously published experimental study. Two cases of small-pores side open and large-pore side open are considered. It is observed that though the simulation results of the  $12 \times 12$  network fail to match the experimental drying curves completely, important landmarks in the drying process (such matching of overall drying times and complete emptying of large pores before the onset of drying in the small pore region of the large-pores side open case) are achieved. Next the drying of the same square-shaped, dual-porosity domain using a much refined  $100 \times 100$  network is carried out in a uniform air flow after keeping either the large-pores or the small-pores side open. The former leads to faster drying and complete emptying of the large pores before the small pores. Using the same refined network, the case of all side open is studied using the same dual-porosity and square domain. Changing the throat cross-section from circle to square leads to much faster drying. Introduction of microstructural irregularity in the network by randomly changing throat diameter and changing the coordination number of pores does not affect the drying rate and drying time significantly.

## 10 SUMMARY AND CONCERNS

This thesis developed a fully-coupled implicit method to study the drying of porous media in laminar flows.

Firstly, a model without film effect is developed and then the film effect is added to it. A novel logistic equation is used to relate the pore network variable,  $\phi$ , with the external field variable,  $C$ .

A broad range of studies are carried out, including the studies on numerical algorithm, microstructure of pore network, and the environmental factors. The model is also applied to drying of thin and dual-scale porous media. Some interesting insights are discovered.

The model developed in this thesis can also be used to study more factors influencing the drying process, for example, the liquid properties, the contact angle, the round corner radius of the throats, etc. These studies are not performed limited to the size of this thesis, but they are all interesting immediate future working directions.

When it comes to new models, we find that the most interesting future work directions needs to be in 3D drying simulation and development of a new film effect model. Note that 3D simulation is preferred when one wants to study the influence of the external flow.

A new film effect model, which abandons the assumption of constant film radius across all liquid-film interfaces, needs to be developed. The current film effect model is broadly used by previous researches, but it is not good when it is applied to the dual-scale porous media.

## APPENDIX: MATHEMATICAL MODELS

The mathematical model as described in the main body is presented here in dimensionless form.

For the external flow field:

$$\begin{cases} \overline{\rho}_g(\overline{u} \frac{\partial \overline{u}}{\partial \overline{x}} + \overline{v} \frac{\partial \overline{u}}{\partial \overline{y}}) = -\frac{\partial \overline{p}}{\partial \overline{x}} + \frac{\overline{\mu}_g}{Re} \left( \frac{\partial^2 \overline{u}}{\partial \overline{x}^2} + \frac{\partial^2 \overline{u}}{\partial \overline{y}^2} \right) \\ \overline{\rho}_g(\overline{u} \frac{\partial \overline{v}}{\partial \overline{x}} + \overline{v} \frac{\partial \overline{v}}{\partial \overline{y}}) = -\frac{\partial \overline{p}}{\partial \overline{y}} + \frac{\overline{\mu}_g}{Re} \left( \frac{\partial^2 \overline{v}}{\partial \overline{x}^2} + \frac{\partial^2 \overline{v}}{\partial \overline{y}^2} \right) \\ \frac{\partial \overline{u}}{\partial \overline{x}} + \frac{\partial \overline{v}}{\partial \overline{y}} = 0 \end{cases}$$

The external flow field is solved using the implicit method.

For the evaporation without film effect:

$$\begin{cases} \overline{u} \frac{\partial \overline{C}_i}{\partial \overline{x}} + \overline{v} \frac{\partial \overline{C}_i}{\partial \overline{y}} = \frac{1}{Pe} \left( \frac{\partial^2 \overline{C}_i}{\partial \overline{x}^2} + \frac{\partial^2 \overline{C}_i}{\partial \overline{y}^2} \right) + \frac{1}{Pe} \sum_j \frac{\overline{A}_{ij}}{\overline{\delta}_{ij}} (\overline{C}_j - \overline{C}_i), \text{ for external field} \\ \sum_j \frac{\overline{A}_{ij}}{\overline{\delta}_{ij}} (\overline{C}_j - \overline{C}_i) = 0, \text{ for gas pores of the pore network} \end{cases}$$

For the evaporation with film effect:

$$\begin{cases} \overline{u} \frac{\partial \overline{C}_i}{\partial \overline{x}} + \overline{v} \frac{\partial \overline{C}_i}{\partial \overline{y}} = \frac{1}{Pe} \left( \frac{\partial^2 \overline{C}_i}{\partial \overline{x}^2} + \frac{\partial^2 \overline{C}_i}{\partial \overline{y}^2} \right) + \frac{1}{Pe} \sum_j \frac{\overline{A}_{ij}}{\overline{\delta}_{ij}} (\overline{C}_j - \overline{C}_i), \text{ for external field} \\ \sum_j \frac{(\overline{\phi}_j - \overline{\phi}_i)}{\overline{\delta}_{ij}} = 0, \text{ for gas pores of the pore network} \end{cases}$$

In which,  $\overline{C}_i$  is related with  $\overline{\phi}_i$  at the porous media openings:

$$\bar{C}_i = \frac{2}{\bar{\phi}_i(1 + e^{-\frac{c\bar{\phi}_i}{\varphi_2}})} \bar{\phi}_i - 1$$

The evaporation is solved using an implicit time marching method.

The dimensionless variables are defined as:

$$\bar{u} = \frac{u}{U^*}, \bar{v} = \frac{v}{U^*}, \bar{x} = \frac{x}{\delta^*}, \bar{y} = \frac{y}{\delta^*}, \bar{\rho}_g = \frac{\rho_g}{\rho^*}, \bar{\mu}_g = \frac{\mu_g}{\mu^*}, Re = \frac{\rho^* U^* \delta^*}{\mu^*}, \bar{C} = \frac{C}{C^*}, \bar{A} = \frac{A}{A^*}, \bar{\phi} = \frac{\phi}{\phi^*},$$

$$Pe = \frac{U^* \delta^*}{D^*}$$

The other reference values are defined using basic reference value:

$$U^* = \frac{\delta^*}{t^*}, p^* = \rho^* U^{*2}, A^* = \delta^{*2}, t^* = \frac{\rho^* \delta^{*2}}{D^* M^* C^*}, \phi^* = M^* D^* A^* C^*$$

The basic reference values are chosen to be:

$\delta^*$ : the average throat diameter of the pore network;  $\rho^*$ : the liquid density;  $\mu^*$ : the liquid viscosity;  $M^*$ : the liquid molar density;  $D^*$ : the liquid mass diffusivity;  $C^*$ : the saturated vapor concentration.

## REFERENCES

- Balhoff, M. T., Thompson, K. E. & Hjortsø, . M., 2007. Coupling pore-scale networks to continuum-scale models of porous media. *Computers & Geosciences*, 33(3), pp. 393-410.
- Bear, J., 1988. *Dynamics of Fluids in Porous Media*. s.l.:Dover Publications.
- Beyhaghi, S. & Pillai, K. M., n.d. Achieving the inside-outside Coupling during Simulation of Isothermal Drying of a Porous Medium in a Turbulent Flow.
- Beyhaghi, S., Xu, Z. & Pillai, K. M., Under Review. Achieving the inside-outside Coupling during Simulation of Isothermal Drying of a Porous Medium in a Turbulent Flow. *Transport in Porous Media*.
- Dullien, F. . A., 1991. *Porous Media: Fluid Transport and Pore Structure*. s.l.:Academic Press.
- Huinink, H. P., Pel, L., Michels, M. & Prat, M., 2002. Drying Processes in the Presence of Temperature Gradients-Pore-Scale Modeling. *European Physical Journal E*, Volume 9, pp. 487-498.
- Jayas, D. S., Cenkowski, S., Pabis, S. & Muir, W. E., 1991. Review of Thin-Layer Drying and Wetting Equations. *Drying Technology*, 9(3), pp. 551-588.
- Laurindo, J. B. & Prat, M., 1996. Numerical and Experimental Network Study of Evaporation in Capillary Porous Media-Phase Distributions. *Chemical Engineering Science*, 51(23), pp. 5171-5185.



- Laurindo, J. B. & Prat, M., 1998. Numerical and Experimental Network Study of Evaporation in Capillary Porous Media-Drying Rates. *Chemical Engineering Science*, 53(12), pp. 2257-2269.
- Lee, T. & Mateescu, D., 1998. Experimental and Numerical Investigation of 2-D Backward-Facing Step Flow. *Journal of Fluids and Structures*, Volume 12, pp. 703-716.
- Mao, X., Wang, S. & Shimai, S., 2008. Porous ceramics with tri-modal pores prepared by foaming and starch consolidation. *Ceramics International*, 34(1), pp. 107-112.
- Metzger, T., Irawan, A. & Tsotsas, E., 2007. Isothermal Drying of Pore Networks: Influence of Friction for Different Pore Structures. *Drying Technology*, Volume 25, pp. 49-57.
- Metzger, T. & Tsostas, E., 2008. Viscous Stabilization of Drying Front: Three-Dimensional Pore Network Simulations. *Chemical Engineering Research and Design*, Volume 86, pp. 739-744.
- Muralidhar, K., Verghese, M. & Pillai, K. M., 1993. Application of an Operator-Splitting Algorithm for Advection-Diffusion Problems. *Numerical Heat Transfer Part A*, Volume 23, pp. 99-113.
- Nowicki, S. C. & Davis, H. T., 1992. Microscopic Determination of Transport Parameters in Drying Porous Media. *Drying Technology*, 10(4), pp. 925-946.
- Patankar, S. V., 1980. *Numerical Heat Transfer and Fluid Flow*. s.l.:Taylor & Francis.
- Pillai, K. M., Prat, M. & Marcoux, M., 2009. A Study on Slow Evaporation of Liquids in a Dual-Porosity Porous Medium using Square Network Model. *International Journal of Heat and*

*Mass Transfer*, Volume 52, pp. 1643-1656.

Prabhanjan, D. G., Ramswamy, H. S. & Raghavan, G. S. V., 1995. Microwave-Assisted Convective Air Drying of Thin Layer Carrots. *Journal of Food Engineering*, Volume 25, pp. 283-293.

Prat, M., 1993. Percolation Model of Drying under Isothermal Conditions in Porous Media. *International Journal of Multiphase Flow*, 19(4), pp. 691-704.

Prat, M., 2007. On the Influence of Pore Shape, Contact Angle and Film Flows on Drying of Capillary Porous Media. *International Journal of Heat and Mass Transfer*, Volume 50, pp. 1455-1468.

Quintard, M. & Whitaker, S., 1993. Transport in ordered and disordered porous media: volume-averaged equations, closure problems, and comparison with experiment. *Chemical Engineering Science*, 48(14), pp. 2537-2564.

Sander, A., 2007. Thin-layer drying of porous materials: Selection of the appropriate mathematical model and relationships between thin-layer models parameters. *Chemical Engineering and Processing*, Volume 46, pp. 1324-1331.

Shaeri, M. R., 2012. *Investigating Regular Pore-Network Models to Predict Drying in Porous Media*, Milwaukee: s.n.

Shaeri, M. R., Beyhaghi, S. & Pillai, K. M., 2012. Drying of a Porous Medium, with Multiple Open

Sides using a Pore-Network Model Simulation. *International Communications in Heat and Mass Transfer*, 39(9), pp. 1320-1324.

Shaeri, M. R., Beyhaghi, S. & Pillai, K. M., 2013. On Applying an External-Flow Driven Mass Transfer Boundary Condition to Simulate Drying from a Pore-Network Model. *International Journal of Heat and Mass Transfer*, Volume 57, pp. 331-344.

Suzuki, K., Ikari, K. & Imai, H., 2003. Synthesis of mesoporous silica foams with hierarchical trimodal pore structures. *Journal of Materials Chemistry*, Volume 13, pp. 1812-1816.

Tsilingiris, P., 2008. Thermophysical and transport properties of humid air at temperature range between 0 and 100 C. *Energy Conversion and Management*, Volume 49, pp. 1098-1110.

Vafai, K., 2015. *Handbook of Porous Media*. 3rd ed. s.l.:CRC Press.

Versteeg, H. K. & Malalasekera, W., 2007. *An Introduction to Computational Fluid Dynamics - The Finite Volume Method*. 2 ed. s.l.:Pearson.

Wikipedia, 2016. *Poroue Medium*. [Online]

Available at: [https://en.wikipedia.org/wiki/Porous\\_medium](https://en.wikipedia.org/wiki/Porous_medium)

[Accessed Feb 2016].

Xu, Z. & Pillai, K. M., Under Review. Analyzing Slow Drying in a Porous Medium placed adjacent to Laminar Air Flow using a Pore-Network Model. *Numerical Heat Transfer, Part A*.

Yiotis, A. G. B. A. G., Stubos, A. K., Tsimpanogiannis, I. N. & Yortsos, Y. C., 2004. Effect of

liquid films on the drying of porous media. *AIChE Journal*, Volume 50, pp. 2721-2737.

Yiotis, A. G. & Boudouvis, A. G., 2003. Effect of Liquid Films on the Isothermal Drying of Porous Media. *Physical Review E*, Volume 68, p. 037303.

Yiotis, A. G. & Stubos, A. K., 2001. A 2-D Pore-Network Model of the Drying of Single-Component Liquids in Porous Media. *Advances in Water Resources*, Volume 24, pp. 439-460.

Yiotis, A. G. & Tsimpanogiannis, I. N., 2007. Coupling between external and internal mass transfer drying of a porous medium. *Water Resource Research*, 43(6), p. W06403.

Zenyuk, I. V., Medicib, E., Allen, J. & Web, A. Z., 2015. Coupling continuum and pore-network models for polymer-electrolyte fuel cells. *International Journal of Hydrogen Energy*, 40(46), p. 16831–16845.

Zhou, D., Blunt, M. & Orr, F. M. J., 1997. Hydrocarbon Drainage along Corners of Noncircular Capillaries. *Journal of Colloid and Interface Science*, Volume 187, pp. 11-21.

# CURRICULUM VITAE

*Zhenyu Xu*

## **Educations**

- **Ph.D.** in Mechanical Engineering, *University of Wisconsin – Milwaukee*, 2016
- **Master** in Fluid Mechanics, *Beijing University of Aeronautics and Astronautics*, 2004
- **Bachelor** in Aerospace, *Beijing University of Aeronautics and Astronautics*, 2001

## **Working Experience**

- *Harley-Davidson*, Product Development Center, Milwaukee, 2006-2012 (Part-Time)
- *UWM*, Research Assistant, 2005-2006
- *CD-adapco Japan* (CDAJ), Beijing/Shanghai Office, 2004-2005

## **Teaching Experience**

- Introduction to Fluid Mechanics, Lecturer and Lab Instructor, 2013
- Intermediate Fluid Mechanics, CFD Lab Instructor, 2014
- Engineering Fundamentals, Lab Instructor, 2012-2015

## **Developed Software**

- *PORODRY™*

## **Selected Publications**

- Numerical Simulation of Supersonic MHD Channel Flows, Zhenyu Xu, Chunhian Lee, Journal of Beijing University of Aeronautics and Astronautics, 2005, 31(8)
- A Numerical Study of a Cooling Ratio for Laser Based Prototyping Technology with a Sample of 316l Stainless Steel, R.S. Amano, Z. Xu, J. Martinez Lucci and Pradeep Rohatgi, The Open Automation and Control Systems Journal, 2012, 4, 1-7
- Analyzing Slow Drying in a Porous Medium placed adjacent to Laminar Air Flow using a Pore-Network Model, Zhenyu Xu, Krishna M Pillai, Numerical Heat Transfer, Part A: Applications (Accepted)
- Modeling Drying in Thin Porous Media after Coupling Pore-Level Drying Dynamics with External Flow Field, Zhenyu Xu, Krishna M Pillai, Drying Technology (Under Review)
- Modeling Drying in Dual-Scale Porous Media after Coupling Pore-Level Drying Dynamics with External Flow Field, Zhenyu Xu, Krishna M Pillai, International Journal of Heat and Mass Transfer (Under Review)